MYOGENIC EFFECTORS AND DISEASE

SUPERVISORY COMMITTEE

Hesham A. Sadek, M.D., Ph.D.

Joshua T. Mendell, M.D., Ph.D.

George N. DeMartino, Ph.D.

Eric N. Olson, Ph.D.

To my family, especially my dearest niece Iria.

I would need another dissertation just to explain how grateful I am to them.

Acknowledgements

I would like to acknowledge all the people who have contributed to the scientific work presented here and to my growth as a scientist during my thesis.

- My mentors in the Olson Lab: Dr. Liu, Dr. Bassel-Duby and Dr. Olson for their precious advice, support, and patience all these years.

- My thesis committee: Dr. Sadek, Dr. Mendell and Dr. DeMartino for their feedback, understanding, and constructive criticism.

- Our collaborators in Dr. Rizo-Rey lab (Klaudia Jaczynska, Dr. Sun) and Dr. Jaarsveld at UMC Utrecht for their shared enthusiasm and insights.

- The Department of Molecular Biology and my Graduate Program (Genetics, Development, and Disease) for being such fostering communities.

- Current and former members of the Olson Lab, particularly those I have worked the closest with: Bercin Cenik, Xurde Menendez, Jessica Cannavino, Maria Abad, Pengpeng Bi, John McAnally, Cristina Rodriguez-Caycedo, Hui Li, Priscilla Jaichander, Efrain Sanchez-Ortiz, Wenduo, Susan, and too many others to list here.

- Our trainees, Mateusz and Gabriela, for challenging the things I thought I knew.

- My colleague and inspiring scientist Yichi (Tony) Zhang, for his essential contribution to the work included in this thesis.

Thank you.

Dallas, 2021

MYOGENIC EFFECTORS AND DISEASE

by

Andres Ramirez Martinez

DISSERTATION

Presented to the Faculty of the Graduate School of Biomedical Sciences

The University of Texas Southwestern Medical Center at Dallas

In Fulfillment of the Requirements

For the Degree of

DOCTOR OF PHILOSOPHY

The University of Texas Southwestern Medical Center at Dallas

Dallas, Texas

December 2021

MYOGENIC EFFECTORS AND DISEASE

Andres Ramirez-Martinez

The University of Texas Southwestern Medical Center at Dallas, 2021

Supervising Professor: Eric N. Olson, Ph.D.

Abstract

Skeletal muscle is essential for life. Inside muscle fibers, filaments of actin and myosin slide on each other to generate the mechanical forces that drive muscle contraction, movement, and breathing. Mutations in muscle-related genes can cause severe diseases in humans. Here we characterize the role of three understudied muscle-specific genes and their potential contribution to human disease. We show that constitutive and juvenile loss of the nuclear envelope protein Net39 in mice recapitulates different manifestations of Emery-Dreifuss muscular dystrophy. Deletion of Net39 caused disruption of nuclear envelope integrity and associated genomic, transcriptional, and metabolic changes that compromised muscle function. Mechanistically, Net39 regulates nuclear organization by associating with LEM proteins, and gene expression by controlling the transcription factor Mef2c. In contrast, global deletion of the Kelch protein Klhl41 in mice causes severe nemaline myopathy, including neonatal lethality and aggregation of contractile proteins in muscle, particularly Nebulin. Molecularly, Klhl41 acts as a chaperone for Nebulin, and N-terminal poly-ubiquitination of Klhl41 acts as a signal to regulate its activity. Finally, we identify a novel pathogenic mutation in the cell fusogen Myomixer. We show that patients with Carey-Fineman-Ziter syndrome lose a region of Myomixer required to destabilize opposing cell membranes during myoblast fusion. Overall, our findings here highlight the contribution of understudied genes to muscle biology and the molecular etiology of muscle disorders.

Table of contents

Prior publications

1. **Ramirez-Martinez A***, Zhang Y*, Chen K, Jiwoong K, Cenik B, McAnally J, Cai C, Shelton J, Huang J, Brennan A, Evers B, Mammen P, Xu L, Bassel-Duby R, Liu N, Olson EN. (2021). The nuclear envelope protein Net39 is essential for muscle nuclear integrity and chromatin organization. *Nat Commun.* 12:690.
2. Landemaine A, **Ramirez-Martinez A**, Monestier O, Sabin N, Rescan PY, Olson EN, Gabillard JC. (2019) Trout myomaker contains 14 minisatellites and two sequence extensions but retains fusogenic function. *J Biol Chem.* 19;294(16):6364-6374
3. **Ramirez-Martinez A,** Cenik B, Bezprozvannaya S, Chen B, Bassel-Duby R, Liu N, and Olson EN. (2017) KLHL41 stabilizes skeletal muscle sarcomeres by nonproteolytic ubiquitination. *Elife* 6.
4. Bi P, **Ramirez-Martinez A**, Li H, Cannavino J, McAnally JR, Shelton JM, Sánchez-Ortiz E, Bassel-Duby R Olson EN. (2017) Control of muscle formation by the fusogenic micropeptide myomixer. *Science* 356:323–327.
5. Di Gioia SA **et al.** (2017) A defect in myoblast fusion underlies Carey-Fineman-Ziter syndrome. *Nat Commun.* 6;8:16077.
6. Golden RJ, Chen B, Li T, Braun J, Manjunath H, Chen X, Wu J, Schmid V, Chang TC, Kopp F, **Ramirez-Martinez A**, Tagliabracci VS, Chen ZJ,7, Xie Y, Mendell JT. (2017) An Argonaute phosphorylation cycle promotes microRNA-mediated silencing. *Nature* 542(7640):197-202.

Parts of this dissertation, including figures, have been reproduced, with or without modifications, from published work.

List of figures

List of abbreviations

AAV	Adeno-associated virus.
ATAC	Assay for Transposase-Accessible Chromatin.
BACK	BTB And C-terminal Kelch domain.
BioID	Proximity-dependent Biotin Identification.
BMP	Bone Morphogenetic Protein.
b-HLH	Basic helix-loop-helix.
BTB	Broad-Complex, Tramtrack, and Bric a brac domain.
CFZS	Carey-Fineman-Ziter syndrome.
ChIP	Chromatin immunoprecipitation.
DAVID	Database for Annotation, Visualization, and Integrated Discovery.
DamID	DNA adenine methyltransferase identification.
DMD	Duchenne muscular dystrophy.
EDL	Extensor digitorum longus muscle.
EDMD	Emery-Dreifuss muscular dystrophy.
FAPs	Fibro-adipogenic precursors.
FGF	Fibroblast growth factor.
GREAT	Genomic Regions Enrichment of Annotations Tool.
HSA	Human skeletal actin.
HSQC	Heteronuclear single quantum coherence.
iPSC	Induced pluripotent stem cell.
LAD	Lamin-associated domain.
LGMD	Limb-Girdle muscular dystrophy.
LEM	LAP2, emerin, MAN1 domain.
LINC	Linker of Nucleoskeleton and the Cytoskeleton.
NM	Nemaline myopathy.
QD	Quadriceps muscle.
ssODN	single-stranded oligo donor.
TAP	Tandem affinity purification.
WGA	Wheat germ agglutinin.

1. Skeletal muscle, myogenesis, and disease

Skeletal muscle is the most abundant tissue in human bodies, comprising 40-60% of our total weight[1]. As such, it constitutes a remarkable signaling and metabolic hub. Histologically, mature muscle is composed of bundles of long, multinucleated cells (myofibers) and associated cell types (**Fig. 1a**). The main function of skeletal muscle is to drive voluntary body movement upon neuronal impulse through the calcium-dependent sliding of actomyosin filaments[2]. Actomyosin filaments are part of the sarcomere, a complex protein network of structural, regulatory, and scaffolding proteins responsible for muscle contraction (**Fig. 1b**). For brevity, this chapter will focus on development of murine limb skeletal muscles and human neuromuscular diseases, as the scientific work throughout the dissertation is centered on these areas.

Developmentally, skeletal muscle is a tissue of mesodermal origin. Cell proliferation and migration during gastrulation give rise to the notochord, a rod-like structure of cells derived from the mesoderm. The notochord establishes anterior-posterior polarity and provides additional developmental signals. The notochord expresses the Bone Morphogenetic Protein (BMP) inhibitor Noggin, generating a gradient of BMP signaling to further specify the surrounding mesoderm into different subtypes[3]: paraxial mesoderm, intermediate mesoderm, and lateral plate mesoderm. The paraxial mesoderm undergoes a process of segmentation called somitogenesis[4]. Temporal and spatial oscillations of Notch, Wnt and Fibroblast growth factor (FGF) signaling (also known as the segmentation clock) regulate the activity of transcription factors (such as Hes7 and Mesp2) to form paired blocks of somites along the neural tube, while the outer cells undergo mesenchymal-to-epithelial transition around them. Then, the

somites become compartmentalized into the ventral mesenchymal sclerotome (giving rise to skeleton and tendons) and the dorsal epithelial dermomyotome (giving rise to skeletal muscle, brown fat and dermis of the back). However, cells within the somites are not yet committed to a specific fate at this stage.

In mice, primary myogenesis occurs between embryonic day (E) 8.5 and E11.5. At E8.5, a subset of cells in the dermomyotome delaminate, thus detaching and migrating[5]. The first muscle to form that way is the myotome, immediately next to the dermomyotome, which will be later incorporated into the trunk musculature. For limb muscle development, muscle progenitors must reach the limb region following specific signals. Delamination and migration are controlled by two homeodomain transcription factors: Pax3 and Lbx1 (**Fig. 1c**). Pax3 controls the expression of c-Met, the receptor for hepatocyte growth factor (HGF). HGF is secreted across the migratory path to the limbs by mesenchymal cells. Once myogenic precursors reach the limbs, they proliferate. Then, additional signals such as Wnt and Sonic hedgehog activate the expression of the myogenic regulatory factors MyoD and Myf5, while interaction with surrounding connective tissue contributes to the organization of specific muscles in the limb[6]. Pax3 directly activates Myf5 expression and it is downregulated during muscle differentiation. The function of MyoD and Myf5 is partially redundant in a muscle-dependent manner. MyoD and Myf5 act by forming heterodimers with E12 Basic helix-loop-helix (b-HLH) transcription factors to drive muscle specification and the expression of other transcriptional regulators such as Myogenin (Myog) and Mrf4[7]. The transcriptional activity of MyoD, Myog and Mrf4 results in the expression of downstream regulators as well as effectors of skeletal muscle differentiation. MyoD, Myog, Mrf4 and Myf5 belong the the b-HLH

family of transcription factors. While their expression is necessary for myogenesis, myogenesis also requires the presence of the Mef2 family of transcription factors[8]. MyoD induces Mef2c expression, and MyoD and Mef2c act synergistically to regulate their own transcription and downstream differentiation genes. Mef2 downstream targets include metabolic genes that regulate muscle fiber type, as well as components of the muscle contractile complex, the sarcomere. Finally, the myogenic differentiation program must be repressed in mature myofibers. Termination of differentiation is achieved through a Mef2-dependent negative-feedback loop[9]. For instance, HDAC9, a Mef2c target, can associate with DNA-bound Mef2c to regulate the surrounding chromatin environment and dampen Mef2c activity.

At E12.5, Pax3 is downregulated and replaced by the paralog Pax7. Pax7 expression is maintained in adult muscle precursors. Pax3 and Pax7 are transcriptional activators and their gene targets mostly overlap[10]. Additional myofibers are formed in a secondary wave of myogenesis at E14.5. Secondary myofibers are morphologically distinct and express fast myosin isoforms, in contrast to slow and embryonic myosin expression in primary myofibers. It is also during this time that neurons start innervating muscle to form neuromuscular junctions. This process continues after birth and regulates the slow and fast fiber type specification. However, part of the Pax7 positive cells do not differentiate. Instead, they become a population of resident muscle precursor cells in adult skeletal muscle. Pax7 positive cells localize under the basal lamina of muscle fibers (thus their name, satellite cells). Satellite cells maintain muscle fiber homeostasis and are responsible for the remarkable plasticity and regenerative capacity of skeletal muscle. Satellite cells remain quiescent until external

signaling, similarly to primary myogenesis, induces their proliferation and expansion[11]. Part of the satellite cell population will differentiate and form new myofibers or fuse into existing ones, whereas a fraction will return to quiescence and act as a muscle reservoir. More recently, a new myogenic precursor in adult skeletal muscle has been identified[12]. This cell population is distinct from satellite cells: their localization is interstitial instead of sublaminal, they are negative for Pax3 or Pax7, and they can be identified by expression of the transcription factor Twist2. Further developmental studies of this new population are required, as Twist2 positive cells are heterogeneous and only a subset possess myogenic potential.

Pathological changes in muscle can result in loss of muscle fiber integrity (muscular dystrophies) or abnormalities in muscle function that maintain muscle fibers intact (myopathies), albeit clinical classifications may overlap and often present a cardiac phenotype[13]. These phenotypes may cause impaired muscle contractility and fiber size (atrophy), leading to muscle weakness, reduced mobility and, in some cases, developmental abnormalities such as reduced growth, craniofacial alterations, or scoliosis. In the most severe cases, impairment of diaphragmatic function can require ventilation and be the cause of patient death. Mutations in the myogenic transcription factors can lead to muscle diseases. Genomic translocations of Pax3 and Pax7 cause rhabdomyosarcoma[14], and mutations in MyoD have been shown to cause congenital myopathy with diaphragmatic defects, and dysmorphic facies[15]. In contrast, Mef2c is also expressed in brain, and human mutations cause neurological alterations[16]. However, probably because myogenic regulatory factors play such extensive roles in muscle formation, most monogenic

neuromuscular disorders are caused by mutations in the many downstream targets of the myogenic program.

The transcriptional regulators of myogenesis have been extensively studied in vivo and in vitro. However, characterization of their downstream effectors is an active area of research, and the focus of this dissertation (**Fig. 1c**). Some of the genes activated by myogenic transcriptional factors still have an unclear function. One such case is the MyoD target gene Net39/Plpp7. Net39 encodes for a nuclear envelope protein. Net39 was previously reported to have both positive and inhibitory functions in myogenesis in vitro[17,18]. Elucidation of the role of Net39 in muscle nuclear organization and its contribution to Emery-Dreifuss muscular dystrophy will be the focus of Chapter 2. Chapter 3 will encompass regulation of sarcomere integrity by the Mef2c target Klhl41. Mutations in Klhl41 and its closest paralog, Klhl40 have been associated to nemaline myopathy[19-21], but the molecular mechanism is elusive. Chapter 4 will include ongoing research on the muscle fusogen Mymx, and the characterization of a novel mutation causing Carey-Fineman-Ziter syndrome. Overarching concluding remarks from the studies will be included in Chapter 5. Finally, the protocols used for this thesis will be detailed in Chapter 6.

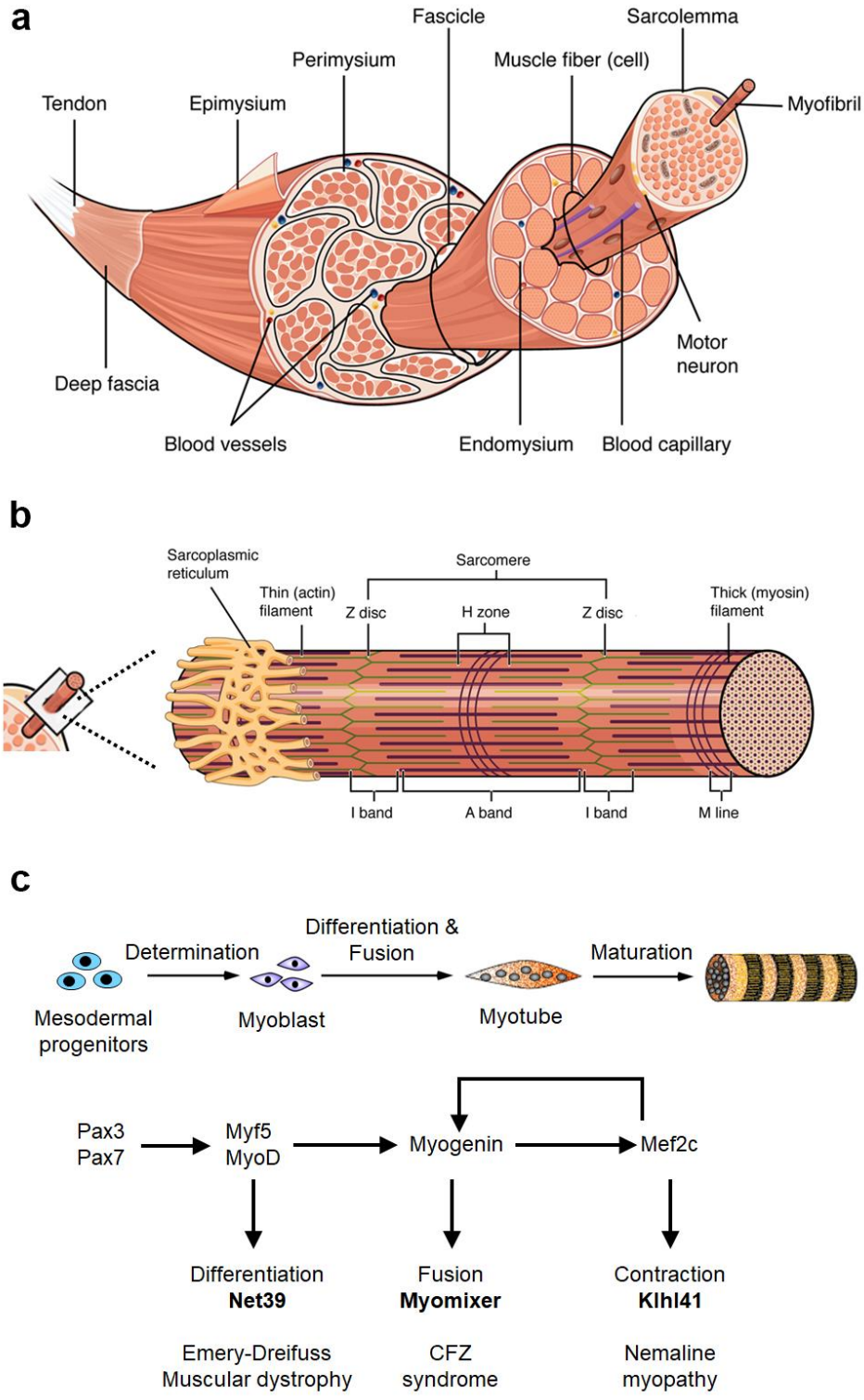

Fig. 1. Skeletal muscle and myogenesis. a. Anatomical organization of muscle. **b.** The sarcomere in skeletal muscle. Adapted from [22]. **c.** Stepwise control of myogenesis, transcription factors involved in the process, and selected downstream targets associated with human diseases.

2. Net39 controls myonuclear integrity and genome organization

2.1. The nuclear envelope and Emery-Dreifuss muscular dystrophy

The nuclear envelope is a double lipid bilayer that separates the cytosol from the nucleoplasm. Beneath the inner nuclear membrane is the nuclear lamina, which includes the intermediate filaments formed by Lamins A, B1, B2, and C, providing support to the nucleus. Lamins and transmembrane proteins within the nuclear envelope are involved in maintaining nuclear envelope structure, nuclear positioning, and chromatin organization[17,23-26]. The transport of molecules between the nucleus and cytosol is mediated by the nuclear pore complex[27], whereas mechanical communication between both compartments occurs through the Linker of Nucleoskeleton and the Cytoskeleton (LINC) complexes[25,26], comprised of Sad1/UNC84 (Sun) 1 and 2 proteins at the inner nuclear membrane and the nuclear envelope spectrin-repeat proteins (Syne/Nesprins) at the outer nuclear membrane. The LINC complexes act as nuclear bridges to connect the cytoskeleton with the lamin nucleoskeleton and allow mechanical crosstalk between both compartments[25,28,29]. Lamins and nuclear envelope proteins have also been shown to play important roles in genome organization and regulation of gene expression. In eukaryotes, transcriptionally active euchromatin is typically found in the nuclear interior, whereas transcriptionally silent heterochromatin adjoins the nuclear envelope[30-32] and associates with nuclear lamins. Lamin-associated regions of DNA, termed lamin-associated domains (LADs), are dynamic and can redistribute upon gene activation[33,34].

Mutations in nuclear envelope proteins and lamins cause numerous

human diseases termed envelopathies, such as Emery-Dreifuss muscular dystrophy (EDMD). EDMD is characterized by skeletal muscle weakness, early contractures, and cardiomyopathy[28,35]. The two most frequent genetic causes of EDMD are X-linked recessive loss of Emerin (encoded by *EMD)* and autosomal dominant mutations in A-type lamins (encoded by *LMNA*)[36,37]. Additional genes involved in the pathogenesis of EDMD[28,36], including *FHL1*, *TMEM43*, Nesprins and *SUN2*[38-41], have also been identified.

Proteomic analysis of isolated nuclear envelopes[42] has identified nuclear envelope transmembrane proteins (NETs) with potential links to human disease[43]. Among them, transmembrane protein 39 (Net39), also referred to as inactive phospholipid phosphatase 7 (Plpp7 or Ppapdc3) (**Fig. 2a, b**), has been studied in vitro with conflicting results[17,18,44]. Net39 was initially reported to inhibit mTOR activity and IGF2 signaling, and knockdown of Net39 in C2C12 cells was shown to strongly promote myoblast differentiation[18]. In contrast, later studies[17,44] demonstrated that knockdown of Net39 blocked myogenesis and the main function of Net39 was to reposition specific genes that inhibit myoblast differentiation to the nuclear periphery, thus repressing their expression.

We observed that, in vitro, Net39 is upregulated during differentiation of immortalized C2C12 myoblasts, as well as differentiation of sublaminal satellite cells marked by the transcription factor Pax7 and interstitial myogenic muscle progenitor cells marked by the transcription factor Twist2 (also called $Tw2^{+}$ cells)[12] (**Fig. 2c**). The expression of Net39 is regulated by the myogenic transcription factors MyoD and Myogenin (**Fig. 2d**). In mice, Net39 transcript is enriched in skeletal muscle compared to other tissues. Within skeletal muscle, Net39 expression is higher in fast-twitch muscles (such as tibialis anterior) than

in slow-twitch muscle (soleus) (**Fig. 2e**). Net39 is also expressed in sites of embryonic myogenesis (**Fig. 2f**) and is upregulated during postnatal muscle growth (**Fig. 2g**).

Here we explored the role of Net39 as a muscle-specific regulator of nuclear envelope structure in vivo by studying two mouse models where Net39 is deleted. Global, constitutive knock-out (KO) of Net39 in mice causes profound changes in nuclear envelope integrity, chromatin organization, gene expression and metabolism, culminating in severe defects in muscle growth and function that lead to juvenile lethality. In contrast, conditional knock-out of Net39 in adult skeletal muscle (cKO) results in progressive myopathy. Mechanistically, Net39 regulates nuclear organization by its association with LEM proteins, and muscle gene expression by controlling the transcription factors Mef2c and MyoR. Overall, our work highlights the role of Net39 in muscle development and maintenance and explores its potential contribution to EDMD.

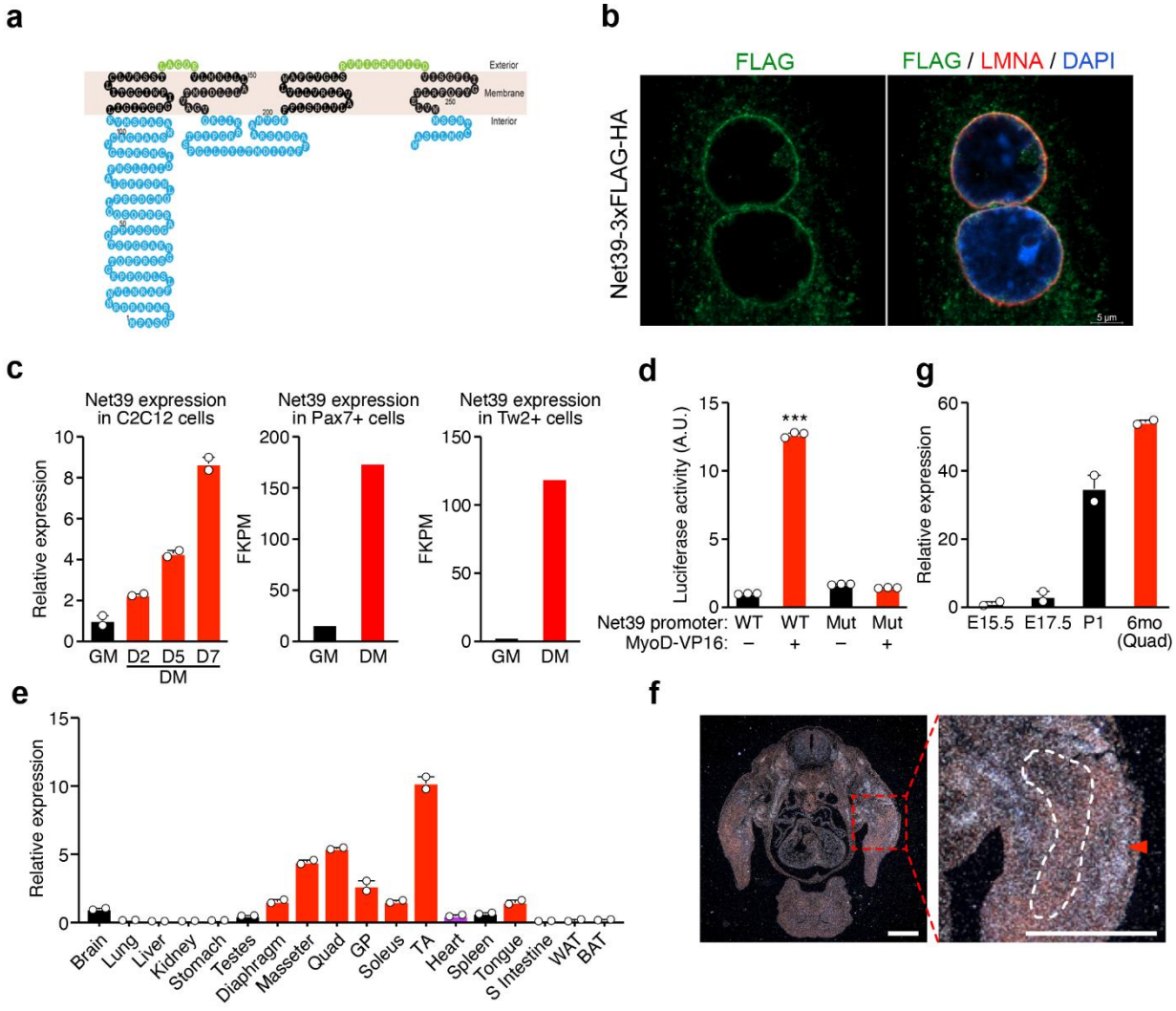

Fig. 2. Net39 is a nuclear envelope protein enriched in skeletal muscle.

a. Predicted topology of murine Net39 in the nuclear envelope. **b.** Immunofluorescence of C2C12 myotubes overexpressing tagged Net39. LMNA was used as a marker for the nuclear envelope. **c.** qRT-PCR analysis of Net39 expression during C2C12 differentiation GM and different days in DM. Levels are relative to expression in GM. n=2 technical replicates (left). Net39 expression in satellite cell-derived Pax7^{+} primary myoblasts before and after 48h of differentiation, as determined by RNA-seq (center). Net39 expression in interstitial myogenic precursor cells (Tw2^{+}) before and after 48h of differentiation, as determined by RNA-seq (right). FPKM: Fragments per kilobase million. **d.** Luciferase assays with Net39 promoter. A 442bp fragment upstream of Net39 ORF was cloned into a luciferase reporter (WT) or with the E-boxes within mutated (Mut). Luciferase activity was measured in the presence or absence of

MyoD-VP16. *p<0.01. Statistical comparisons between groups were evaluated by unpaired Student's t-test. **e.** qRT-PCR analysis of Net39 transcript in adult mouse tissues. Expression is normalized to its expression in brain. Red bars indicate skeletal muscle tissues. Purple bar represents heart tissue. Black bars indicate non-muscle tissues. TA: Tibialis Anterior. WAT: White Adipose Tissue. BAT: Brown Adipose Tissue. n=2 technical replicates. **f.** In-situ hybridization of Net39 transcript in a transverse section of a mouse at embryonic day 12.5. The area indicated within the white dashed line corresponds to cartilage. Arrowhead denotes positive signal in muscle. Scale bar: 500μm. **g.** qRT-PCR analysis of Net39 transcript in skeletal muscle during development (black bars) and in adult quadriceps (red bar)**.** Levels are relative to expression at E15.5. n=2 technical replicates.

2.2. Net39 is an essential component of the myonuclear envelope

Loss of Net39 in mice causes juvenile lethality and muscle abnormalities

To explore the functions of Net39 in vivo, we generated Net39 knockout (KO) mice using CRISPR/Cas9-mediated genome editing. The murine *Net39* gene spans two exons. We deleted the first exon of the gene using 2 sgRNAs (**Fig. 3a, b**), eliminating most of the open reading frame. Loss of Net39 mRNA and protein in KO mice was confirmed by RNA sequencing and western blot analysis, respectively, in quadriceps at 17 days postpartum (P17) (**Fig. 3c, d**).

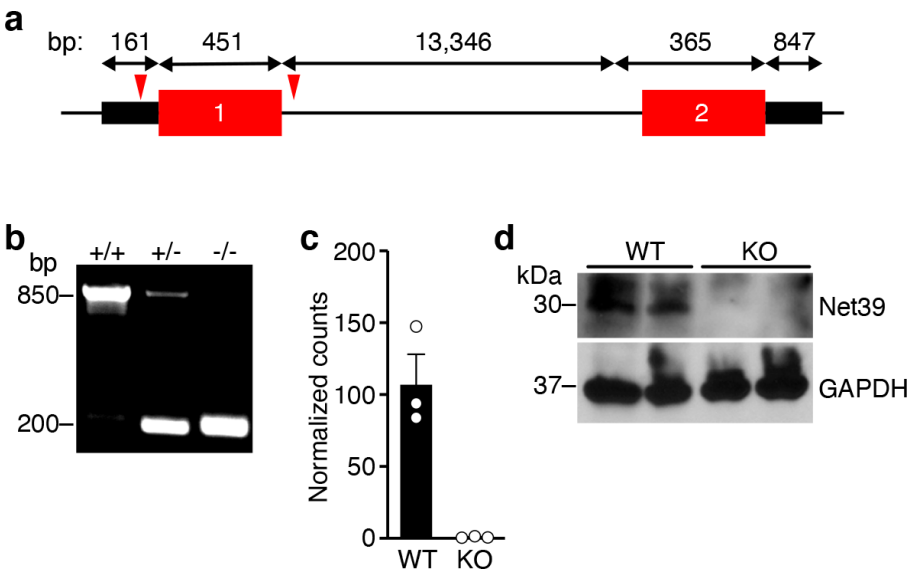

Fig. 3. Knockout strategy for Net39.

a. Gene structure of *Net39/Plpp7* and knock-out strategy. Red arrowheads indicate the locations of the sgRNAs used. Boxes represent exons. Black box denotes untranslated region and red box indicates open reading frame. **b.** Genotyping of Net39 KO mice by PCR. KO mice have a deletion of 559 base pairs (bp). **c.** RNA-seq analysis showing loss of Net39 RNA in postnatal day 17 (P17) quadriceps of Net39 KO mice. **d.** Western blot analysis showing loss of Net39 protein in P17 quadriceps of Net39 KO mice. GAPDH is a loading control.

Net39 heterozygous mice showed no discernible abnormalities. Net39 KO mice were born at Mendelian ratios from heterozygous intercrosses and were indistinguishable from WT littermates at birth. However, KO mice failed to thrive and were readily identifiable by P7 by their runted appearance, which became increasingly apparent with age (**Fig. 4a, b**). Net39 KO mice showed progressive lethality starting from P13, with none surviving past 23 days of age (**Fig. 4c**). KO mice displayed a waddling gait at P17, which was associated with an increasing number of falls, indicative of muscle dysfunction. Histological analysis and wheat germ agglutinin (WGA) staining of skeletal muscles revealed a reduction in myofiber cross-sectional area in KO compared to WT mice at P17 (**Fig. 4d, e**). Isolated EDL and soleus muscles from KO mice displayed lower tetanic force (**Fig. 4f**). Electron microscopy showed sarcomeric disarray in KO diaphragm (**Fig. 4g**). Aside from defects in skeletal muscle, we observed that cardiomyocytes in Net39 KO hearts were smaller than WT cardiomyocytes, but this did not lead to a reduction in heart function as measured by echocardiography (data not shown).

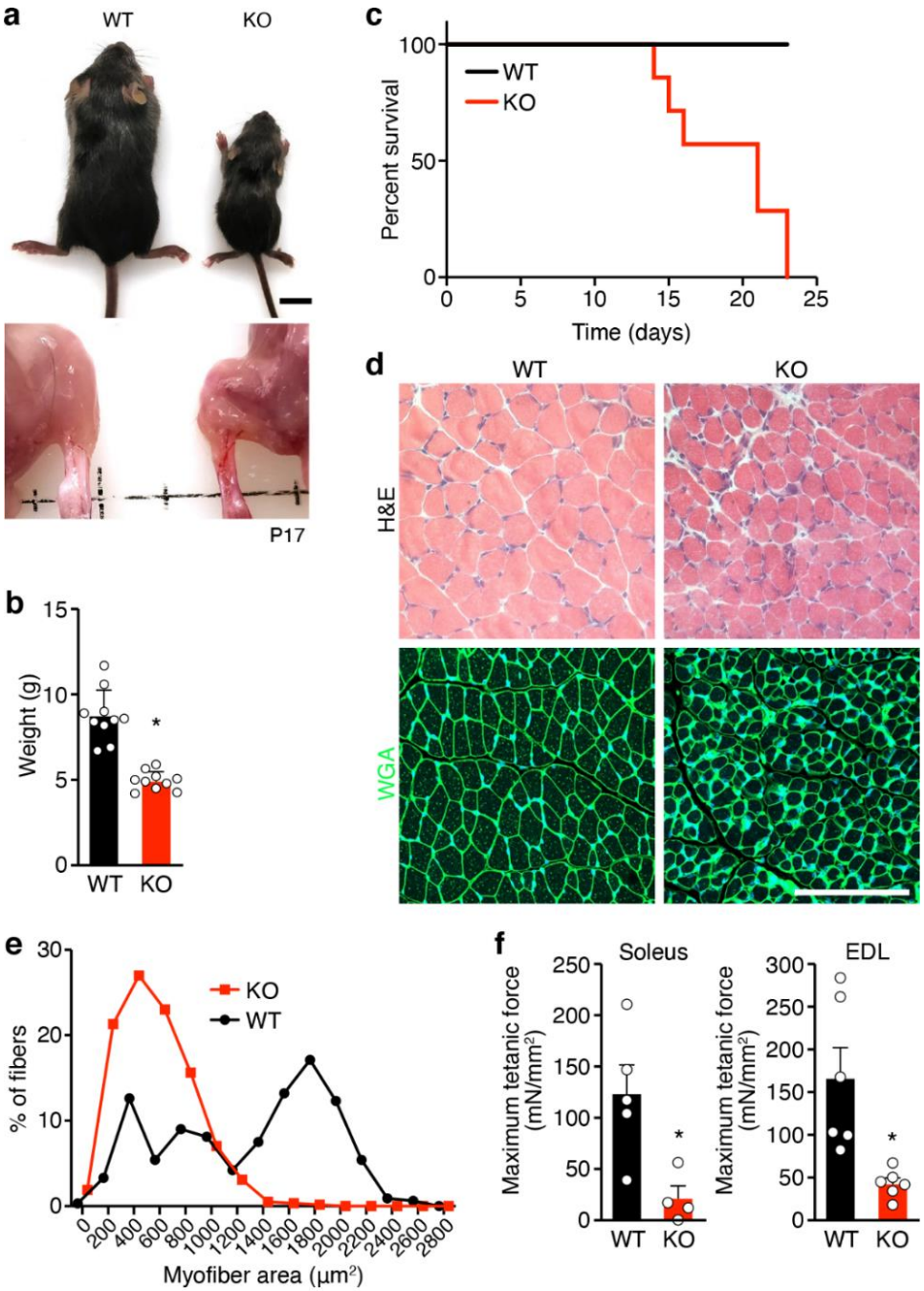
a
WT
KO
P17
b
Weight (g)
WT
KO
c
Percent survival
Time (days)
WT
KO
d
WT
KO
H&E
WGA
e
% of fibers
Myofiber area (μm²)
KO
WT
f
Soleus
EDL
Maximum tetanic force (mN/mm²)
WT
KO
g
WT
KO

Fig. 4. Net39 is required for normal muscle structure and function.

a. At P17, Net39 KO mice (upper panel) and their hindlimb muscles (lower panel) are abnormally small compared to WT mice. Scale bar: 1cm. **b.** Body weight of WT and Net39 KO mice at P17. n=10 mice per group. *p<0.05. **c.** Survival curve of Net39 KO mice. n=8 mice for WT and 7 mice for KO. **d.** H&E (upper panels) and wheat germ agglutinin (WGA) staining (lower panels) of WT and Net39 KO quadriceps muscle at P17**.** Scale bar: 100μm. **e.** Myofiber area distribution quantified using CellProfiler from WGA-stained quadriceps sections at P17. p<0.01. n=3 mice per group. **f.** *Ex vivo* contraction assay to measure maximum tetanic force of the indicated muscles at P17. EDL, Extensor digitorum longus. n=6 mice per group for EDL and n=4 for soleus. *****p<0.05. **g.** Electron micrographs show disorganized sarcomeres in Net39 KO diaphragms at P17. Red arrowheads show sarcomere disarray (left). Higher magnification of indicated areas (red box) are shown (right). Scale bars: 1μm. Statistical comparisons between groups were evaluated by unpaired Student's t-test.

Net39 maintains nuclear integrity

Net39 KO mice showed deformations of nuclear envelope architecture in longitudinal sections of different muscle types and their frequency increased with age (**Fig. 5a**). Immunohistochemistry for the nuclear envelope protein SUN2 showed that nuclear deformations were characterized by pronounced invaginations and projections that protruded into the sarcomeres (**Fig. 5b**). Electron microscopy revealed a jagged appearance of KO nuclear envelopes (**Fig. 5c**). Loss of nuclear envelope proteins like Lamin A/C can also cause nuclear deformations and susceptibility to mechanical stress[45]. Indeed, we observed that nuclear envelope deformations in KO EDL muscles increased mildly just after a short ex vivo mechanical stretch, whereas WT muscles were unaffected by stretch (**Fig. 5d**).

To further characterize the nuclear envelope deformations observed in Net39 KO muscles, we probed for changes in nuclear envelope proteins by western blot analysis in Net39 KO muscles and found that LMNB1 and LEMD2 signals were increased relative to WT muscle, whereas EMD levels were decreased. These results indicate changes in protein levels or post-translational changes in the regions recognized by the antibodies used (**Fig. 5e, f**). Interestingly, a homozygous missense mutation in *LEMD2* that causes arrhythmic cardiomyopathy in humans also leads to nuclear envelope deformations in cardiomyocytes resembling those seen in Net39 KO myonuclei[46], implying a common function. These results suggest that loss of Net39 compromises nuclear envelope integrity and causes dysregulation of its components.

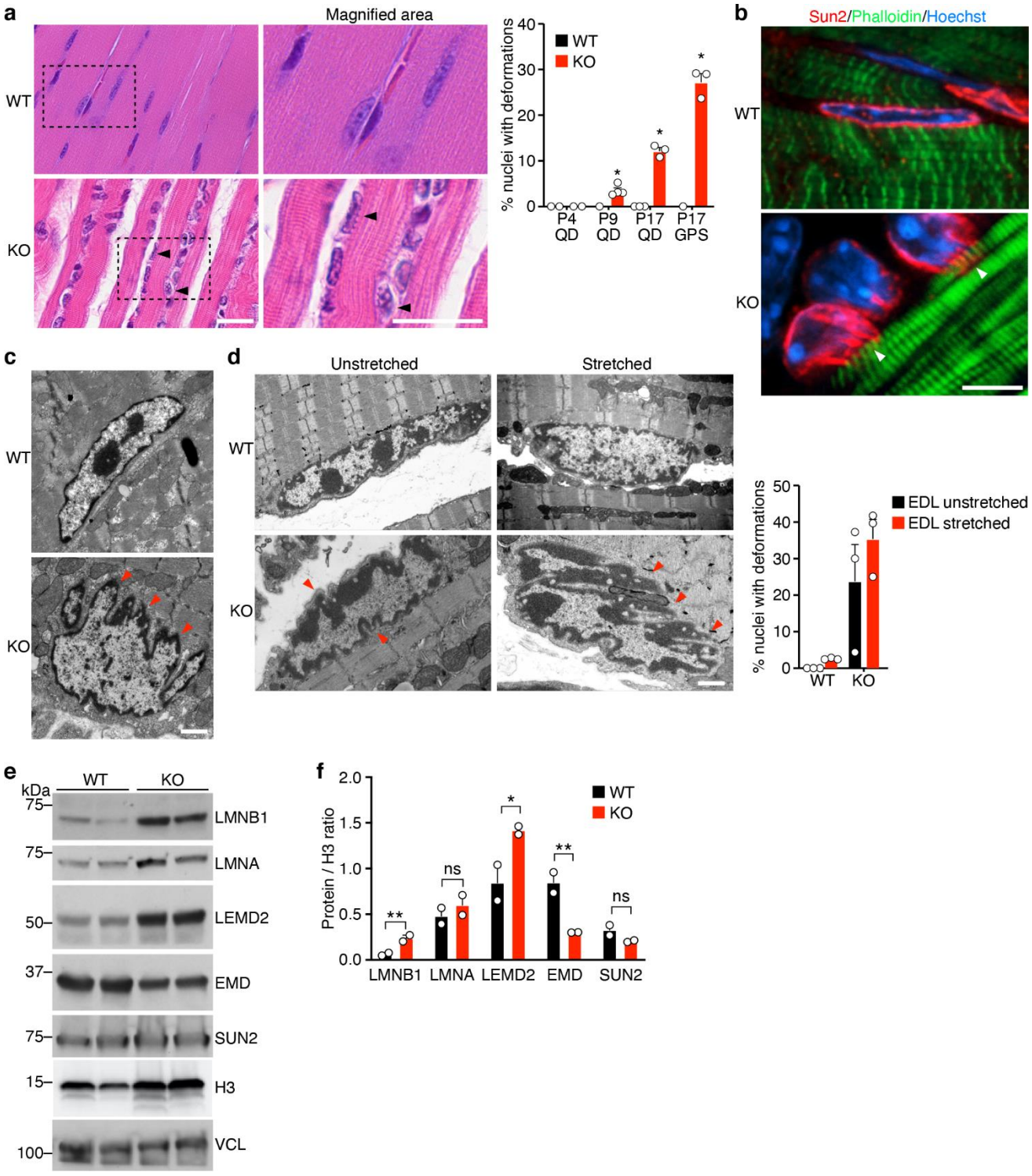

Fig. 5. Net39 maintains integrity of the nuclear envelope.

a. H&E staining of longitudinal quadriceps sections at P17 (left). Magnified images display the jagged outlines of the indicated nuclei. Arrowheads indicate nuclear envelope protrusions. Scale bar: 20μm. Quantification of the percentage of nuclei with nuclear envelope deformations in the indicated muscles and

timepoints (right). n=2 WT and KO mice *p<0.05. **b.** Immunofluorescence of the nuclear envelope in longitudinal quadriceps sections at P17 reveals nuclear envelope deformations. Sections were stained for the inner nuclear membrane protein Sun2 (red), phalloidin for F-actin (green), and Hoechst for DNA (blue). Arrowheads indicate nuclear envelope protrusions. Scale bar: 5μm. **c.** Electron micrographs of P17 quadriceps nuclei showing nuclear envelope defects in Net39 KO muscle. Arrowheads indicate nuclear envelope protrusions. Scale bar: 1μm. **d.** Electron micrographs of P17 EDL nuclei before and after *ex vivo* stretching (left) and quantification of the percentage of nuclei with nuclear envelope deformations (right). Arrowheads indicate nuclear envelope protrusions. Scale bar: 1μm. p=0.3. n=3 WT and KO mice. **e.** Western blot analysis showing protein levels of LMNB1, LMNA, LEMD2, EMD, and SUN2 in P17 quadriceps muscle lysates from WT and Net39 KO mice. Vinculin (VCL) and Histone H3 are loading controls for total protein and nuclear protein, respectively. **f.** Densitometry quantification of western blot from Fig. 2e. The intensity of each nuclear envelope protein was normalized to Histone H3 intensity. n= 2 biological replicates. *p<0.5, **p<0.01.

Net39 modulates genome organization and gene expression

Nuclear envelope proteins regulate the formation of genomic regions associated with lamins, called LADs[33,34]. We sought to profile global changes in LADs by performing Lamin A/C ChIP-seq in WT and Net39 KO muscles. We found that there was a significant loss of LADs and transcriptional start sites within the LADs in Net39 KO quadriceps muscles (**Fig. 6a**). We also assessed chromatin accessibility in WT and Net39 KO quadriceps using Assay for Transposase-Accessible Chromatin (ATAC) sequencing (**Fig. 6b**). Following Net39 deletion, we observed differential changes in chromatin accessibility in genes related to distinct pathways (**Fig. 6c**). The promoters of genes involved in lipid metabolism such as Acyl-CoA transferase 1 (*Acot1*) became more

accessible, whereas genes related to carbohydrate metabolism and muscle contraction such as fast fiber-type Myosin binding protein C (*Mybpc2*) became less accessible.

Changes in gene expression were profiled by RNA sequencing at early (P9) and late (P17) time points. Differences between KO and WT quadriceps were more pronounced over time (**Fig. 6d**). Differentially regulated genes correlated with the changes in their accessibility (**Fig. 6e**). An example of this correlation is Cysteine and glycine rich protein 3 (*Csrp3*), also known as muscle LIM protein (MLP), an inhibitor of myoblast differentiation[47]. *Csrp3* expression is affected by the loss of a LAD, which may facilitate chromatin opening and increased accessibility of its gene body, resulting in a concomitant increase in its mRNA expression (**Fig. 6f**). Pathway analysis showed that the upregulated genes in KO muscle, such as *Acot1* and *Csrp3*, were mainly involved in lipid and muscle processes (**Fig. 6g**). In contrast, the downregulated genes were related to carbohydrate metabolism, cell cycle and mitotic division (**Fig. 6g**). Downregulated cell cycle genes such as *Cdk1* and *Aurkb* control nuclear envelope assembly and disassembly by regulating chromosomal condensation[48], whereas kinesins (*Kif4*, *Kif22*) have been shown to be required in muscle for nuclear positioning[49]. We observed alterations in expression of myosin heavy chain genes and key sarcomeric components including myozenin-1, myosin binding protein C, myosin light chain 1, and tropomyosin 1, which likely contributes to sarcomere disarray observed in the diaphragm.

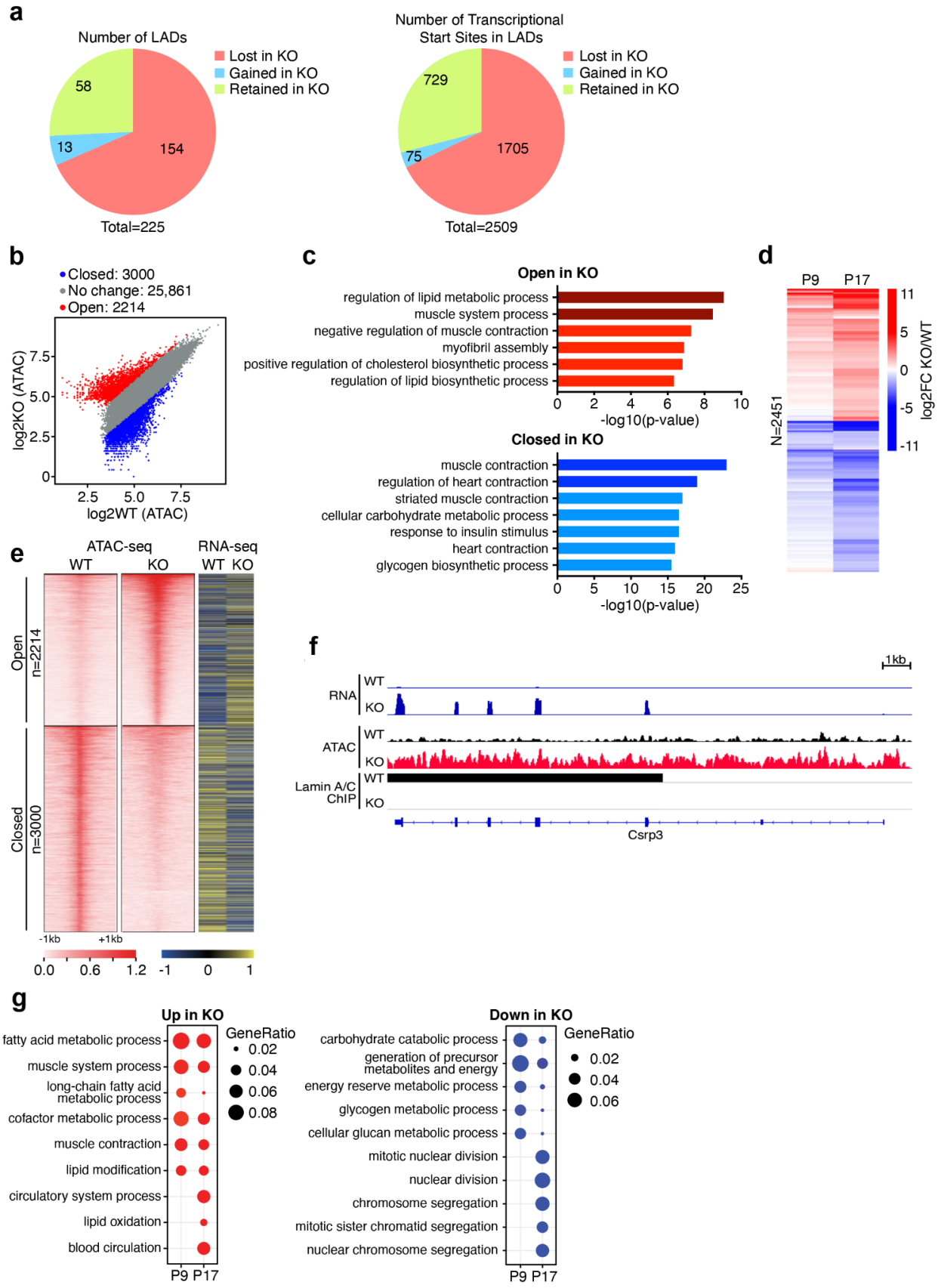
a
Number of LADs
Lost in KO
Gained in KO
Retained in KO
58
13
154
Total=225
Number of Transcriptional Start Sites in LADs
729
75
1705
Total=2509
b
Closed: 3000
No change: 25,861
Open: 2214
log2KO (ATAC)
log2WT (ATAC)
c
Open in KO
regulation of lipid metabolic process
muscle system process
negative regulation of muscle contraction
myofibril assembly
positive regulation of cholesterol biosynthetic process
regulation of lipid biosynthetic process
-log10(p-value)
Closed in KO
muscle contraction
regulation of heart contraction
striated muscle contraction
cellular carbohydrate metabolic process
response to insulin stimulus
heart contraction
glycogen biosynthetic process
-log10(p-value)
d
P9
P17
N=2451
log2FC KO/WT
e
ATAC-seq
RNA-seq
WT
KO
Open n=2214
Closed n=3000
-1kb
+1kb
f
1kb
RNA
ATAC
Lamin A/C ChIP
Csrp3
g
Up in KO
fatty acid metabolic process
muscle system process
long-chain fatty acid metabolic process
cofactor metabolic process
muscle contraction
lipid modification
circulatory system process
lipid oxidation
blood circulation
GeneRatio
Down in KO
carbohydrate catabolic process
generation of precursor metabolites and energy
energy reserve metabolic process
glycogen metabolic process
cellular glucan metabolic process
mitotic nuclear division
nuclear division
chromosome segregation
mitotic sister chromatid segregation
nuclear chromosome segregation
P9 P17

Fig. 6. Loss of Net39 causes changes in chromatin accessibility and gene expression.

a. Chart illustrating the number of Lamin-Associated Domains (LAD) and the number of transcriptional start sites (TSS) within LADs that are lost (red), gained (blue), or retained (green) from Lamin A/C Chromatin Immunoprecipitation sequencing (ChIP-seq) in Net39 KO quadriceps compared to WT at P17. n=2 WT and KO mice. **b.** Scatter plot with all detected peaks in P17 quadriceps ATAC-seq (n=3). A cutoff of fold change > 2 and an adjusted p-value < 0.05 was set for the identification of differentially open and closed peaks in Net39 KO samples**. c.** Pathways enriched by GREAT analysis of open or closed chromatin peaks in Net39 KO samples compared to WT. **d.** Heatmap showing fold change of up- and down-regulated genes in KO muscle at P9 (n=3) and P17 (n=3) as determined by RNA-seq. A cutoff of fold change > 2 and an adjusted p-value < 0.05 was set for the identification of differentially expressed genes. **e.** Heatmap of open- and closed-regulated ATAC-seq peaks (left panels) and the expression level of associated genes as determined by RNA-seq (right panel). **f.** Distributions of RNA-seq, ATAC-seq, and Lamin A/C ChIP-seq peaks at the Cysteine and glycine rich protein 3 (Csrp3) locus in WT and KO muscles. WT: black, KO: red for ATAC-seq and Lamin A/C ChIP-seq. **g.** GO terms enriched among up- (left) and down-regulated (right) genes by RNA-seq. Circle sizes indicate the ratio of genes included in the pathway.

Transcriptional changes in Net39 KO mice affect muscle fiber type and metabolism

To further explore the functional consequences of transcriptional alterations, we analyzed the fiber-type composition of KO muscle. Immunohistochemical staining showed that Net39 KO quadriceps exhibited a shift towards an oxidative fiber composition (type I and type IIa) (**Fig. 7a**). An increase in oxidative metabolism was also evidenced by NADH and COX staining on quadriceps muscle (**Fig. 7b**). To determine whether the increase in oxidative

metabolism is a result of increased mitochondria biogenesis, we examined the mitochondrial DNA content by qPCR in quadriceps muscle samples, as well as transcript levels of the regulator of mitochondrial biogenesis PGC1α. We observed no differences between WT and Net39 KO mice (data not shown). Therefore, we conclude that the increased oxidative metabolism in Net39 KO muscle is not due to an increased number of mitochondria.

To better understand the changes in metabolism, we performed targeted metabolomics on WT and Net39 KO hindlimb muscle (**Fig. 7c, d**), and observed increases in fatty acid species and decreases in glycolysis intermediates (**Fig. 7e, f**). Overall, Net39 deletion caused a shift from carbohydrate to lipid metabolism in skeletal muscle, which may contribute to increased oxidative activity[50]. Serum glucose levels were significantly decreased in Net39 KO mice compared to WT, but no changes were observed in other serum metabolites, or circulating insulin (**Fig. 7g**). Hypoglycemia has also been observed in mouse models of EDMD, in which *Lmna* is either deleted or mutated[51,52].

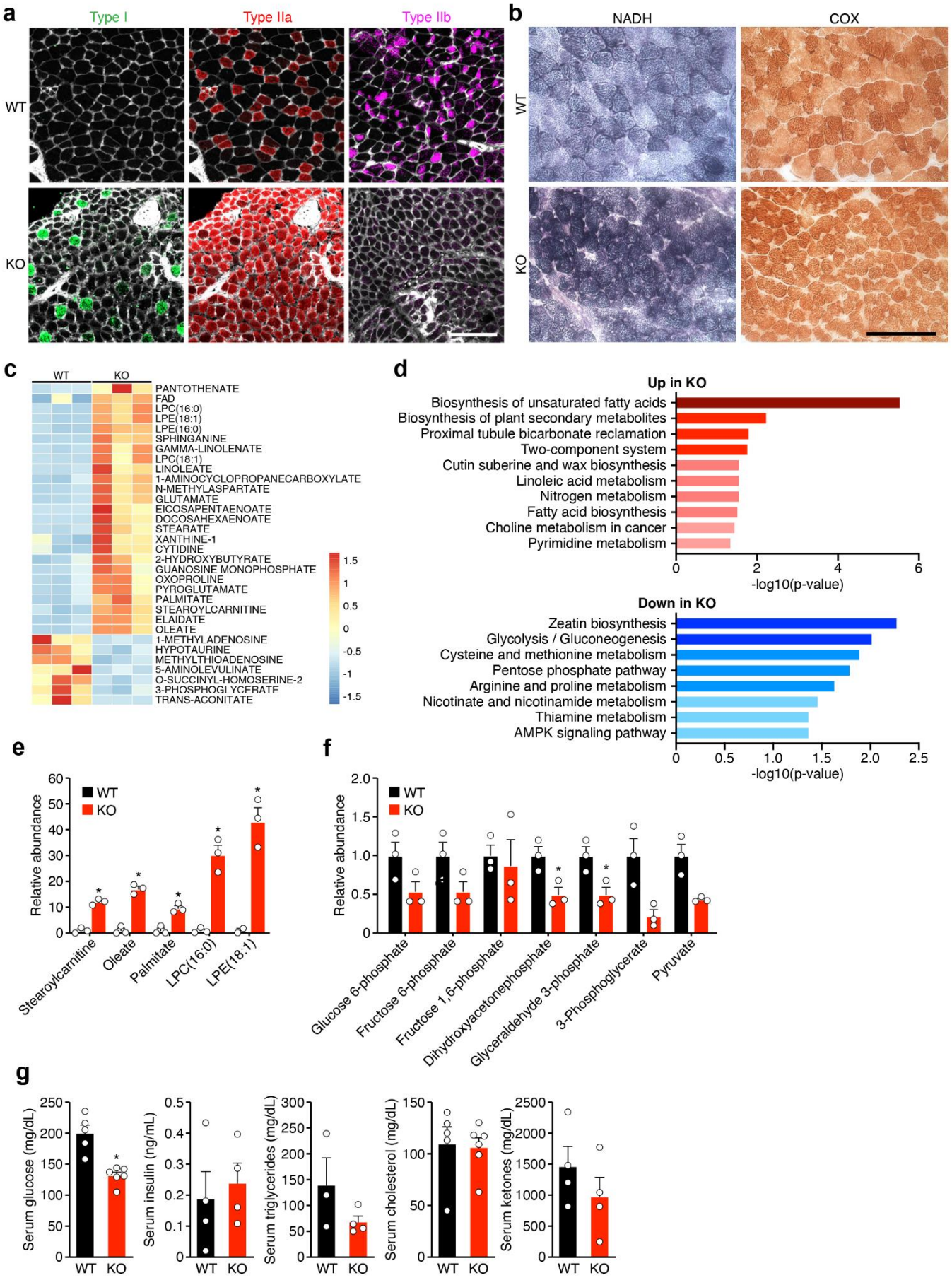
a
Type I
Type IIa
Type IIb
WT
KO
b
NADH
COX
WT
KO
c
WT
KO
PANTOTHENATE
FAD
LPC(16:0)
LPE(18:1)
LPE(16:0)
SPHINGANINE
GAMMA-LINOLENATE
LPC(18:1)
LINOLEATE
1-AMINOCYCLOPROPANECARBOXYLATE
N-METHYLASPARTATE
GLUTAMATE
EICOSAPENTAENOATE
DOCOSAHEXAENOATE
STEARATE
XANTHINE-1
CYTIDINE
2-HYDROXYBUTYRATE
GUANOSINE MONOPHOSPHATE
OXOPROLINE
PYROGLUTAMATE
PALMITATE
STEAROYLCARNITINE
ELAIDATE
OLEATE
1-METHYLADENOSINE
HYPOTAURINE
METHYLTHIOADENOSINE
5-AMINOLEVULINATE
O-SUCCINYL-HOMOSERINE-2
3-PHOSPHOGLYCERATE
TRANS-ACONITATE
1.5
1
0.5
0
-0.5
-1
-1.5
d
Up in KO
Biosynthesis of unsaturated fatty acids
Biosynthesis of plant secondary metabolites
Proximal tubule bicarbonate reclamation
Two-component system
Cutin suberine and wax biosynthesis
Linoleic acid metabolism
Nitrogen metabolism
Fatty acid biosynthesis
Choline metabolism in cancer
Pyrimidine metabolism
0
2
4
6
-log10(p-value)
Down in KO
Zeatin biosynthesis
Glycolysis / Gluconeogenesis
Cysteine and methionine metabolism
Pentose phosphate pathway
Arginine and proline metabolism
Nicotinate and nicotinamide metabolism
Thiamine metabolism
AMPK signaling pathway
0
0.5
1.0
1.5
2.0
2.5
-log10(p-value)
e
Relative abundance
WT
KO
Stearoylcarnitine
Oleate
Palmitate
LPC(16:0)
LPE(18:1)
f
Relative abundance
WT
KO
Glucose 6-phosphate
Fructose 6-phosphate
Fructose 1,6-phosphate
Dihydroxyacetonephosphate
Glyceraldehyde 3-phosphate
3-Phosphoglycerate
Pyruvate
g
Serum glucose (mg/dL)
Serum insulin (ng/mL)
Serum triglycerides (mg/dL)
Serum cholesterol (mg/dL)
Serum ketones (mg/dL)
WT
KO

Fig. 7. Net3 mice exhibit a shift in oxidative metabolism.

a. Immunohistochemistry of WT and Net39 KO quadriceps sections at P17 showing type I (green), type IIa (red), and type IIb (purple) myofibers. Sections were co-stained with WGA (white). Scale bar: 100μm. **b.** Staining of WT and Net39 KO quadriceps at P17 for nicotinamide adenine dinucleotide (NADH), succinic dehydrogenase (SDH) and cytochrome C oxidase (COX). Scale bar: 100μm. **c.** Heatmap showing upregulated and downregulated metabolites in Net39 KO quadriceps at P17, as analyzed by targeted metabolomics. n=3 mice per group. **d.** GREAT analysis of metabolic pathways enriched among upregulated (top) and downregulated (bottom) metabolites in Net39 KO quadriceps. **e.** Relative levels of selected elevated fatty acids and lysophospholipids in Net39 KO quadriceps at P17**.** WT was used as reference. *p<0.05. **f.** Levels of detected glycolysis intermediates in Net39 KO quadriceps at P17. WT was used as reference. *p<0.05. **g.** Serum glucose, insulin, triglycerides, cholesterol, and ketones levels in WT and Net39 KO mice at P17 were measured using VITROS clinical diagnostics. n=3-6 mice per group. *p<0.05. Statistical comparisons between groups were evaluated by unpaired Student’s t-test.

2.3. Loss of Net39 in adult muscle causes progressive myopathy

Conditional deletion of Net39 in adult muscle

Global loss of Net39 causes juvenile lethality due to impaired muscle function, thus preventing analysis of adult mice[53]. To understand the role of Net39 in muscle maintenance, we generated a Net39 conditional allele in mice ($Net39^{fl}$). loxP sequences were inserted flanking the first exon of Net39 using CRISPR/Cas9-mediated homology-directed repair (**Fig. 8a**). $Net39^{fl}$ mice were bred with mice carrying a tamoxifen-inducible Cre recombinase transgene under control of the skeletal muscle-specific human skeletal actin promoter (HSA-CreERT2). Tamoxifen was injected intraperitoneally in male $Net39^{fl/fl}$ (control group, Ctrl) and $Net39^{fl/fl}$, HSA-CreERT2 mice (conditional deletion in skeletal muscle, cKO) at 2 months of age for 5 consecutive days (**Fig. 8b**). Genomic excision by recombination was observed in muscle but not in other tissues by PCR analysis (**Fig. 8c**), and reduced Net39 mRNA and protein levels in Net39 cKO muscles were confirmed by qRT-PCR (**Fig. 8d**) and western blot analysis (**Fig. 8e**), respectively.

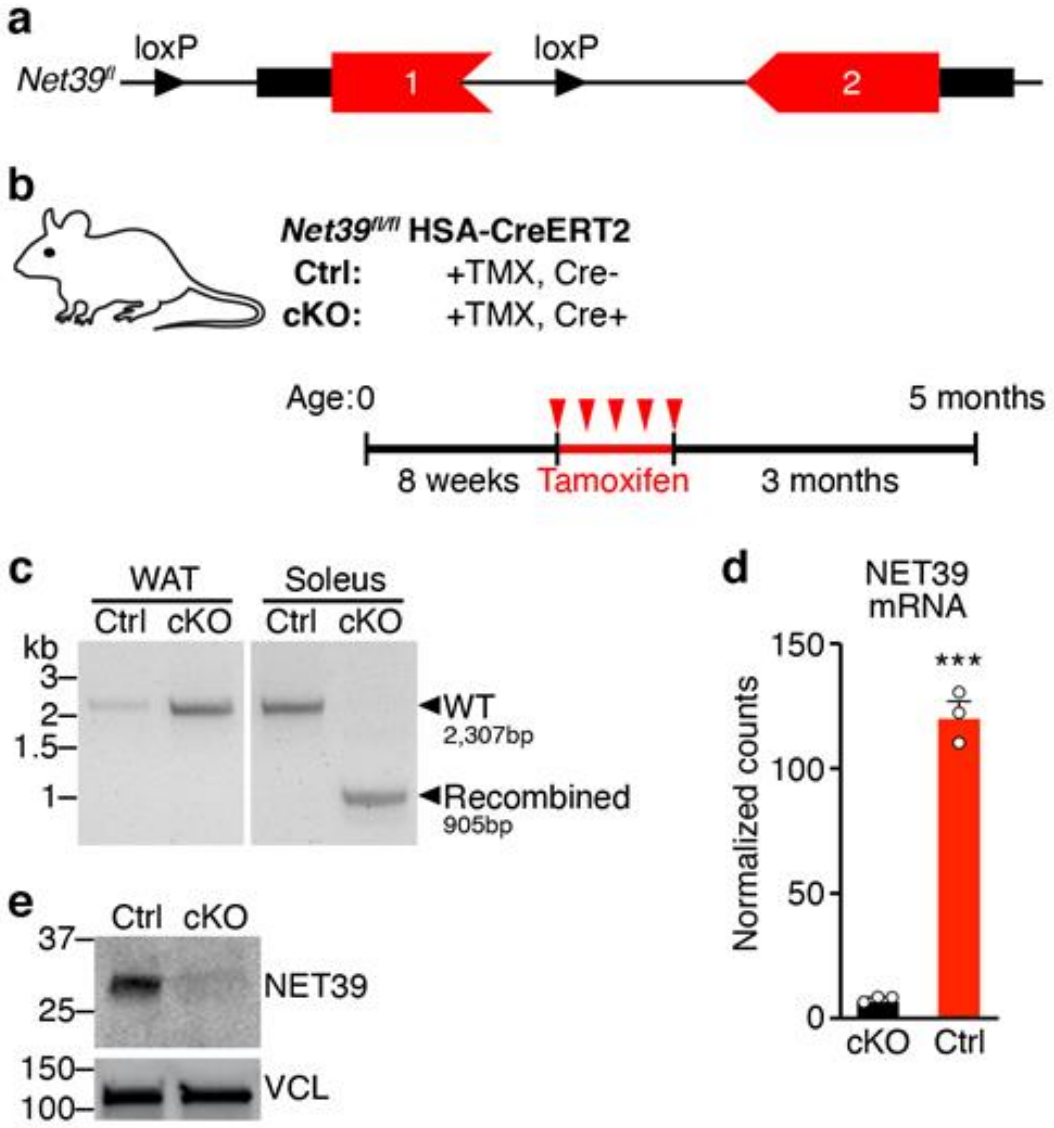

Fig. 8. Conditional deletion of Net39.

a. Gene structure of the conditional allele for *Net39* (*Net39*^{fl}). Black arrowheads indicate the location of the loxP sequences inserted. Boxes represent exons. Black boxes denote untranslated regions and red boxes indicate open reading frame. **b.** Experimental set up for deletion of Net39 in adult skeletal muscle. Control (Ctrl) and Net39 cKO (cKO) mice were injected tamoxifen and analyzed at the indicated times. **c.** PCR analysis showing genomic recombination of the Net39 locus only in cKO soleus muscles. WAT: White adipose tissue. **d.** qRT-PCR analysis showing loss of Net39 RNA in GP muscle 3 months after tamoxifen injection in cKO mice. **e.** Western blot analysis showing loss of Net39 protein in quadriceps muscle 1 month after tamoxifen injection in cKO mice.

Net39 is required for adult muscle maintenance

Three months after tamoxifen treatment, Net39 cKO mice displayed reduced mass of gastrocnemius plantaris (GP) and tibialis anterior (TA) muscles, but not total body mass, compared to control. (**Fig. 9a**). To assess muscle function, ex vivo contractility assays were performed. Soleus and EDL muscles of Net39 cKO mice showed reduced maximum tetanic force, indicating compromised contractility (**Fig. 9b**). Hematoxylin and eosin, and wheat germ agglutinin (WGA) staining of skeletal muscles revealed a reduction in myofiber cross-sectional area in cKO compared to control mice (**Fig. 9c, d**). Net39 KO mice show a homogenous decrease in myofiber size. In contrast, we observed variations in myofiber size across Net39 cKO muscles. No centralized nuclei or fibrosis were observed in Net39 cKO muscles, and serum CK levels did not change between control and cKO mice (data not shown). Whole hindlimb immunofluorescence of myofiber types revealed the appearance of type I, small, angular myofibers in gastrocnemius muscles (**Fig. 9e**) To understand myofiber heterogeneity in Net39 cKO muscles, additional histological analyses were performed. Small angular fibers in Net39 cKO GP muscles showed increased NADH and COX staining (**Fig. 9f**), and were positive for desmin, embryonic myosin, and cleaved caspase-3 (**Fig. 9g**), indicating that they are myopathic and degenerative. Ultrastructural analysis of GP muscles by electron microscopy showed defects in sarcomere organization in the smaller, thinner myofibers, and compromised nuclear envelope integrity (**Fig. 9h**). These results indicate that adult loss of Net39 causes heterogeneous muscle degeneration that impairs muscle maintenance.

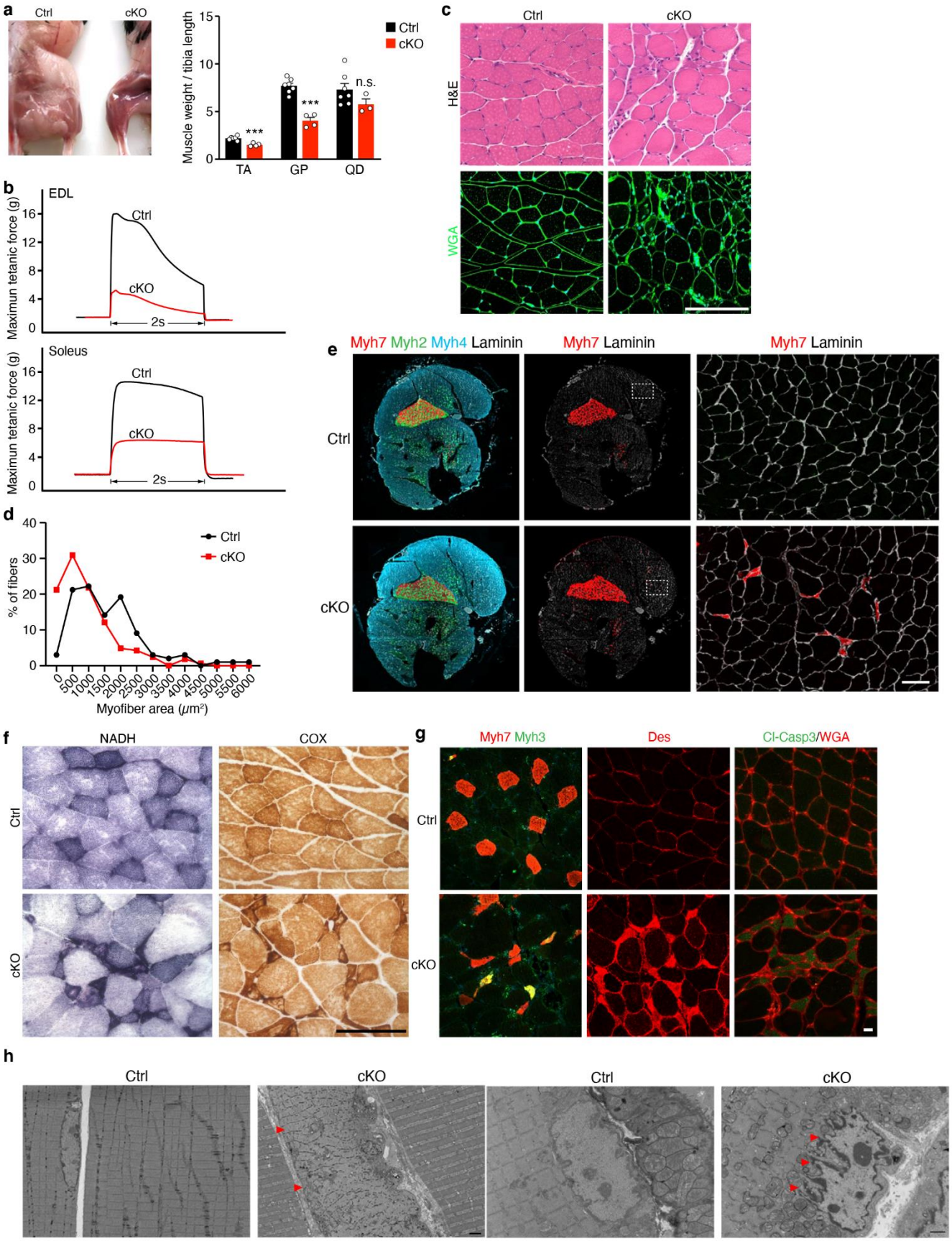
a
Ctrl
cKO
Muscle weight / tibia length
15
10
5
0
Ctrl
cKO
***
***
n.s.
TA
GP
QD
b
EDL
Maximun tetanic force (g)
16
12
8
4
0
Ctrl
cKO
2s
Soleus
Maximun tetanic force (g)
16
12
8
4
0
Ctrl
cKO
2s
c
Ctrl
cKO
H&E
WGA
d
% of fibers
40
30
20
10
0
Ctrl
cKO
0
500
1000
1500
2000
2500
3000
3500
4000
4500
5000
5500
6000
Myofiber area (μm²)
e
Myh7 Myh2 Myh4 Laminin
Myh7 Laminin
Myh7 Laminin
Ctrl
cKO
f
NADH
COX
Ctrl
cKO
g
Myh7 Myh3
Des
Cl-Casp3/WGA
Ctrl
cKO
h
Ctrl
cKO
Ctrl
cKO

Fig. 9. Net39 is required for adult muscle maintenance.

a. Dissection of Ctrl and Net39 cKO hindlimb muscles 3 months after tamoxifen treatment (left). Muscle weight to tibia length ratios for the indicated muscles in Ctrl and Net39 cKO mice 3 months after tamoxifen treatment (right). TA: Tibialis anterior, GP: Gastrocnemius plantaris, QD: Quadriceps. **b.** *Ex vivo* contraction assay to measure maximum tetanic force of the indicated muscles in Ctrl and Net39 cKO muscles 3 months after tamoxifen. EDL: Extensor digitorum longus. **c.** H&E (upper panels) and wheat germ agglutinin (WGA) staining (lower panels) of Ctrl and Net39 cKO GP muscles 3 months after tamoxifen treatment. Scale bar: 100μm. **d.** Myofiber area distribution quantified using CellProfiler from WGA-stained GP sections. **e.** Whole hindlimb immunofluorescence for type I (Myh7), type IIa (Myh2) and type IIb (Myh4) myofibers of Ctrl and Net39 cKO mice 3 months after tamoxifen treatment. The magnified area shows the presence of small angular fibers positive for Myh7 in Net39 cKO GP. Scale bar: 100μm. **f.** Staining of Ctrl and Net39 cKO GP muscles 3 months after tamoxifen treatment for nicotinamide adenine dinucleotide (NADH) and cytochrome C oxidase (COX). Scale bar: 100μm**. g.** Immunofluorescence for type I (Myh7) and embryonic (Myh3) myosins (left), Desmin (middle), and cleaved Caspase-3 and wheat-germ agglutinin (right) in Ctrl and Net39 cKO mice 3 months after tamoxifen treatment. Scale bar: 20μm **h.** Electron micrographs showing disorganized sarcomeres (left, red arrowheads) and nuclear envelope deformations (right, red arrowheads) in Net39 cKO GP muscles 3 months after tamoxifen treatment. Scale bar: 1μm

Loss of Net39 causes myonuclear-specific transcriptional changes

Net39 was previously shown to control gene expression by regulating the regions of DNA associated with lamins (termed lamin-associated domains, LADs). To profile the transcriptional changes caused by adult loss of Net39, transcriptomic analysis was performed by bulk RNA sequencing (bulk RNA-seq) in GP muscles (**Fig. 10a**). Pathway analysis of differentially expressed genes

showed that upregulated genes were preferentially involved the immune response (such as Cd74 Ctss, and Msr1), cytoskeleton/extracellular matrix (Enah, Baiap2, Itgax, Fgf16) and p53 signaling (Casp3, Cdkn1a, Rprm) (**Fig. 10b**). Downregulated genes were enriched in pathways related to glucagon/insulin (such as Fbp2, Pfkm and Pygm), and calcium signaling (Calm1, Atp2a1, Nos1) (**Fig. 10b**). Although gene expression of metabolic genes was altered in Net39 cKO muscles, no changes in blood serum metabolites were observed (data not shown).

Skeletal muscle is a tissue with diverse cell populations, and the nuclei within myofibers differ in their function and gene expression profiles[54]. To understand the heterogeneous changes in Net39 cKO mice, single-nucleus RNA sequencing (snRNA-seq) was performed in control and Net39 cKO GP muscles. Unsupervised clustering identified distinct nuclear populations that were assigned to biological populations based on the expression of marker genes (**Fig. 10c, d**). We observed a new myonuclear population recently reported to be potentially involved in muscle fiber repair and remodeling (Remodeling, Rem), but we were not able to identify tenocytes in our dataset. The relative abundance of each nuclear population was then quantified (**Fig 10e**). Net39 cKO muscles presented increases in type I myonuclei (2.9% to 21.9), and decreased percentage of type IIb myonuclei (52.3% to 41.6%) and fibro-adipogenic precursors (FAPs) (10.7% to 4.4%). The increase in type I myonuclei did not match a decrease in another single nuclear population, suggesting that multiple myonuclear populations may transition into myopathic, embryonic-like, type I myonuclei instead. Next, we integrated bulk RNA-seq and snRNA-seq datasets (**Fig. 10f**). We observed that the biggest changes in bulk RNA-seq could be mainly attributed to transcriptional

differences in type I and remodeling myonuclei. Thus, single nucleus transcriptomic analysis indicated that the abnormalities in Net39 cKO muscles are caused by the combined changes in distinct myonuclear populations within myofibers.

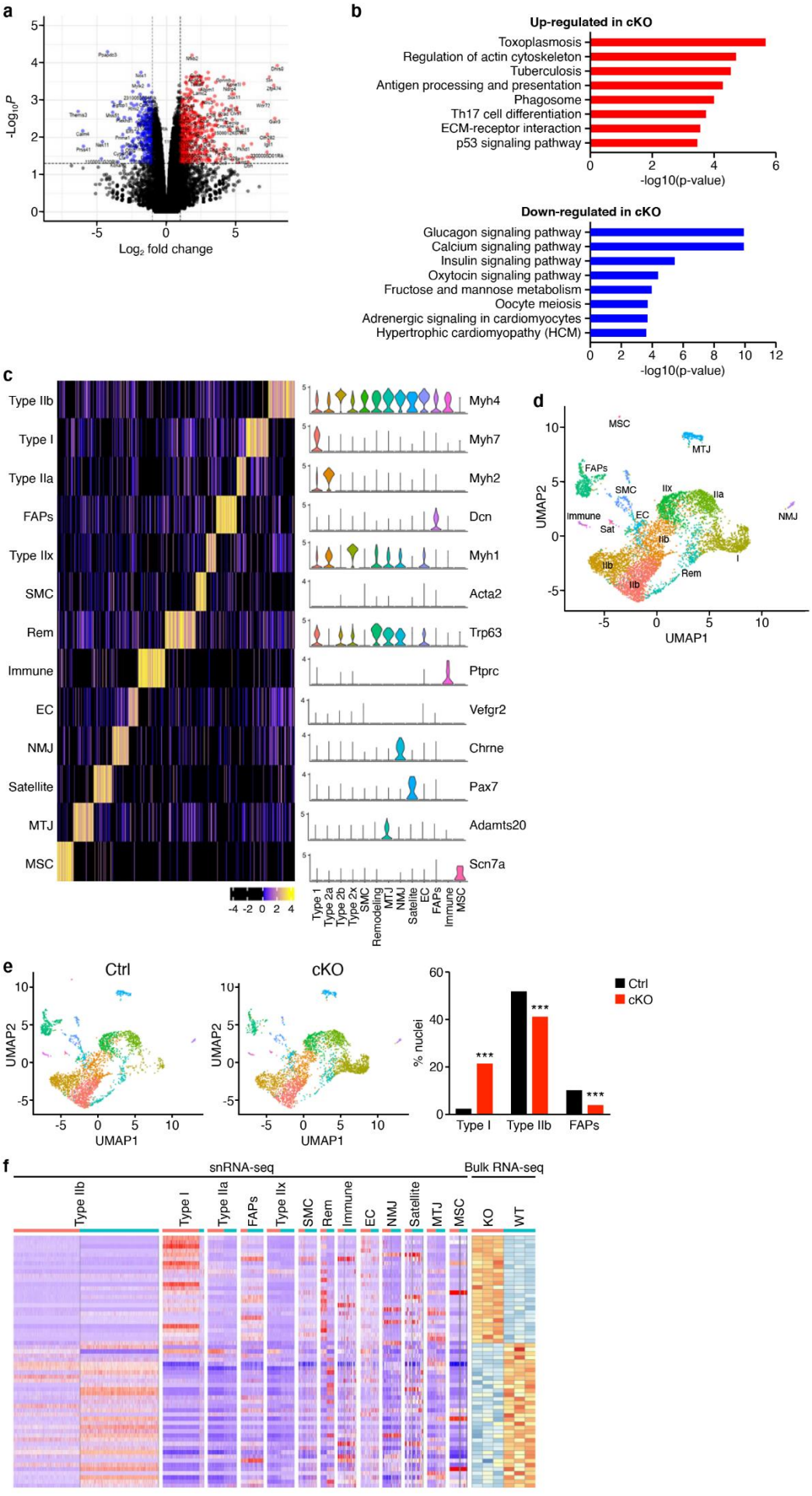
a
-Log10P
Log2 fold change
b
Up-regulated in cKO
Toxoplasmosis
Regulation of actin cytoskeleton
Tuberculosis
Antigen processing and presentation
Phagosome
Th17 cell differentiation
ECM-receptor interaction
p53 signaling pathway
-log10(p-value)
Down-regulated in cKO
Glucagon signaling pathway
Calcium signaling pathway
Insulin signaling pathway
Oxytocin signaling pathway
Fructose and mannose metabolism
Oocyte meiosis
Adrenergic signaling in cardiomyocytes
Hypertrophic cardiomyopathy (HCM)
-log10(p-value)
c
Type IIb
Type I
Type IIa
FAPs
Type IIx
SMC
Rem
Immune
EC
NMJ
Satellite
MTJ
MSC
Myh4
Myh7
Myh2
Dcn
Myh1
Acta2
Trp63
Ptprc
Vefgr2
Chrne
Pax7
Adamts20
Scn7a
Type 1
Type 2a
Type 2b
Type 2x
SMC
Remodeling
MTJ
NMJ
Satellite
EC
FAPs
Immune
MSC
d
MSC
MTJ
FAPs
SMC
IIx
IIa
Immune
EC
NMJ
Sat
IIb
I
Rem
UMAP1
UMAP2
e
Ctrl
cKO
UMAP1
UMAP2
% nuclei
Type I
Type IIb
FAPs
***
f
snRNA-seq
Bulk RNA-seq
Type IIb
Type I
Type IIa
FAPs
Type IIx
SMC
Rem
Immune
EC
NMJ
Satellite
MTJ
MSC
KO
WT

Fig. 10. Loss of Net39 causes myonuclear-specific transcriptional changes

a. Volcano plot illustrating the up- and down-regulated genes in Ctrl and Net39 cKO GP muscles 3 months after tamoxifen treatment by bulk RNA-seq. A cutoff of fold change > 2 and an adjusted p-value < 0.05 were set for the identification of differentially expressed genes. **b.** Pathway analysis of up- and down-regulated genes in Ctrl and Net39 cKO GP muscles 3 months after tamoxifen treatment by bulk RNA-seq. **c.** Heatmap showing cluster-specific genes identified in distinct nuclear populations by snRNA-seq. The colors indicate z-score (left)**.** Violin plots showing the expression of selected marker genes in each population (right). **d.** UMAP visualization of nuclear transcriptomes from Ctrl and Net39 cKO GP muscles 3 months after tamoxifen treatment by snRNA-seq (7,296 nuclei), colored by cluster identity. **e.** UMAP visualization of Ctrl (3,566 nuclei) (left) and Net39 cKO (3,730 nuclei) (middle) nuclear transcriptomes by snRNA-seq. Quantification of the percentage of nuclei corresponding to the indicated populations in Ctrl and Net39 cKO samples (right). **f.** Heatmaps showing the expression of the top 30 up- and down-regulated genes by bulk RNA-seq (right) and their expression in different nuclear populations by snRNA-seq (left) in Ctrl and Net39 cKO GP muscles 3 months after tamoxifen treatment. Color indicates Z-score. UMAP: Uniform manifold approximation and projection for dimension reduction, FAPs: Fibro-adipogenic progenitors, SMC: Smooth muscle cells, Rem: Remodeling myonuclei, EC: Endothelial cells, NMJ: Neuromuscular junction myonuclei, MTJ: Myotendinous junction myonuclei, MSC: Mesenchymal stem cells.

Mef2c is upregulated in Net39 cKO muscles

To interrogate the molecular pathways altered in Net39 cKO muscle, the transcriptomic changes of all myonuclear populations were merged and upstream regulator analysis was performed (**Fig. 11a**). The promoters of the down-regulated genes in Net39 cKO myonuclei were enriched in targets for AR, Nfat, Mef2, and Nf1, whereas the up-regulated myonuclei genes were primarily Mef2

targets. Furthermore, bulk RNA-seq and western blot analysis revealed increased Mef2c transcript (**Fig. 11b**) and protein levels (**Fig. 11c**) in Net39 cKO and KO muscles. Mef2c immunofluorescence showed increased Mef2c positive nuclei in Net39 cKO muscles (**Fig. 11d**). Based on these observations, we hypothesized that Net39 may regulate Mef2c activity to control muscle gene expression.

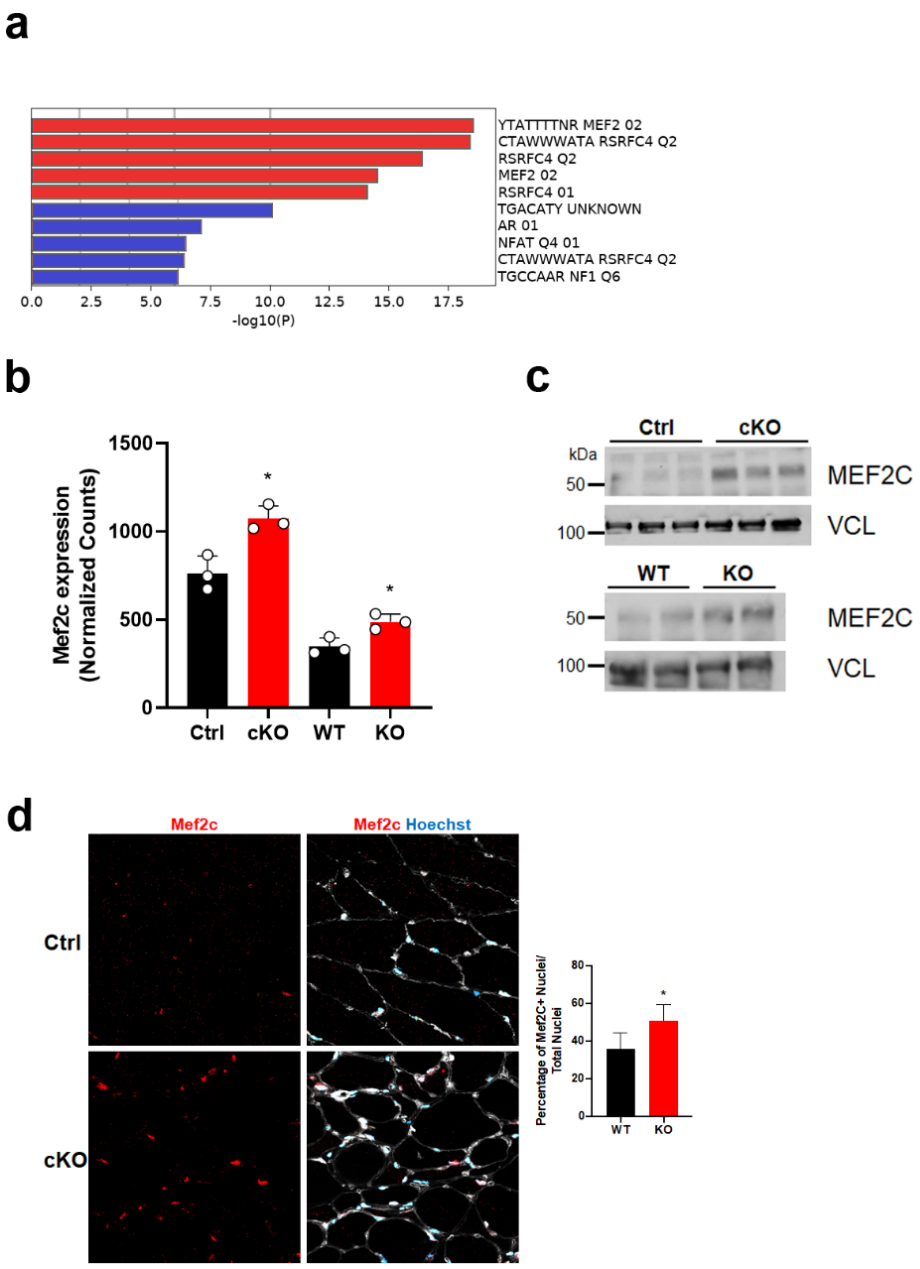

Fig. 11. Mef2c is upregulated in Net39-deficient muscles.

a. Transcription factor enrichment among upregulated (red) and downregulated (blue) genes among the myonuclear transcripts. **b.** Transcript levels of Net39 mRNA in the indicated mouse models as detected by RNA-seq. **c.** Protein levels of Net39 in the indicated mouse models as detected by western blot analysis. For Ctrl and cKO, GP muscles were analyzed 3 months after tamoxifen injection. For WT and KO, P17 quadriceps muscles were analyzed. Vinculin (VCL) is a loading control. **d.** Mef2c immunofluorescence in Ctrl and cKO transverse sections of GP muscles 3 months after tamoxifen injection (left). Quantification of nuclei positive for Mef2c staining (right). *$p<0.05$. Statistical comparisons between groups were evaluated by unpaired Student's t-test.

2.4. Molecular studies on Net39

Net39 associates with the LEM-Lamin complex

We used proximity biotinylation (BioID) to unbiasedly assess if Net39 associated with other nuclear envelope proteins in C2C12 myotubes. Indeed, we found that Net39 is associated with multiple components of the nuclear envelope such as LEMD2, SUN2, and EMD (**Fig. 12a**). In contrast to prior studies[17], we did not observe interaction between Net39 and lamin A. We further validated the interaction between NET39 and nuclear envelope proteins by co-immunoprecipitation (**Fig. 12b**). Remarkably, a human mutation in *LEMD2* causes nuclear envelope deformations in cardiomyocytes, which are similar to the ones observed in Net39 KO and cKO mice[46]. LEMD2 and EMD are LEM proteins, which interact with lamins to indirectly tether DNA to the nuclear periphery[32]. To examine the potential role of Net39 in that process, ChIP-seq was performed in vitro by overexpressing 3xTy1-Net39 in C2C12 myotubes. Net39 has no known DNA binding domain, and it associated with DNA at low efficiency, indicating that, as in the case of LEM proteins, DNA binding is likely indirect. The peaks observed by ChIP-seq were long and broad (average length: 3.9Mb) and strongly resembled the DNA binding profile of lamin B1 in C2C12 cells, which has been previously determined by DamID[44] (**Fig. 12c**). Genome-wide comparison between Net39 ChIP-seq and lamin B1 DamID revealed a high degree of correlation (**Fig. 12d**). These results indicate that Net39 associates with the LEM-Lamin complex, a group of proteins with important roles in maintaining envelope integrity and genome organization.

Net39 regulates the transcription factors Mef2c and MyoR

DNA regions associated with lamins (LADs), LEM proteins, or Net39, are megabases long and encompass a significant part of the total genome (30-45%). While Net39 has been shown to tether genomic loci to the nuclear periphery for silencing[17,44], we did not observe a genome-wide correlation between active or inactive genes based on their presence in LADs by lamin A ChIP-seq (data not shown). Instead, our in vivo data suggest that the nuclear envelope may provide an additional regulatory scaffold for protein-protein and protein-DNA interactions to control the expression of specific genes inside or outside LADs. Prior studies showed that forced Mef2 activation is sufficient to cause fiber type switching in vivo[55]. Therefore, the regulation of Mef2c activity by Net39 could contribute to the histological and functional changes observed in Net39 cKO mice. To assess Mef2c activity, the enhancer of Desmin (DesMef), a bona fide Mef2c target, was used in reporter experiments[56]. We generated DesMef-LacZ, Net39 KO mice, and observed increased X-gal staining in Net39 KO GP muscles compared to WT (**Fig. 12e**). In vitro, overexpression of Net39 in N2a cells was sufficient to repress Mef2c activation of a luciferase reporter under the control of DesMef (**Fig. 12f**). These results indicate that Net39 directly represses Mef2c activity.

To identify additional direct Net39 downstream targets, RNA-seq was performed in vitro under conditions where Net39 was exogenously upregulated (Net39 overexpression in C2C12 myoblasts) or downregulated (Net39 knock-down in C2C12 myotubes) (**Fig. 12g**). From all the genes identified, MyoR/Musculin showed a strong, opposite regulation in both conditions. MyoR (myogenic repressor), is a transcription factor that antagonizes MyoD[57] (**Fig. 12h**). MyoR is highly expressed in myoblasts, and Net39 overexpression

repressed its transcript levels by 50%. In contrast, MyoR is usually repressed in myotubes, but it was strongly upregulated when Net39 was knocked-down. MyoR was also elevated in Net39 KO muscles (**Fig. 12i**). In vitro, knock-down of Net39 impairs myotube formation[17], and upregulation of MyoR likely contributes to the phenotype. We hypothesize that Net39 may control gene expression by directly or indirectly regulating transcription factors like Mef2c or MyoR, whereas the interactions with LEM proteins likely contribute to its role in preserving nuclear envelope integrity (**Fig. 12j**). Additional experiments are being performed to further validate and understand the direct effectors of Net39 function.

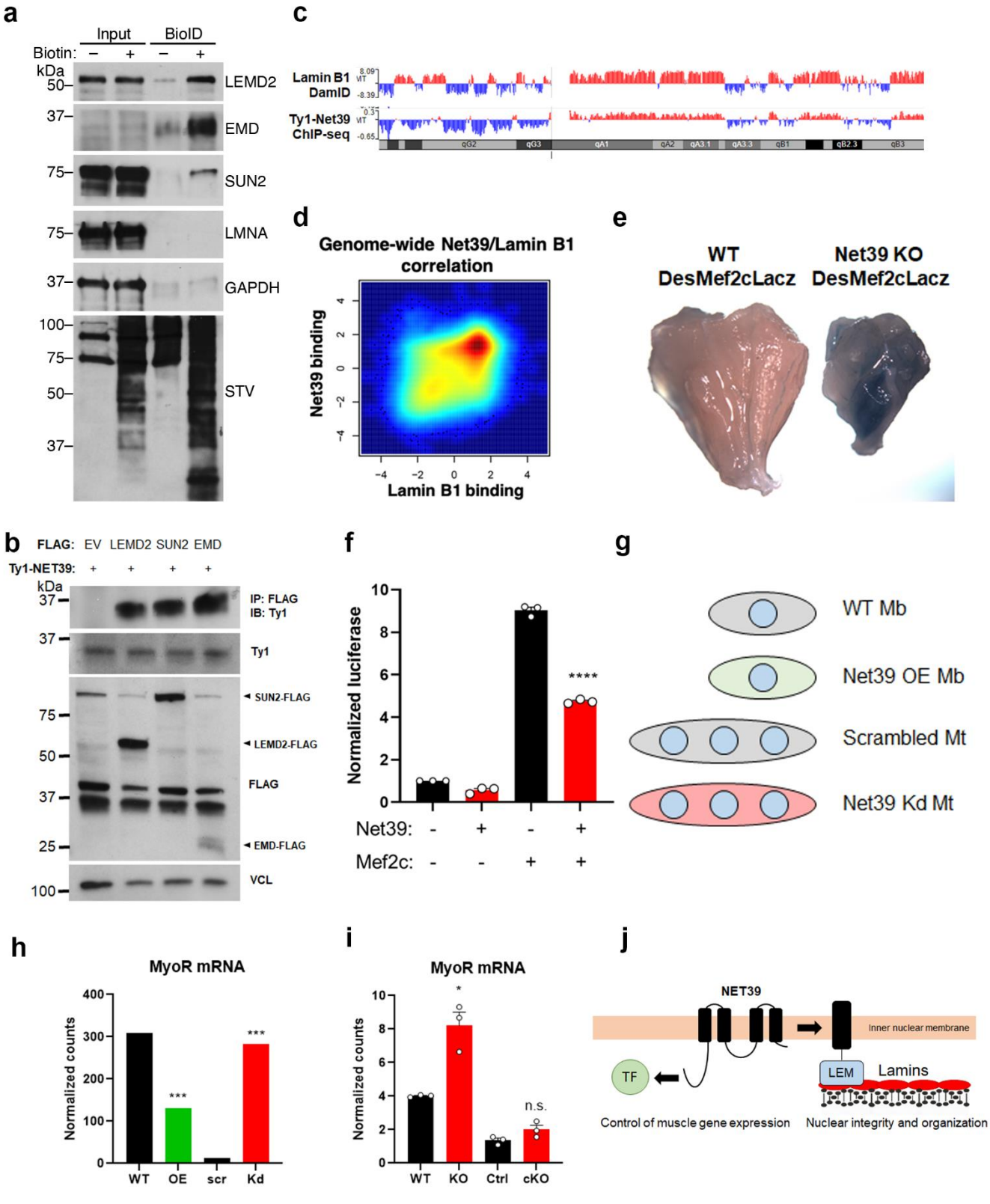
a
Input
BioID
Biotin: – + – +
kDa
50–
LEMD2
37–
EMD
75–
SUN2
75–
LMNA
37–
GAPDH
100–
75–
50–
37–
STV
c
Lamin B1 DamID
Ty1-Net39 ChIP-seq
qG2
qG3
qA1
qA2
qA3.1
qA3.3
qB1
qB2.3
qB3
d
Genome-wide Net39/Lamin B1 correlation
Net39 binding
Lamin B1 binding
e
WT DesMef2cLacz
Net39 KO DesMef2cLacz
b
FLAG: EV LEMD2 SUN2 EMD
Ty1-NET39: + + + +
kDa
IP: FLAG
IB: Ty1
Ty1
SUN2-FLAG
LEMD2-FLAG
FLAG
EMD-FLAG
VCL
f
Normalized luciferase
****
Net39: - + - +
Mef2c: - - + +
g
WT Mb
Net39 OE Mb
Scrambled Mt
Net39 Kd Mt
h
MyoR mRNA
Normalized counts
***
***
WT
OE
scr
Kd
i
MyoR mRNA
Normalized counts
*
n.s.
WT
KO
Ctrl
cKO
j
NET39
Inner nuclear membrane
TF
LEM
Lamins
Control of muscle gene expression
Nuclear integrity and organization

Fig. 12. Molecular studies on Net39.

a. Net39 BioID in C2C12 myotubes detects enrichment of biotinylated LEMD2, SUN2, and EMD but not Lamin A in C2C12 myotubes. GAPDH is a loading control. Total biotinylated proteins were detected using streptavidin-HRP (STV). **b.** Validation of Net39 interaction with LEMD2, EMD and SUN2 by co-immunoprecipitation in C2C12 myotubes. VCL is a loading control. **c.** Genome browser tracks for Lamin B1 DamID and Ty1-Net39 ChIP-seq performed in C2C12 myotubes. Signal was normalized to input. **d.** Graph showing genome-wide peak intensity correlation between Lamin B1 DamID and Ty1-Net39 ChIP-seq performed in C2C12 myotubes. For each genomic location, the levels of Net39 and Lamin B1 binding are represented. Color denotes the abundandce of peaks with that intensity (blue: low, red: high). Both signals are proportional to each other and a linear correlation can be observed **e.** Whole-mount X-gal staining of GP muscles at P17 performed in WT and Net39 KO mice transgenic for LacZ under control of DesMef enhancer, a reporter of Mef2 activity. **f.** Luciferase assays with DesMef reporter. The three Mef2c binding sites of the Desmin enhancer were cloned into a luciferase reporter. Luciferase activity was measured in the presence or absence of Mef2c and Net39. **g.** Experimental design to identify direct Net39 targets. RNA-seq was performed in myoblasts (Mb) overexpressing Net39 (OE) or an empty vector (WT), and in myotubes (Mt) were Net39 was knocked-down (Net39 Kd) or a scrambled shRNA was used. Genes with opposite regulation patterns between both conditions were selected for analysis. **h.** MyoR mRNA transcript levels from in vitro experiments in C2C12 as determined by bulk RNA-seq. scr: Scrambled. **i**. MyoR mRNA transcript levels in WT and KO P17 quadriceps muscles and in Ctrl and Net39 cKO GP muscles 3 months after tamoxifen treatment as determined by bulk RNA-seq. **j.** Proposed model for Net39 function. Net39 directly and indirectly regulates the activity of specific transcription factors to regulate muscle gene expression. Net39 is also required to preserve nuclear integrity and organization, and that function is potentially mediated by its association with the LEM-lamin complex.

2.5. Involvement of Net39 in human disease

Characterization of human Net39 mutations

Several new human mutations in *NET39* have been identified as novel alleles associated with EDMD[43] (**Fig. 13a**). One mutant variant of *NET39* showed reduced tethering of the *PTN* locus in vitro. However, besides a single correlative study, the actual contribution of *NET39* mutations to disease has not been analyzed. A homozygous single nucleotide polymorphism (SNP) in *NET39* (c.644G>A, p.R215H) (**Fig. 13a**) was observed by whole-exome sequencing in a patient with an unresolved case of Limb-Girdle muscular dystrophy (LGMD) (Dr. V. Straub, University of Newcastle, personal communication). The patient presented childhood onset myopathy, fiber type disproportion, proximal muscle weakness in upper and lower limbs, no cardiac involvement, and cognitive impairment. The patient did not present any mutations known to cause LGMD. Western blot analysis and densitometry of muscle biopsies showed a modest reduction in NET39 protein levels (-28%) (**Fig. 13b**), and histological analysis revealed sporadic abnormalities in muscle nuclear envelope integrity (**Fig. 13c**).

NET39 R215 is a residue conserved between mice and humans. We generated a humanized mouse model carrying the mutation (Net39^{R215H}) using CRISPR/Cas9-mediated homology-directed repair. Heterozygous Net39^{R215H} mice were crossed to each other, pups were born at Mendelian ratios and littermates were indistinguishable. Histological analysis was performed in 1 year old WT and Net39$^{R215H/R215H}$ mice (**Fig. 13d**). No differences between genotypes were observed by hematoxylin and eosin or NADH-TR staining. Overall, these results suggest that the NET39 R215H mutation alone does not cause EDMD in mice. Future studies will be required to understand the potential role of NET39

R215H as a disease modifier, and to generate additional humanized mouse models to study other Net39 mutations. Work from other groups and ours may help underscore the importance of Net39 in EDMD and warrant its consideration in future genetic studies of myopathic patients.

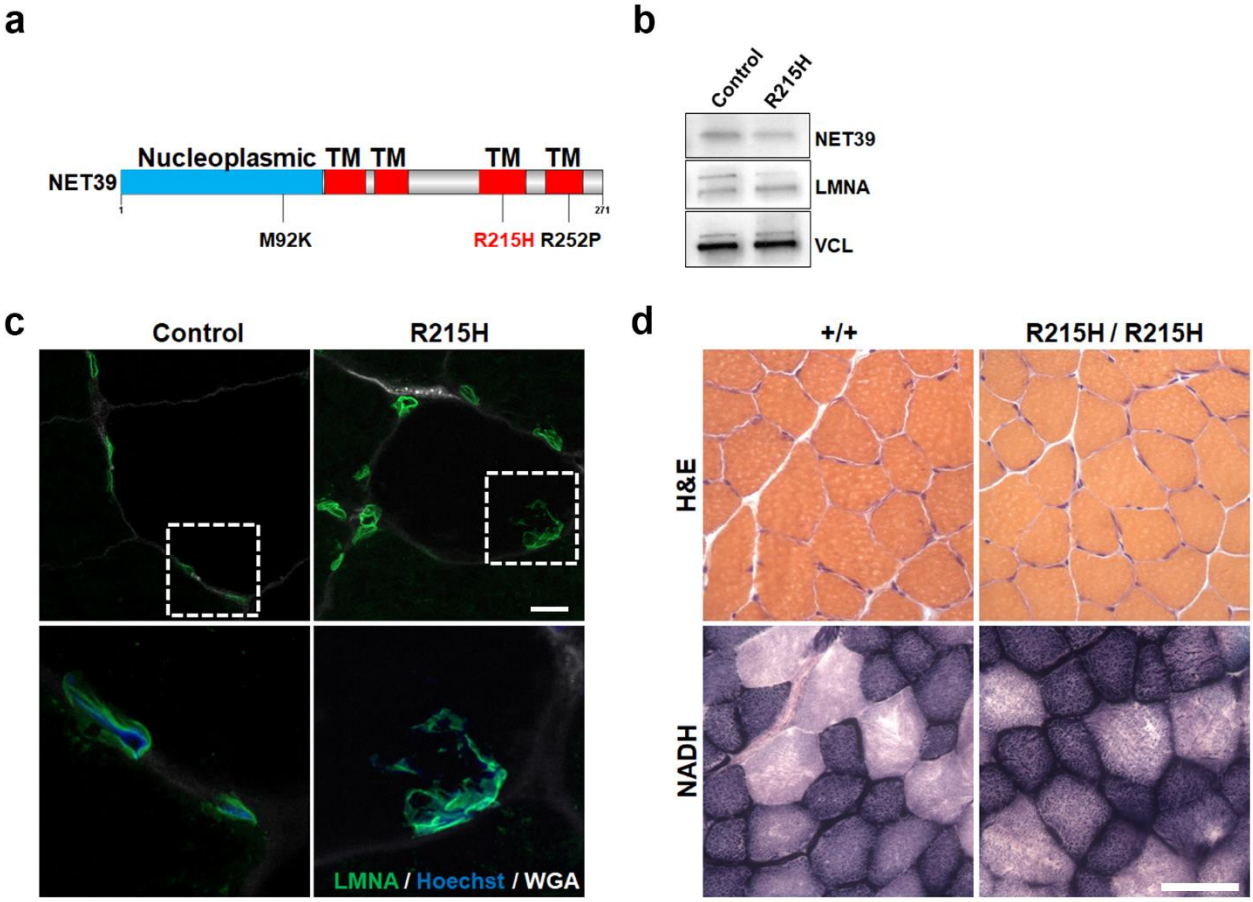

Fig. 13. Characterization of Net39^{R215H}.

a. Protein structure of NET39. Blue denotes the N-terminal nucleoplasmic region. TM denotes predicted transmembrane domains. Highlighted residues indicate human alleles previously reported to have potential links to EDMD (M92K, R252P) or characterized in this study (R215H). **b.** Western blot analysis for NET39 protein levels in a muscle biopsy from a patient with a homozygous NET39 R215H mutation and an age-matched control. LMNA and VCL were used as loading controls. **c.** Immunofluorescence for LMNA in transverse muscle sections from a patient with a homozygous NET39 R215H mutation and an age-

matched control. Magnified area indicates sporadic abnormalities in the nuclear envelope. WGA: Wheat-germ agglutinin. Scale bar 20μm.: **d.** Histological analysis of transverse GP muscle sections from 1-year old WT and Net39$^{R215H/R215H}$ mice. No differences were observed by hematoxylin and eosin (H&E) or nicotinamide adenine dinucleotide (NADH) staining. Scale bar: 100μm.

Net39 is downregulated in EDMD

EDMD is a complex disease and there are multiple mouse models that reflect its genetic diversity and broad range of manifestations[28]. The early lethality and nuclear envelope dysregulation observed in Net39 KO mice prompted us to compare the Net39 KO phenotype with other mouse models of severe EDMD. One such model carries a Lmna ΔK32 mutation, a single amino acid deletion that impairs the lateral assembly of lamin A/C[58]. In humans, the Lmna ΔK32 mutation causes severe congenital muscular dystrophy[59]. We observed overlapping phenotypes between Lmna ΔK32 mice[51] and our Net39 KO mice. Both mouse models manifest early lethality, nuclear abnormalities, failure to grow and metabolic alterations. Furthermore, it was recently reported that Lmna ΔK32 myotubes show downregulation of Net39 transcript and protein levels[60]. These findings raised the possibility that Net39 expression may be affected in EDMD patients and may contribute to the pathogenesis of the disease.

To determine whether Net39 is downregulated in EDMD, we examined Net39 expression in muscle biopsies from patients with EDMD caused by different missense mutations in the *LMNA* gene (**Fig. 14a**). We found that NET39 protein levels were decreased by >80% in these muscles (**Fig. 14b, c**), with a concomitant decrease in *NET39* transcript (**Fig. 14d**). Protein levels of another

muscle-enriched nuclear envelope protein, LEMD2, were unchanged in EDMD patients.

We hypothesized that, because loss of Net39 in mice causes severe muscle defects, restoration of Net39 expression in EDMD may ameliorate the disease. Ongoing experiments are being performed to explore the therapeutic potential of Net39. These experiments involve overexpression of Net39 in EDMD mouse models by muscle-specific transgenes or by delivery of adeno-associated virus (AAV). To ensure muscle-specific expression, Net39 was cloned into an AAV backbone under control of the muscle-specific muscle creatine kinase promoter (CK8e)[61]. To track viral infection, a cleavable GFP sequence was included in the open reading frame (GFP-2A-Net39). The construct was packaged into AAV2/9, a pseudotyped viral vector containing AAV2 rep and AAV9 cap proteins. AAV2/9 shows specific tropism for striated muscle[62]. As a proof of principle, Net39 was delivered into two Net39 KO mice by AAV at P6 by intraperitoneal injection at a concentration of 5×10^{13} vg/kg. qRT-PCR analysis of one AAV-Net39 injected mouse showed increased Net39 expression (**Fig. 14e**) and rescue of growth (**Fig. 14f**) and muscle abnormalities (**Fig. 14g**). One Net39 KO mouse was indistinguishable from WT and was still alive one year after injection. These preliminary data indicate that AAV delivery of Net39 is sufficient to rescue complete loss of Net39 in vivo, and it could be a potential intervention to treat other EDMD mouse models.

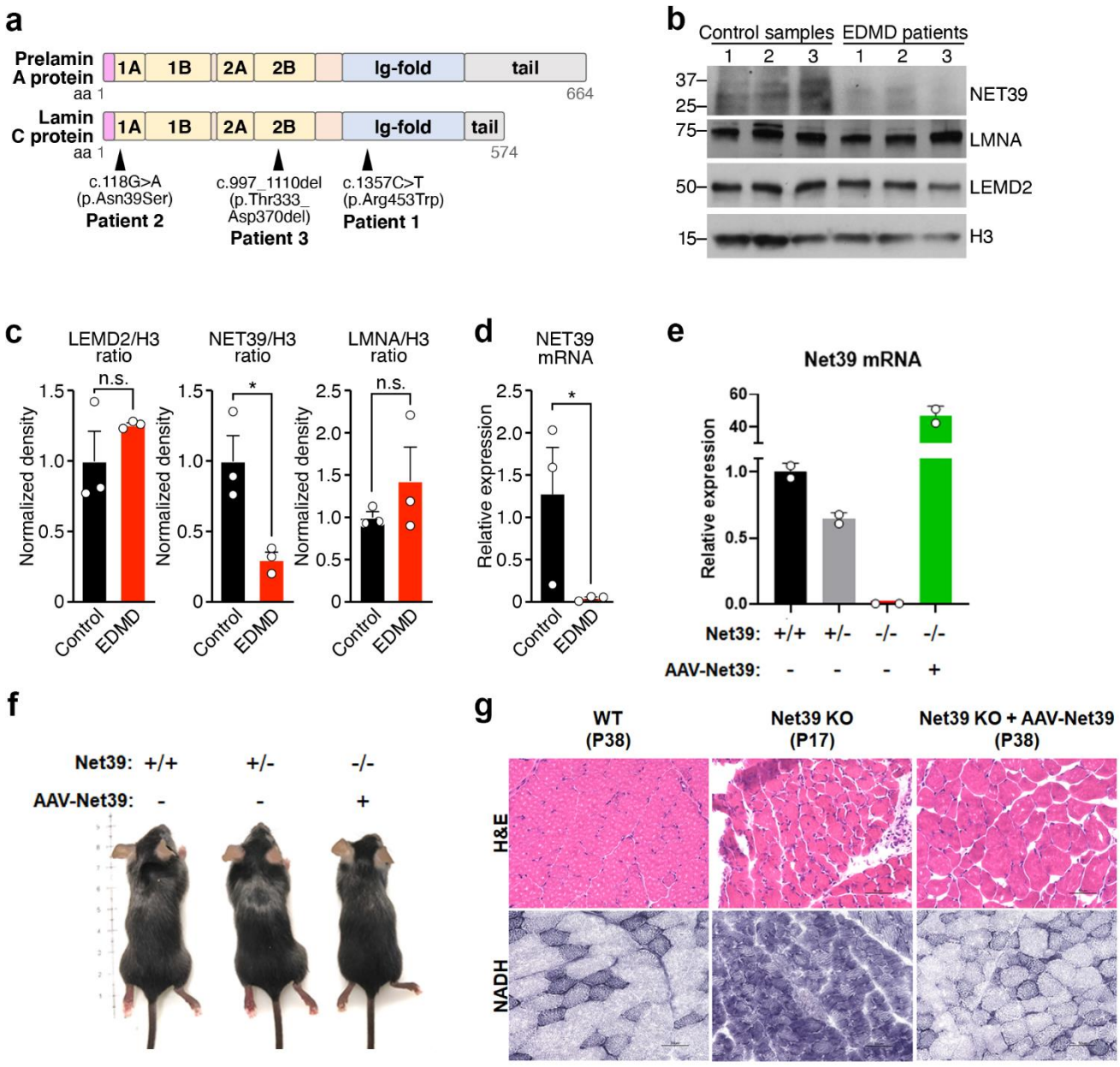

Fig. 14. Net39 is downregulated in EDMD.

a. Illustration of Lamin A/C protein domains highlighting specific mutations in three Emery-Dreifuss muscular dystrophy (EDMD) patients. In the Lamin A/C protein domains, pink indicates head region, yellow denotes rod domains, blue shows Ig-fold and gray indicates the tail regions of lamin C and prelamin A. **b**. Western blot analysis of human muscle biopsies from healthy (control) individuals and EDMD patients showing NET39, LMNA, and LEMD2 protein expression. Histone H3 (H3) was used as a nuclear loading control. **c.** Densitometry of western blots shown in (b) was performed and the ratios of LEMD2/H3 NET39/H3

and LMNA/H3 (p=0.3454) were quantified. n= 3 biologically independent samples. Data are presented as mean values +/- SEM. Statistical comparisons between groups were evaluated by unpaired and two-sided Student's t-test. * indicates p-value <0.05. **d.** qRT-PCR analysis of Net39 transcript in control and EDMD patient biopsy samples. Net39 mRNA expression in patient samples is normalized to its expression in control samples. p=0.0445. n= 3 biologically independent samples. Data are presented as mean values +/- SEM. Statistical comparisons between groups were evaluated by unpaired, one-tailed Student's t-test. **e.** qRT-PCR analysis to quantify Net39 mRNA levels in GP muscles from WT, heterozygous, Net39 KO and Net39 KO mice treated with adeno-associated virus (AAV) encoding for Net39. Net39 KO GP muscles were analyzed at P17, as early death precludes later timepoints. The other mice were analyzed at P38. Each sample is a technical replicate. **f.** Mice from the prior panel (e), at P38, showing recovery of survival and body size in Net39 KO mice treated with AAV-Net39. **g.** Histological analysis of transverse GP muscle sections from WT (P38) Net39 KO (P17) and Net39 KO mice treated with AAV-Net39 (P38). Hematoxylin and eosin (H&E) and nicotinamide adenine dinucleotide (NADH) were performed. WT and AAV-Net39 treated Net39 KO mice were histologically similar to each other.

2.6. Discussion and future directions

Our findings reveal an essential role for Net39 in muscle growth and function. The loss of Net39 leads to compromised nuclear envelope integrity in addition to changes in chromatin organization, gene expression, and muscle metabolism. Mice lacking Net39 fail to thrive, display reduced muscle growth and function, and eventually succumb to lethality. This phenotype is reminiscent of severe congenital muscular dystrophy, which can be produced by some Lamin A/C deletions or mutations[51,52,63]. In contrast, deletion of Net39 in adult muscle causes a slow, progressive, and heterogenous myopathic phenotype, which resembles common skeletal muscle manifestations of EDMD[36]. The nuclear deformations observed in Net39 KO and cKO mice have also been reported in Lamin A/C-deficient fibroblasts, as well as in models or individuals in which nuclear envelope proteins are mutated[45,46].

Generating a Net39 KO mouse model allowed us to understand the role of a tissue-specific nuclear envelope protein in vivo. Net39 expression is restricted to skeletal muscle and deletion of Net39 caused more nuclear deformations in gastrocnemius plantaris soleus (GPS) muscles than in quadriceps muscle. Muscle groups can be differentially affected under pathological conditions such as muscular dystrophy[64]. We propose that heterogeneity in Net39 expression (enriched in fast-twitch muscle), mechanical burden, and fiber-type composition may account for subtle phenotypical differences across muscles. With an in vivo model, we were also able to examine the contribution of Net39 to muscle metabolism. Net39 KO mice presented a fiber-type switch towards oxidative fibers with concomitant changes in contractility and metabolism but no changes in total mitochondrial number. Those

metabolic changes are similar to those described for other envelopathies[51,52]. Further mechanistic studies should be performed to understand how Net39 controls multiple processes in muscle, including growth, metabolism, and contractility.

Myogenesis and muscle maintenance require the activation of distinct transcriptional programs in a timewise manner[5]. Comparison between Net39 KO, cKO and AAV-mediated rescue of KO enabled us to dissect the contribution of Net39 to these processes. Embryonic myogenesis occurs at E11.5 and E14.5, but during the first weeks of age of mice, skeletal muscle undergoes extensive maturation, growth, and mechanical stress caused by muscle contraction and body movement[7]. Net39 is strongly induced postnatally, and delivery of Net39 by AAV to Net39 KO mice at P6 was sufficient to prevent myopathy and death. These data indicate that Net39 is essential for postnatal adaptations of skeletal muscle but not for embryonic myogenesis. Net39 KO mice presented widespread myofiber abnormalities across whole muscles. In contrast, in cKO muscles only certain myofibers appeared to be affected. These fibers were smaller, angular, presented immature/myopathic markers, and their number increased at later timepoints after tamoxifen treatment. Understanding the heterogeneity in the Net39 cKO phenotype will be important to further narrow down the essential functions of Net39. The HSA-CreERT2 transgene is expressed in all skeletal muscles, and we confirmed efficient deletion of Net39. Therefore, we speculate that certain myofibers may be more sensitive than others to the loss of Net39, but the nature of those myofibers still remains to be ascertained. Adult skeletal muscle undergoes basal levels of degeneration and regeneration to maintain tissue homeostasis[11]. Therefore, a small myofiber population experiences a

maturation process similar to the one observed at the juvenile stage, where loss of Net39 causes global abnormalities. Additional experiments are needed to determine if Net39 is required precisely at that stage and in that nuclear population.

Skeletal muscle is a syncytial tissue with hundreds of nuclei within a single myofiber. snRNA-seq now makes it now possible to readily interrogate changes in transcription and chromatin at single nuclear resolution. Recent studies examined changes in skeletal muscle at a single nucleus level during development, aging, and disease[54,65-67]. At the time of this thesis, there are no snRNA-seq datasets for EDMD available, and little is known about the contribution of specific myonuclear populations to the disorder. In Net39 cKO muscles, which display an EDMD-like phenotype, we observed heterogeneous changes across nuclei, primarily affecting type I myonuclei. However, the recently described and poorly understood remodeling/repair myonuclear population[65] is likely to play a significant role in pathological processes and requires further examination. Increasing our understanding of each myonuclear population, generating additional snRNA-seq datasets for other models for EDMD, and comparing them will be of great interest to define the underlying mechanisms of the disease.

The prior points highlight the diverse and intricate regulatory networks controlling skeletal muscle, and the difficulty to finely recapitulate these processes in cultured cells. In vitro, Net39 has been described as both a negative and a positive regulator of C2C12 myoblast differentiation by regulating mTOR signaling and gene positioning, respectively[17,18]. However, we did not observe changes in mTOR signaling in Net39 KO mice, or in C2C12 cells overexpressing

Net39 (data not shown). It is possible that the previously reported functions may be specific to transfected HeLa cells and not observed in muscle cells. In contrast, Net39 KO mice presented extensive changes in genome organization that compromised muscle function. These observations are more consistent with the other proposed function of Net39: to regulate myoblast differentiation by sequestering repressors of myogenesis to the nuclear periphery[44]. However, comparisons between in vivo and in vitro phenotypes indicate that, while roughly related, the pathways affected also differ between models.

Our unbiased identification of Net39 interactors by proximity labeling (BioID) showed different results from those reported previously. By myc-Net39 pulldown, the nucleoplasmic N-terminus of Net39 was previously shown to interact with mTOR[18], and that region has also been proposed to associate with Lamin A/C for genome tethering[17,44]. Our proximity labeling data showed association of Net39 with EDMD-related proteins but not mTOR or any lamins. One explanation for the differences is that Net39 may control genome organization by interacting with lamin-associated proteins rather than lamins themselves. It is also possible that the interaction with lamins may be transient or too weak to be detected by BioID. Alternatively, the N-terminus of Net39 may not be accessible to the biotin ligase fused to the C-terminus of Net39 used in this study. However, Net39 ChIP-seq strongly correlated with Lamin B1 DamID in C2C12 myotubes. Therefore, while Net39 and lamins may not be at immediate proximity, they are likely to functionally interact. We observed by proximity labeling and co-immunoprecipitation that Net39 interacts with Lemd2 and Emerin, two LEM proteins, and loss of Net39 results in upregulation of Lemd2 transcript and protein levels. LEM proteins tether chromatin and Lamin A/C to the nuclear

periphery through their nucleoplasmic LEM domain[32,68]. Nuclear envelope deformations like those observed in Net39 KO mice have also been reported in cardiomyopathy patients carrying a mutation in *LEMD2*[46]. We hypothesize that both proteins may potentially act as part of a complex with lamins to regulate nuclear organization and the mechanical properties of the envelope. In vitro, the N-terminus of Net39 mediates its known functions. It will be of interest to elucidate if that region, or others, control Net39 association with LEM proteins or other binding partners.

During changes in cell identity, some silenced regions of the genome are positioned in close proximity to the nuclear envelope[33]. From this observation, it has been proposed that lamins and nuclear envelope proteins may control gene expression by tethering specific genomic regions (LADs) to the periphery, to be repressed. However, further examination of that model by studying specific loci has yielded mixed results[69]. We identified Mef2c as a critical regulator of muscle gene expression that becomes activated upon loss of Net39, and we showed that Net39 can repress Mef2c activity. Mef2c is recruited to the nuclear pore complex during myoblast differentiation to promote gene expression[70], and we hypothesize that Net39 may tether Mef2c to the nuclear periphery to repress its activity at later stages. Similarly, the expression of MyoR, a myogenic repressor[57], is controlled by Net39, and likely accounts for the inhibition of myoblast differentiation observed when Net39 is knocked-down in vitro. We propose that the interplay between nuclear envelope proteins and certain transcription factors may provide an additional layer of specificity to changes in gene expression beyond regulation of LADs.

We showed that Net39 expression is diminished in EDMD patients with dominant LMNA missense mutations. Specifically, Net39 protein and transcript levels are decreased in muscle biopsies from EDMD patients relative to healthy controls, but not in a mouse model of muscular dystrophy (DMD) (data not shown). Mutations in LMNA have been proposed to impair MyoD activation in the context of EDMD[71], and Net39 is a MyoD target. Mutations in LMNA can also influence Net39 levels[60]. We surmise that LMNA-dependent MyoD dysregulation could underlie the loss of the muscle-specific nuclear envelope protein Net39 in EDMD. Reduced Net39 levels may contribute to the muscle defects observed in EDMD. It will be of interest to understand the role of Net39 in this disease, its therapeutic potential, and the transcriptional similarities and differences with other models for EDMD. Overall, our findings show that loss of the nuclear envelope protein Net39 causes profound defects in mice, and the reduced Net39 levels in EDMD patients potentially contribute to the pathogenesis of this disorder.

The role of nuclear envelope proteins in striated muscle has been predominantly explored in cardiac muscle, in contrast to skeletal muscle. Lamins and many components of the nuclear envelope are ubiquitous, and their deletion in mice can cause embryonic lethality[29,30,63]. In other cases, lamins and envelope proteins can exert partially redundant roles. For instance, loss of *Emd* in mice causes no overt phenotype[72], and instead acts as a modifier when other nuclear envelope proteins are lost. In contrast, *EMD* mutations are the main cause of X-linked EDMD in humans[36], indicating that the results in mice and other organisms cannot always be extrapolated to humans. Discovery of new nuclear envelope proteins such as Net39, either by proteomic analysis[42] or by identification of new pathogenic alleles by whole-exome sequencing[43] are ongoing areas of research.

Therefore, new deletions, conditional alleles, compound deletions, and humanized mouse models remain to be generated and characterized to understand the contribution of nuclear envelope genes to development and disease.

3. Klhl41 regulates sarcomere assembly

3.1. Kelch proteins in nemaline myopathy

Nemaline myopathy (NM) is one of the most severe forms of congenital myopathy, affecting ~1 in 50,000 births[73,74]. NM encompasses a set of genetically heterogeneous diseases defined by the presence of rod-like structures, called nemaline bodies, in skeletal muscle fibers. Nemaline bodies are formed by the abnormal aggregation of proteins within muscle thin filaments and are associated with myofibril disorganization, reduced contractile force, mitochondrial dysfunction, and a spectrum of abnormalities ranging from mild muscle weakness to complete akinesia. There is no effective treatment for NM and mechanistic insight into the molecular basis of the disorder is lacking.

To date, mutations in 11 different genes have been linked to NM, most of which encode components of the sarcomeric thin filament, including nebulin (NEB), actin-1, tropomyosins-2 and -3, troponin-1 and leiomodin-3 (LMOD3)[75-81]. Interestingly, 3 genes associated with NM, KLHL40, KLHL41 and KBTBD13, encode Kelch proteins, characterized by the presence of a Kelch-repeat domain, a BTB/POZ domain involved in protein-protein interaction, and a BACK domain that binds E3 ubiquitin ligases[82,83]. More than 60 different Kelch proteins have been identified[84], many of which function as substrate-specific adaptors for Cullin-3 (CUL3) E3 ubiquitin ligase, a component of the ubiquitin-proteasome system[85]. Modification of proteins by the covalent attachment of ubiquitin to lysine residues via CUL3 serves as a signal for protein degradation. However, there are also Kelch proteins that function independently of proteolysis[86] and much remains to be learned about their functions.

We and others showed that loss of function of the muscle-specific Kelch protein KLHL40 in mice causes NM similar to that seen in human patients with KLHL40 mutations[19,21]. Unlike other Kelch proteins that promote protein degradation, KLHL40 is required for stabilization of LMOD3, an actin nucleator, and NEB, a molecular ruler that controls myofibrillogenesis[19,76]. The absence of LMOD3 or NEB causes lethal NM and severe disruption of skeletal muscle sarcomeric structure and function in mice and humans, confirming the essential roles of these proteins in maintenance of sarcomere integrity. KLHL40 shares 52% identity with KLHL41, which is also expressed in a muscle-specific manner[87]. Similarly, KLHL41 mutations in humans have been associated with NM, and morpholino knockdown of KLHL41 in zebrafish causes NM-like abnormalities with aberrant myofibril formation[20]. In mice, Klhl41 is expressed in a muscle-specific manner with highest levels in adult skeletal muscle relative to the heart (**Fig. 15a, b**). During embryogenesis, Klhl41 is highly expressed in somite myotomes at embryonic day (E) 10.5 and in skeletal muscles throughout the body at later stages, as detected by in situ hybridization (**Fig. 15c**). However, the molecular functions of KLHL41 and the mechanistic basis of these abnormalities have not been determined.

Here, we describe a mouse model of severe NM caused by a loss of function mutation in the Klhl41 gene. Although KLHL40 and 41 share high homology and muscle-specific expression, we show that their mechanisms of action are distinct. KLHL41 preferentially stabilizes NEB rather than LMOD3, and this activity is dependent on K48-linked poly-ubiquitination sensed through the BTB domain of KLHL41. In the absence of KLHL41, NEB and other sarcomeric components fail to accumulate, resulting in early neonatal lethality. These

findings provide new insight into the molecular etiology of NM and also reveal a previously unrecognized role for Kelch proteins in protein stabilization and chaperone activity via poly-ubiquitination of partner proteins.

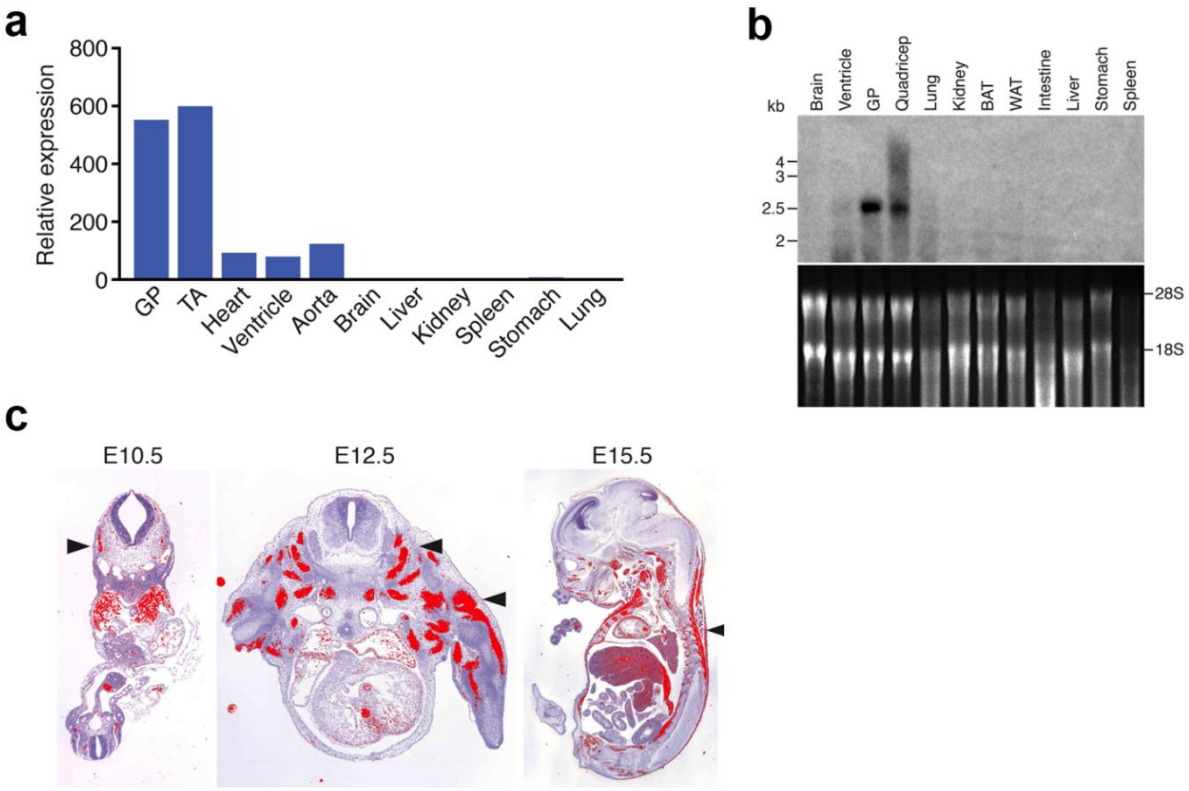

Fig. 15. Muscle-specific expression of *Klhl41*.

a. Distribution of Klhl41 transcript in adult mouse tissues as determined by qRT-PCR. Expression of Klhl41 transcript was normalized to 18 s rRNA. GP: Gastrocnemius plantaris, TA: Tibialis anterior. **b.** Northern blot analysis of *Klhl41* transcript in adult mouse tissues (top). Total RNA in each lane was visualized by ethidium bromide staining and 28 s and 18 s rRNAs were indicated on the right (bottom). BAT: Brown adipose tissue, WAT: White adipose tissue. **c.** Detection of Klhl41 transcript by in-situ hybridization using an Klhl41 anti-sense radioisotopic probe in mouse embryo sections at indicated ages. Transverse sections of E10.5 and E12.5 embryos, and sagittal section of an E15.5 embryo are shown. Signal for *Klhl41 mRNA* (pseudocolored red) only appears in developing muscle. Arrowheads point to representative developing skeletal muscle. The low signal outside the developing muscles represents background.

3.2. Deletion of Klhl41 causes nemaline myopathy in mice

Klhl41 knockout mice display neonatal lethality

To investigate the function of Klhl41 in mice, we obtained embryonic stem cells that contained a LacZ-Neo cassette in intron 1 of the Klhl41 locus from KOMP. In this allele, exon 1 of the Klhl41 gene is predicted to be spliced to LacZ, preventing expression of a functional Klhl41 transcript. Mice heterozygous for the mutant allele ($Klhl41^{+/-}$) were normal and were intercrossed to obtain $Klhl41^{-/-}$ knockout (KO) mice. LacZ expression was not detected in $Klhl41^{+/-}$ mice, suggesting that the LacZ cassette was spliced out. Quantitative RT-PCR (qRT-PCR) confirmed the complete loss of Klhl41 transcript in KO mice (**Fig. 16a**) and western blot analysis revealed loss of KLHL41 protein in muscle from KO mice (**Fig. 16b**). KO mice were born at Mendelian ratios from heterozygous intercrosses and were indistinguishable from WT littermates at birth (**Fig. 16c**). However, KO pups failed to thrive and showed progressive lethality from birth to postnatal day (P) 12, after which no surviving KO mice were observed (**Fig. 16d**). In order to ascertain that the failure to thrive was not due to difficulty in suckling or breathing, we confirmed that KO mice had milk spots comparable to those of their WT littermates. KO mice that survived the early neonatal period displayed severe runting at P3 and P10, and their body weight failed to increase with age (**Fig. 16e**), even when other littermates were removed from their mothers, indicating an intrinsic abnormality rather than simply an inability to compete with stronger siblings for nursing.

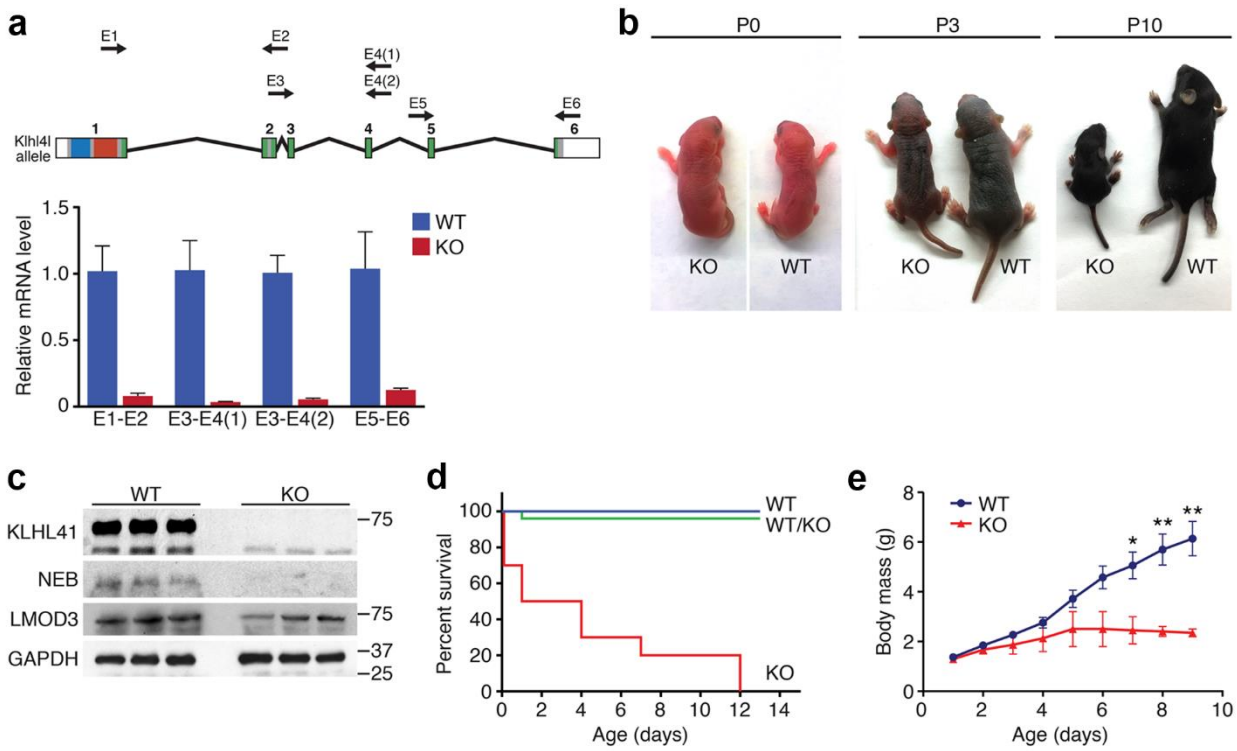

Fig. 16. Klhl41 KO mice display neonatal lethality.

a. *Klhl41* gene structure: the regions coding for BTB (blue), BACK (red) and Kelch repeats (green) are indicated (top). Detection of *Klhl41* transcript in P0 muscle of WT and *Klhl41* KO mice by qRT-PCR using the indicated primer pairs (arrows) (bottom) (n = 3 mice per genotype). Data are presented as mean ±SEM. **b.** Western blot analysis of the indicated proteins in WT and KO hindlimb muscles from P0 pups. Because of the large size of NEB (800 > KDa), the corresponding band is above the molecular weight markers used. GAPDH was used as a loading control. **c.** Surviving WT and *Klhl41* KO mice at P0, P3 and P10. KO pups show a failure-to-thrive phenotype and become severely runted by 10 days of age. **d.** Survival curve of offspring from *Klhl41* heterozygous intercrosses. n = 20 WT, n = 10 WT/KO (heterozygous), and n = 10 KO. **e.** Growth curves (body mass) of WT and *Klhl41* KO mice. n = 20 WT and n = 10 KO. Data are presented as mean ±SEM. *p<0.05. **p<0.01.

Loss of Klhl41 leads to nemaline myopathy and protein imbalance

Histological analysis of skeletal muscles of KO mice at various time points revealed occasional ragged fibers (fibers with discontinuities in their staining) in the diaphragm at P0 (**Fig. 17a**). Further abnormalities in muscle histology were observed by Gomori's trichrome staining (**Fig. 17b**). KO myofibers presented abundant depositions that were absent in WT muscle, and desmin staining showed additional cytoskeletal disarray (**Fig. 17c**). In WT muscle at P3, desmin was evenly expressed throughout transverse sections of myofibers. However, in KO mice, desmin protein aggregates were distributed across myofibers, indicating abnormal sarcomere structure. Electron microscopy of diaphragm (**Fig. 17d**) at P3 also showed sarcomere disarray and Z-line streaming, as well as electron dense inclusions, corresponding to nemaline bodies. Hearts from WT and KO mice were indistinguishable (data not shown).

To further define the muscle abnormalities of Klhl41 KO mice, we compared the protein compositions of WT and Klhl41 KO hindlimb muscle at P0 by unbiased quantitative proteomics (**Fig. 17e**). These studies revealed a total of 389 proteins that were up- or down-regulated in muscle from the KO mice. Remarkably, KLHL41 and NEB were the two most down-regulated proteins. Analysis of enriched biological pathways using the Database for Annotation, Visualization and Integrated Discovery (DAVID)[88] revealed that "sarcomere organization" and "regulation of muscle contraction" proteins were aberrantly down-regulated in KO mice (**Fig 17f)**. Many other down-regulated proteins in the KO mice were essential components of the sarcomere (**Fig. 17g**), including slow skeletal muscle troponin T, myosin light chain-3, myozenin-3, and β-tropomyosin (also associated with NM). As revealed by deep sequencing of RNA transcripts

the mRNAs encoding these proteins were unchanged in KO muscle (data not shown). Therefore, the changes in accumulation of these proteins likely reflect post-translational mechanisms. Notably, western blot analysis showed down-regulation of NEB and only a slight decrease in LMOD3 in Klhl41 KO mice[19] (**Fig. 17b**), while both NEB and LMOD3 were markedly down-regulated in Klhl40 KO mice. We therefore reasoned that KLHL41 could mainly stabilize NEB instead of LMOD3, further underscoring the likelihood that these two Kelch proteins act, at least partially, through different mechanisms. Nebulin-related anchoring protein (NRAP), another member of the nebulin family[89] was up-regulated both at protein and mRNA levels (probably as a compensatory consequence of sarcomere disarray), suggesting that the presence of Nebulin repeats is not sufficient for KLHL41 to recognize and stabilize its partners. In contrast to LMOD3, LMOD2, another member of the LMOD family involved in thin filament shortening and cardiomyopathy[90] was also up-regulated in Klhl41 KO mice both at protein and mRNA levels.

Among the pathways identified in the up-regulated proteins in KO mice (**Fig. 17g**) we found “ubiquitin-dependent catabolic processes”. Indeed, a remarkable number of up-regulated proteins in the KO mice were involved in ubiquitination, including E3 ubiquitin ligases HERC2, TRIM63 and TTC3. Among these, TRIM63/MuRF1 has been associated with atrophy and degradation of sarcomeric proteins[91]. Up-regulation of ubiquitination regulators occurred at both protein and mRNA levels, suggesting that accumulation of sarcomeric proteins within nemaline bodies might activate compensatory protein degradation pathways. Overall, these data indicate that loss of Klhl41 recapitulates severe

nemaline myopathy, including alterations in protein composition and appearance of nemaline bodies.

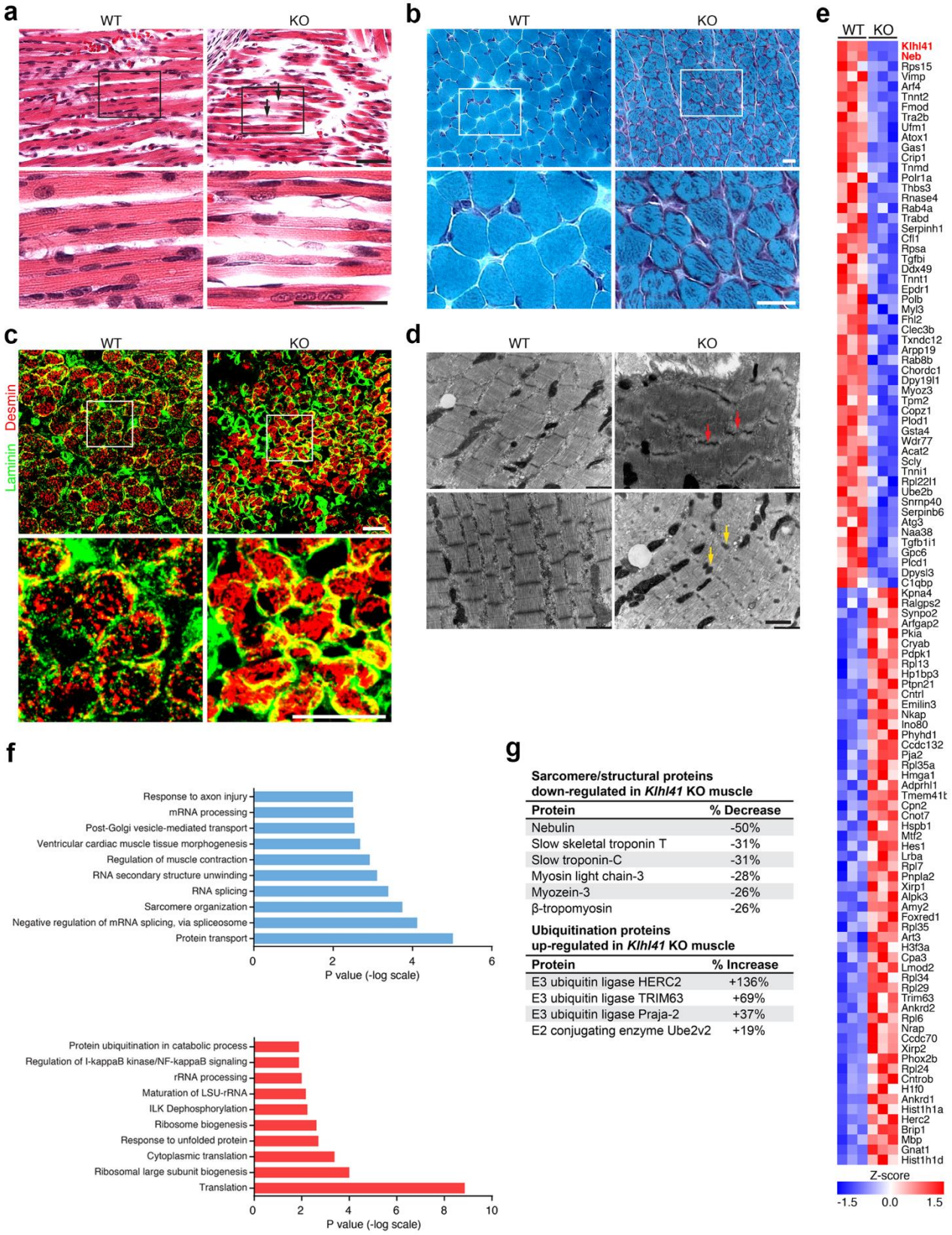

g

Sarcomere/structural proteins down-regulated in *Klhl41* KO muscle

Protein	% Decrease
Nebulin	-50%
Slow skeletal troponin T	-31%
Slow troponin-C	-31%
Myosin light chain-3	-28%
Myozein-3	-26%
β-tropomyosin	-26%

Ubiquitination proteins up-regulated in *Klhl41* KO muscle

Protein	% Increase
E3 ubiquitin ligase HERC2	+136%
E3 ubiquitin ligase TRIM63	+69%
E3 ubiquitin ligase Praja-2	+37%
E2 conjugating enzyme Ube2v2	+19%

Fig. 17. Loss of Klhl41 leads to nemaline myopathy and protein imbalance.

a. Hematoxylin and eosin staining of longitudinal sections of diaphragm muscle of WT and Klhl41 KO mice at P0. Arrows point to ragged fibers (fibers with discontinuous H&E staining) present in KO muscle but not WT muscle. Bottom panels are zoomed images of the indicated regions. Scale bar: 20 µm. **b.** Gomori's trichrome staining of transverse sections of quadriceps muscle of WT and Klhl41 KO mice at P10. KO myofibers show numerous abnormal depositions absent in WT muscle. Bottom panels are zoomed images of the indicated regions. Scale bar: 20 µm. **c.** Desmin and laminin immunostaining of transverse sections of WT and Klhl41 KO diaphragm at P3. Bottom panels are zoomed images of the indicated regions. Scale bar: 20 µm. **d.** Electron microscopy images of WT and Klhl41KO diaphragm at P3. Z-line streaming and nemaline bodies are indicated with red and yellow arrows, respectively. Scale bar: 1 µm. **e.** Heat map of changes in protein levels identified by proteomics in WT and Klhl41 KO hindlimb muscles at P0 (n = 3 mice per genotype). A total of 389 proteins were identified by proteomics to be differentially regulated ($p<0.05$). Proteins up or down-regulated by more than 30% compared to WT are represented (n = 111). KLHL41 and NEB (red) were the two most down-regulated proteins. Heat map was created with Morpheus and the color scale represents Z-score. **f.** Top 10 biological pathways enriched in down-regulated proteins (top) and up-regulated proteins (bottom) in Klhl41 KO hindlimb muscle at P0 as identified by DAVID analysis. **g.** Selected list of down-regulated sarcomeric proteins and up-regulated ubiquitination proteins identified by proteomics. Their relative levels to WT are shown on the right.

3.3. Poly-ubiquitination of Klhl41 is required for Nebulin stability

Klhl41 interacts with sarcomeric proteins and stabilizes Nebulin

To explore the molecular functions of KLHL41, we performed tandem affinity purification (TAP) of 3xFLAG-HA tagged KHL41 in C2C12 myotubes and identified KHL41 binding partners by mass spectrometry (**Fig. 18a**). Structural components of the sarcomere, such as NEB, NRAP and filamin-C (FLNC) were identified. Notably, mutations in NEB, NRAP, and FLNC have been associated with NM and other myopathies[92,93]. Because of the large size of NEB (>800KDa), which prohibits efficient expression of the full-length protein, we used a fragment of the NEB protein (NEBfrag) previously found to associate with KLHL40 in yeast two-hybrid assays[19]. We further validated the interaction between KLHL41 and both NEBfrag and FLNC by co-immunoprecipitation in COS-7 cells (**Fig. 18b**). LMOD3 was not detected by TAP using 3xFLAG-HA-KLHL41, nor did we detect an interaction between these proteins in co-immunoprecipitation experiments (data not shown). Kelch proteins are known to associate with each other and to form complexes with CUL3 to act as adaptors that confer substrate specificity to E3 ubiquitin ligase complexes[84]. Indeed, KLHL40 was also identified as a KLHL41 binding partner, suggesting a heterodimeric function of these proteins. We reasoned that the overlapping partners between KLHL41 and KLHL40 could reflect their association with a common complex. By co-immunoprecipitation assays, we found that KLHL41 self-associated and interacted with KLHL40 (**Fig. 18c**), as well as with CUL3 (**Fig. 18d**).

In contrast to other Kelch proteins, KLHL40 stabilizes its two main binding partners (NEB and LMOD3) instead of degrading them[19]. Due to the high similarity between KLHL40 and 41, we tested the stabilization of NEB and

LMOD3 by KLHL41 in transfected COS-7 cells (**Fig. 18e**). NEBfrag alone could not be detected by western blot, but NEBfrag protein levels were detectable when either KLHL40 or KLHL41 were co-expressed. In contrast, LMOD3 levels only increased modestly in the presence of KLHL41, whereas KLHL40 overexpression was sufficient to dramatically increase LMOD3 stability. We did not observe changes in either NRAP or FLNC protein levels when KLHL41 was co-expressed, indicating that the stabilizing activity of KLHL41 may be partner specific. Overall, these results suggest that KLHL41 interacts and stabilizes components of the sarcomere, and loss of these interactions leads to sarcomeric disarray and NM.

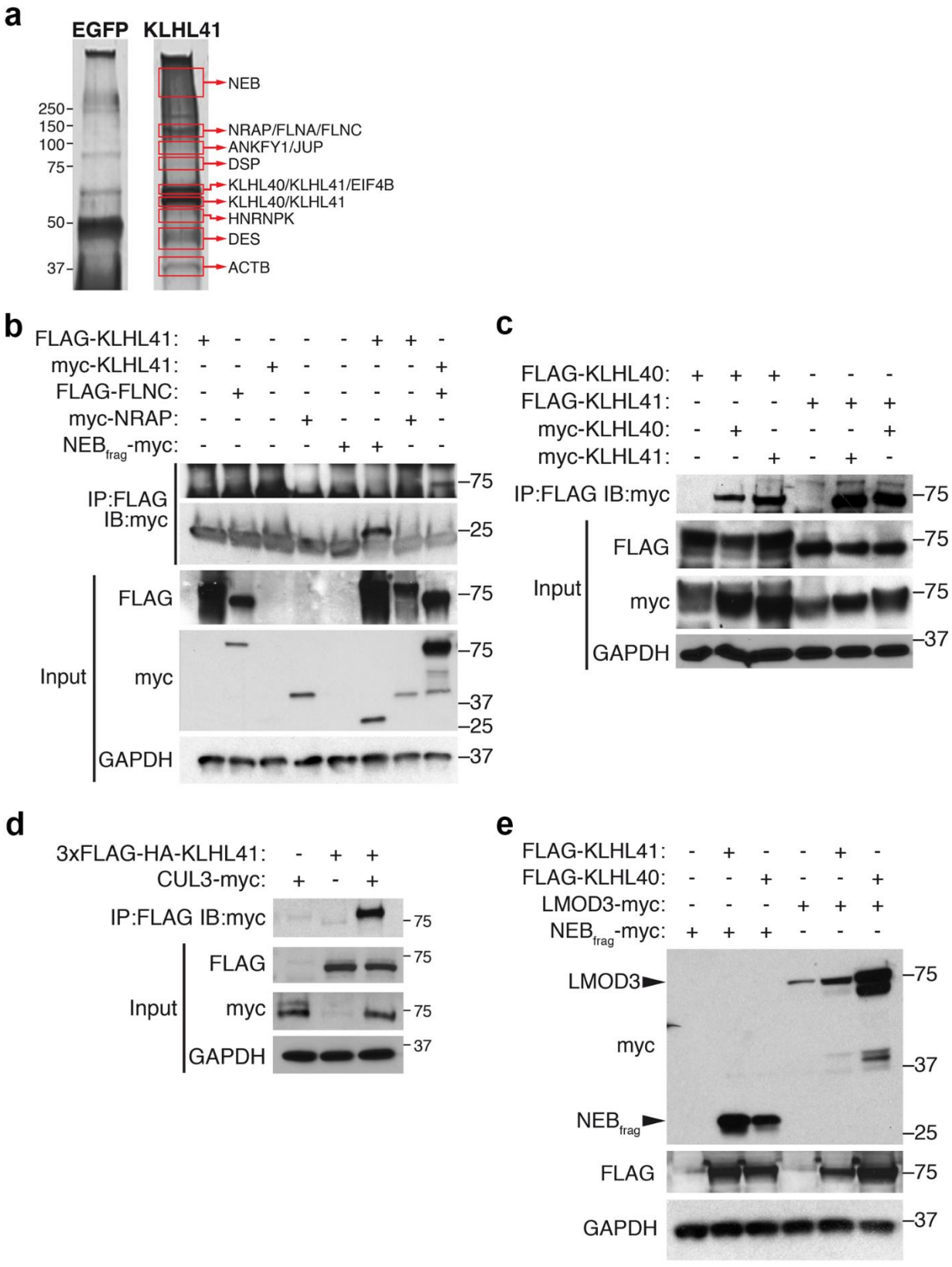

Fig. 18. Klhl41 interacts with sarcomeric proteins and stabilizes Nebulin.

a. Klhl41 binding partners identified following tandem affinity purification (TAP) from cultured C2C12 myotubes. Representative silver-stained gels with TAP

protein from myotubes infected with 3XFLAG-HA-EGFP (negative control) or 3xFLAG-HA-KLHL41 are shown. Proteins listed next to each box indicate the most abundant protein(s) identified in each corresponding area. **b.** Co-immunoprecipitation experiments to validate interactions between KLHL41 and FLNC, NRAP and NEBfrag. COS-7 cells were transfected with the indicated plasmids. **c.** Effect of KLHL41 on NEBfrag and LMOD3 stability. KLHL41 preferentially stabilizes NEBfrag. COS-7 cells were transfected with expression vectors for the indicated proteins. Protein levels of LMOD3, NEBfrag, KLHL40 and KLHL41 were detected by western blot. GAPDH was used as a loading control. **d.** Co-immunoprecipitation in transfected COS-7 cells indicates that KLHL41 homodimerizes with itself and heterodimerizes with klHL40. Western blots of co-immunoprecipitation and input with indicated antibodies are shown. GAPDH was used as a loading control. **e.** Interaction between 3XFLAG-HA-KLHL41 and CUL3-myc was detected by co-immunoprecipitation and western blot analysis with the indicated antibodies in transfected COS-7 cells.

Klhl41 stabilizing activity is regulated through K48-linked poly-ubiquitination of its BTB domain

KLHL41 contains three annotated domains (BTB, BACK and Kelch repeats). To define the regions required for its function, we created deletion mutants lacking each domain. By co-immunoprecipitation, we observed that deletion of the BTB domain was sufficient to abolish homodimerization of KLHL41 (**Fig. 19a**) and its association with CUL3 (**Fig. 19b**). Similarly, deletion of the BTB domain of KLHL40 greatly impaired its association with KLHL41 (**Fig. 19c**). Overall, these experiments indicate that the BTB domain of KLHL41 constitutes a critical region for interaction with other components of the CUL3 complex.

To assess whether poly-ubiquitination could regulate NEBfrag accumulation, we tested the effect of HA-tagged ubiquitin mutants on NEBfrag

protein levels. The formation of poly-ubiquitination chains typically occurs via the covalent attachment of the 76-amino acid ubiquitin peptide to lysine residues of proteins that are targeted for degradation[94]. The HA-tagged Ubiquitin-K0 (Ub-K0) mutant contains all its lysines mutated to arginines, thus preventing poly-ubiquitination in a dominant negative manner[95]. Overexpression of Ub-K0 did not rescue NEBfrag protein levels in the absence of KLHL41, but surprisingly was sufficient to prevent the accumulation of NEBfrag in the presence of KLHL41 (**Fig. 19d**). These findings suggest that poly-ubiquitination was unexpectedly required for the stabilization of NEBfrag by KLHL41. Next, we sought to identify the protein target of poly-ubiquitination. Co-immunoprecipitation experiments showed that KLHL41 was poly-ubiquitinated and overexpression of Ub-K0 greatly reduced KLHL41 poly-ubiquitination. Furthermore, deletion of the BTB domain was sufficient to strongly impair KLHL41 poly-ubiquitination (**Fig. 19e**).

Poly-ubiquitination can take place through any of the 7 lysine residues of ubiquitin or the free amino group from the first methionine. To understand which type of ubiquitination regulated KLHL41, we used HA-tagged ubiquitin mutants in which individual lysines were mutated to arginine (K6R, K11R, K27R, K29R, K33R, K48R and K63R). We found that overexpression of K48R was sufficient to prevent NEBfrag stabilization by KLHL41, whereas other mutants did not affect NEBfrag levels (**Fig. 19f**). Based on the preferential poly-ubiquitination of the BTB domain, we tested whether deletion of any functional domain of KLHL41 could rescue NEBfrag levels even in the presence of Ub-K0. As previously reported for KLHL40, deletion of the Kelch repeats of KLHL41 only decreased NEBfrag protein levels slightly when Ub-WT was overexpressed[19]. However, when poly-ubiquitination was inhibited by Ub-K0, ΔBTB-KLHL41 could still stabilize

NEBfrag.(**Fig. 19g**) While components of the E3 ligase complex are usually ubiquitinated[96,97], the requirement of the BTB domain for poly-ubiquitin sensitivity indicates that ubiquitination plays a direct role in the regulation of KLHL41 activity. Therefore, we conclude that K48-linked poly-ubiquitination of the KLHL41 BTB domain mediates NEBfrag stabilization.

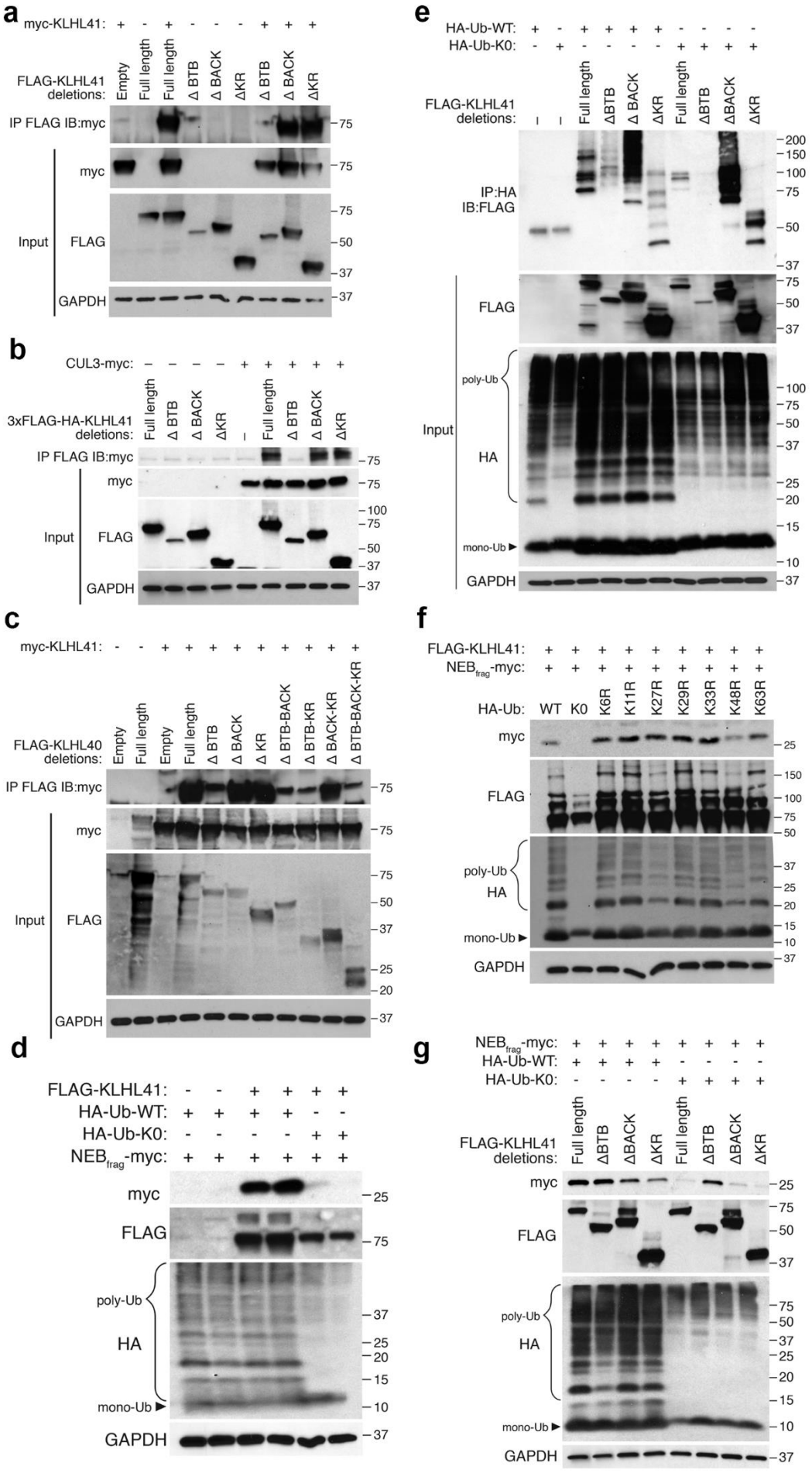
a
myc-KLHL41:
FLAG-KLHL41 deletions:
Empty
Full length
Full length
Δ BTB
Δ BACK
ΔKR
Δ BTB
Δ BACK
ΔKR
IP FLAG IB:myc
myc
Input
FLAG
GAPDH
b
CUL3-myc:
3xFLAG-HA-KLHL41 deletions:
c
myc-KLHL41:
FLAG-KLHL40 deletions:
Empty
Full length
Empty
Full length
Δ BTB
Δ BACK
Δ KR
Δ BTB-BACK
Δ BTB-KR
Δ BACK-KR
Δ BTB-BACK-KR
d
FLAG-KLHL41:
HA-Ub-WT:
HA-Ub-K0:
NEBfrag-myc:
poly-Ub
HA
mono-Ub
e
HA-Ub-WT:
HA-Ub-K0:
FLAG-KLHL41 deletions:
Full length
ΔBTB
Δ BACK
ΔKR
Full length
ΔBTB
ΔBACK
ΔKR
IP:HA IB:FLAG
FLAG
Input
poly-Ub
HA
mono-Ub
GAPDH
f
FLAG-KLHL41:
NEBfrag-myc:
HA-Ub:
WT
K0
K6R
K11R
K27R
K29R
K33R
K48R
K63R
myc
FLAG
poly-Ub
HA
mono-Ub
GAPDH
g
NEBfrag-myc:
HA-Ub-WT:
HA-Ub-K0:
FLAG-KLHL41 deletions:
Full length
ΔBTB
ΔBACK
ΔKR
Full length
ΔBTB
ΔBACK
ΔKR
myc
FLAG
poly-Ub
HA
mono-Ub
GAPDH

Fig. 19. Klhl41 stabilizing activity is regulated through K48-linked poly-ubiquitination of its BTB domain.

a. Co-immunoprecipitation of various FLAG-tagged KLHL41 deletion mutants with full-length KLHL41 (myc-KLHL41) in transfected COS-7 cells to identify the domains necessary for KLHL41 self-dimerization. **b.** Co-immunoprecipitation of various FLAG-tagged KLHL41 deletion mutants with CUL3-myc in transfected COS-7 cells to identify the domains necessary for association with CUL3. **c.** Co-immunoprecipitation of various FLAG-tagged KLHL40 deletion mutants with full-length KLHL41 (myc-KLHL41) in transfected COS-7 cells to identify the domains of KLHL40 required for heterodimerization with KLHL41. **d.** KLHL41 can stabilize NEB_{frag} in the presence of HA-Ub-WT but not HA-Ub-K0 mutant. Expression of NEB_{frag} and KLHL41 was determined by western blot analysis with the indicated antibodies in COS-7 cells. The laddered smear detected in HA input with HA-Ub-WT corresponds to the pool of poly-ubiquitinated proteins (indicated as poly-Ub). In contrast, HA-Ub-K0 (lysine zero), a mutant protein that cannot be poly-ubiquitinated, was preferentially detected as a single band of mono-Ubiquitin (indicated as mono-Ub). **e.** KLHL41 is preferentially poly-ubiquitinated in the BTB domain. Full-length and deletion mutants of KLHL41 were co-expressed in the presence of HA-Ub-WT or HA-Ub-K0 in COS-7 cells. Protein expression was detected by western blot analysis using the indicated antibodies. Note that either deletion of BTB (ΔBTB) or HA-Ub-K0 overexpression collapsed poly-ubiquitinated bands. **f.** HA-Ub-K48R impairs KLHL41 activity to stabilize NEB_{frag}. KLHL41 stabilization of NEB_{frag} in the presence of Ubiquitin HA-Ub-WT, K0 and Ub lysine mutants were determined by western blot analysis. HA-Ub-K48R overexpression led to a decrease in poly-ubiquitinated KLHL41, as observed in the FLAG input western blot. Each Ub lysine mutant only inhibits one type of ubiquitination. Therefore, total poly-ubiquitination levels remain the same as HA-Ub-WT as detected in HA input western blot. **g.** Deletion of the KLHL41 BTB domain (ΔBTB) can restore NEB_{frag} stability in the presence of Ub-K0 mutant. Western blot analysis shows NEB_{frag} stability in the presence of full length and deletion mutants of KLHL41 when co-expressed with either HA-Ub-WT or HA-Ub-K0 mutant in COS-7 cells.

KLHL41 prevents aggregation of NEBfrag

Because mutations in NEB are the most common cause of NM[73], we investigated the mechanism by which KLHL41 stabilizes NEB. We hypothesized that KLHL41 could either prevent degradation of NEB by another E3 ligase or act as a chaperone. Inhibition of proteasomal activity or autophagy by MG132 or chloroquine, respectively, was not sufficient to rescue NEBfrag protein levels in the absence of KLHL41 (**Fig. 20a, b**), suggesting that KLHL41 did not evoke its stabilizing effect on NEBfrag by degrading another E3 ligase. Next, we sought to identify a potential degron in NEBfrag that could target it for degradation. We therefore generated a series of NEBfrag mutants each containing a 25-residue deletion spanning the entire protein and assessed their protein levels by western blot in the presence or absence of KLHL41. Strikingly, we observed that, in contrast to full length NEBfrag, most deletion mutants could be detected even in the absence of KLHL41, albeit at lower levels (**Fig. 20c**). Furthermore, all mutants exhibited increased protein levels in the presence of KLHL41, and they interacted with KLHL41 by co-immunoprecipitation (d5 and d6 had weaker interactions than others) (**Fig. 20c**). These findings indicate that NEBfrag is unlikely to be regulated by a degron recognized by an unknown E3 ligase but rather general conformational changes promote NEBfrag stability.

To assess whether KLHL41 prevented NEBfrag aggregation, we performed protein extraction of the insoluble fraction of transfected COS-7 cells with high detergent concentration. We found that when NEBfrag was expressed alone, it could be detected in the insoluble fraction, whereas co-expression of KLHL41 was sufficient to shift a portion of the NEBfrag pool to the soluble fraction (**Fig. 20d**). We further validated these results by immunofluorescence (**Fig. 20e**).

NEBfrag alone formed aggregates localized predominantly in the nucleus, and co-expression of KLHL41 or KLHL40 resulted in homogenous cytosolic staining. Thus, these results suggest that KLHL41 and KLHL40 can act as chaperones and prevent NEBfrag aggregation.

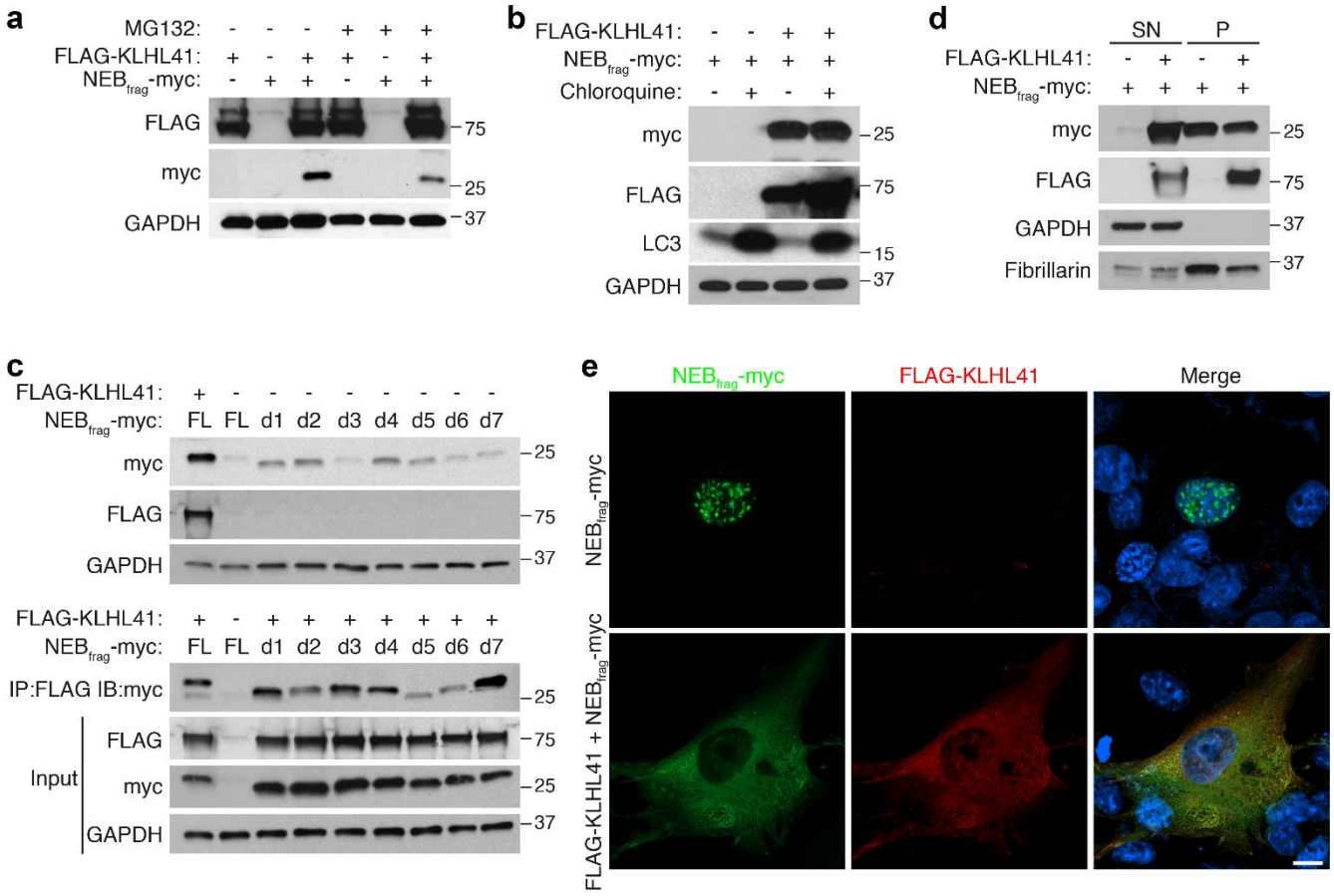

Fig. 20. Klhl41 prevents aggregation of NEBfrag.

a. KLHL41 regulation of NEBfrag in the absence or presence of proteasome inhibitor was determined by western blot analysis with the indicated antibodies in COS-7 cells. **b.** KLHL41 regulation of NEBfrag in the absence or presence of autophagy inhibitor in COS-7 cells. Increased level of LC3 protein was detected as a positive control for autophagy inhibition. **c.** Multiple NEBfrag deletion mutants are stable in the absence of KLHL41. COS-7 cells were transfected with various NEBfrag deletion mutants in the absence (top) or presence (bottom) of KLHL41. Protein levels were determined by western blot analysis with the indicated antibodies. Co-immunoprecipitation of FLAG-KLHL41

and NEBfrag deletion mutants (bottom) shows that all mutants interact with KLHL41. **d.** Expression of KLHL41 affects NEB_{frag} solubility. COS-7 cells were transfected with the indicated plasmids and lysed with mild detergent to collect supernatant (SN). The remaining pellet (P) was then solubilized under high detergent conditions. Expression of FLAG-KLHL41 and NEBfrag in SN and P fractions was detected by western blot analysis. GAPDH was restricted to the SN fraction. Fibrillarin, a nucleolar protein, was enriched in P. **e.** Expression of NEBfrag in the absence and presence of KLHL41 was detected by immunofluorescence of COS-7 cells transfected with the indicated plasmids. Scale bar: 10 µm.

3.4. Discussion and future directions

Mutations in KLHL41 have been associated with NM in humans, but molecular understanding of the mechanism of action of KLHL41 has been lacking, despite its clinical significance. Furthermore, the unique stabilizing activity of both KLHL41 and KLHL40, which distinguishes them from most other members of the Kelch family, has not been previously explored. Our results demonstrate that KLHL41 is required for sarcomere integrity and stabilization of essential muscle structural proteins. The absence of KLHL41 in mice results in severe NM with general sarcomere disarray, accumulation of nemaline bodies and perinatal death as seen in humans with KLHL41 mutations. Our results reveal a unique pro-stabilizing function of KLHL41 in which it prevents NEB aggregation through poly-ubiquitination of its BTB domain. We surmise that under normal conditions KLHL41 functions as a chaperone, preventing NEB aggregation and degradation. Loss of KLHL41 or reduced poly-ubiquitination of KLHL41 results in loss of KLHL41 activity, NEB aggregation and NM. These regulatory events suggest that KLHL41 may serve as a poly-ubiquitination sensor, offering a new layer of complexity to the abundant ubiquitin ligases and deubiquitinases resident in muscle sarcomeres.

Protein ubiquitination involves the covalent attachment of the 76-amino acid ubiquitin peptide to the epsilon amino group of target lysine residues. Poly-ubiquitin chains can be formed by sequential addition of ubiquitin molecules through any of its 7 lysines (K6, K11, K27, K29, K33, K48 and K63) or the free amino group of the initial methionine[98]. K48-linked poly-ubiquitination has been extensively characterized as the canonical signal for proteasomal degradation and most Kelch proteins for which functions have been explored have been

shown to mediate protein degradation via E3 ligase-dependent poly-ubiquitination[99-102]. However, new nonproteolytic roles for Kelch proteins are being reported. For example, KLHL20 controls trafficking of the actin stabilizing protein Coronin 7 via K33-linked poly-ubiquitination[103], while mono-ubiquitination NOLC1 and TCOLF by KBTBD8 regulates translation and cell fate specification[86]. Our findings highlight a unique protein stabilizing function of KLHL41. In contrast to other Kelch proteins, KLHL41 stabilizes its partner, NEB, instead of marking it for degradation. Inhibition of the two major degradation pathways (the ubiquitin-proteasome and the lysosome) was not sufficient to rescue NEBfrag levels in the absence of KLHL41 indicating that KLHL41 is not regulating another E3 ligase responsible for NEB degradation. Intriguingly, inhibition of poly-ubiquitination abolished the ability of KLHL41 to stabilize NEBfrag. Additionally, we could not identify a degron responsible for NEBfrag instability in the absence of KLHL41 but rather, multiple mutants were stable when short sequences of the protein were deleted. These results suggest that KLHL41 stabilizes NEBfrag by regulating its folding rather than by degrading an unknown protein that might decrease NEBfrag levels. Specific inhibition of K48-linked poly-ubiquitination recapitulated the loss of NEBfrag observed with Ub-K0. Besides its canonical role in degradation, K48-linked poly-ubiquitination has been implicated in substrate stabilization[104] and segregation of ubiquitinated proteins from their partners[105,106]. In contrast to those studies, however, KLHL41 itself is ubiquitinated instead of its partner. Components of the E3 ubiquitin ligase complex can be self-ubiquitinated during the transfer of ubiquitin to their substrates or as a negative feedback loop to downregulate their protein levels[96,97], but the requirement of Kelch protein poly-ubiquitination for protein stabilization constitutes a novel regulatory mechanism.

We speculate that K48-linked poly-ubiquitination of KLHL41 could regulate protein-protein interactions between the BTB domain and other partners. K48-linked poly-ubiquitination can act as a recognition signal for CDC48, a chaperone required to extract misfolded proteins from the ER during ER-associated protein degradation[107]. Additional work will be required to understand how KLHL41 is regulated in a poly-ubiquitin dependent manner.

Although KLHL40 and 41 share extensive homology and loss of either gene causes NM, our results indicate that these two proteins possess both overlapping and distinct functions. Loss of either KLHL40 or KLHL41 leads to severe NM in humans, whereas Klhl41 KO mice present earlier muscle dysfunction than Klhl40 KO mice. While both proteins stabilize NEB, only KLHL40 stabilizes LMOD3 significantly. Considering that the loss of function phenotype of KLHL41 is stronger than that of KLHL40, it is likely KLHL41 is more critical for sarcomere integrity by interacting with additional partners. The stabilization of LMOD3 by KLHL40 occurs through a mechanism distinct from the stabilization of NEB, as inhibition of poly-ubiquitination does not decrease LMOD3 protein levels in the presence of KLHL40[19]. Furthermore, in the absence of KLHL40, LMOD3 levels are increased by proteasome inhibition. KLHL40 and KLHL41 are highly similar in their BTB and BACK domains, which could explain why both are sensitive to poly-ubiquitination. However, they present differences within the Kelch repeats, which likely enables them to discriminate between different substrates. It is currently unknown whether other Kelch proteins, especially those closely related to KLHL41, act as chaperones or can stabilize their partners in a poly-ubiquitin dependent manner. Of special interest is KBTBD13, the only other

Kelch protein associated with NM. Further work is needed to understand if KBTBD13 acts through a similar mechanism to that of KLHL40 and KLHL41.

NM and other protein aggregomyopathies are characterized by formation of pathogenic protein inclusions[108]. Although the most common causes for protein aggregation in myofibers are mutations in sarcomeric genes, mutations in the MuRF1 and MuRF3 E3 ubiquitin ligases have also been reported[109]. Nemaline bodies can be detected in the cytoplasm and the nucleus of patient biopsies, and the presence of intranuclear rods has been associated with more severe clinical phenotypes[110]. Chaperones have become interesting therapeutic targets in protein aggregation diseases[111,112]. Indeed, during myofibrillogenesis, chaperones are required for proper assembly of the sarcomere and loss of their activity has been associated with a broad array of muscle disorders[113,114]. Our results reveal an unexpected chaperone activity for KLHL40 and 41, suggesting that modulation of chaperone activity could represent an approach to treat NM. There are currently no effective therapies for NM. Thus, elucidation of the precise mechanisms of action of KLHL40 and 41 may ultimately allow new interventions into the pathogenic processes associated with this disorder.

4. Loss of Mymx ectodomain causes CFZS

4.1. Mymx and Myomaker are the master regulators of myoblast fusion

Cell-cell fusion is an essential event for developmental milestones such as fertilization and placentation, and in specialized cell types like osteoclasts and muscle fibers[115]. These processes require the merging of two or more cells to form a diploid cell or a specialized multinucleated syncytium. Cell fusion is highly coordinated and requires fusing cells to recognize and approach each other, extend actin protrusions, and recruit protein fusogens at the sites of fusion[116]. Fusogens bring the opposing membranes in close proximity and expel the water between them, thus creating an energetically favorable environment for the merging of both membranes (hemifusion) and the rapid opening of a fusion pore to mix cytosolic contents. Skeletal muscle undergoes extensive fusion and each myofiber contains hundreds of nuclei[117]. The master regulators of myoblast fusion are Myomaker[118] (Mymk, also known as Tmem8c) and Myomixer[119-121] (Mymx, also known as Myomerger, Minion, or Gm7325). To avoid confusion, they will be referred as Myomaker and Mymx, respectively. Since their discovery, mechanistic studies on Myomaker and Mymx have been undertaken[122,123], but additional work is required to further understand how muscle fusogens control myoblast fusion in development and disease.

Protein fusogens are typically characterized by long ectodomains capable of oligomerizing and reaching the opposing membrane upon conformational changes[124,125]. However, Myomaker and Mymx are plasma membrane fusogens with distinct protein sequences and topologies. Myomaker is a seven-transmembrane protein (**Fig. 21a**)[126], and Mymx is a small single-pass plasma

membrane protein (micropeptide/microprotein) as short as 62 amino acids in some species[127] (**Fig. 21b**). When co-expressed in vitro, Myomaker and Mymx are sufficient to confer fusogenicity to cells that normally do not fuse, such as fibroblasts (**Fig. 21c**). Since then, mutagenesis and evolutionary studies have been performed to elucidate the functional and essential conserved regions of each protein. In the case of Myomaker, palmitoylation of its C-terminal cysteines has been shown to be required for fusion[128], even if some species encode for much longer orthologs with expanded C-termini[129]. In contrast, Mymx is less conserved at the amino acid level, but all orthologs encode for a hydrophobic N-terminal trasmembrane domain, a basic-hydrophobic 15 amino acid segment, and a hydrophobic region with an essential AxLyCxL motif. Higher vertebrate orthologues include an extended C-terminus (19 additional amino acids) that is not required for Mymx activity in vitro[127]. Mechanistically, Myomaker has been proposed to act as a plasma membrane destabilizer to promote membrane hemifusion. Topological and sequence analysis of Myomaker suggests it may be similar to GPCRs and ceramidase enzymes[130], but its precise molecular function remains elusive. More recently, Mymx activity was reported to be replaceable by osmotic shock in vitro[123], thus suggesting that Mymx may physically disrupt membranes or membrane curvature to drive fusion pore formation.

Mymx and Myomaker are necessary for vertebrate muscle fusion in vivo, and knock-out mice for either of the two genes die at birth due to lack of functional, multinucleated myofibers[118,119] (**Fig. 21d**). Myoblast fusion is required for muscle development and maintenance. In adult vertebrates, satellite cells (which comprise the primary muscle precursor population) may become activated and initiate fusion to be incorporated into preexisting myofibers or to form new ones.

Adult deletion of Myomaker or Mymx in satellite cells prevents muscle regeneration in response to injury[131,132]. Human mutations in *MYOMAKER* are the cause of the genetic disorder known as Carey-Fineman-Ziter syndrome (CFZS), a congenital myopathy[133]. CFZS patients carry hypomorphic *MYOMAKER* allelic combinations that result in impaired myoblast fusion (**Fig. 21a, e**). Because of the reduced muscle multinucleation, CFZS manifests as an array of abnormalities, including hypotonia, myofiber size dysregulation, Moebius sequence, Pierre Robin complex, and growth defects (**Fig. 21f-h**). *MYOMAKER* and *MYMX* are essential muscle fusion proteins, but deleterious mutations have been identified only in *MYOMAKER* so far.

Here, we report that in humans, loss of the Mymx ectodomain causes a myopathic, CFZS-like phenotype. Disease models (iPSC-derived skeletal muscle and a humanized mouse model) are currently being generated to reveal the contribution of the Mymx ectodomain to myoblast fusion. Mechanistically, loss of the Mymx ectodomain generates a stable protein truncation with impaired activity in vitro, and nuclear magnetic resonance (NMR) studies reveal that purified Mymx ectodomain undergoes conformational changes in the presence of micelles. We propose that the Mymx ectodomain drives pore formation by changing its conformation inside-out through interactions with the hydrophobic environment of opposing membranes during fusion. Mymx is one of the smallest fusogens in biology, and our findings reveal its contribution to human disease and the underlying molecular mechanism.

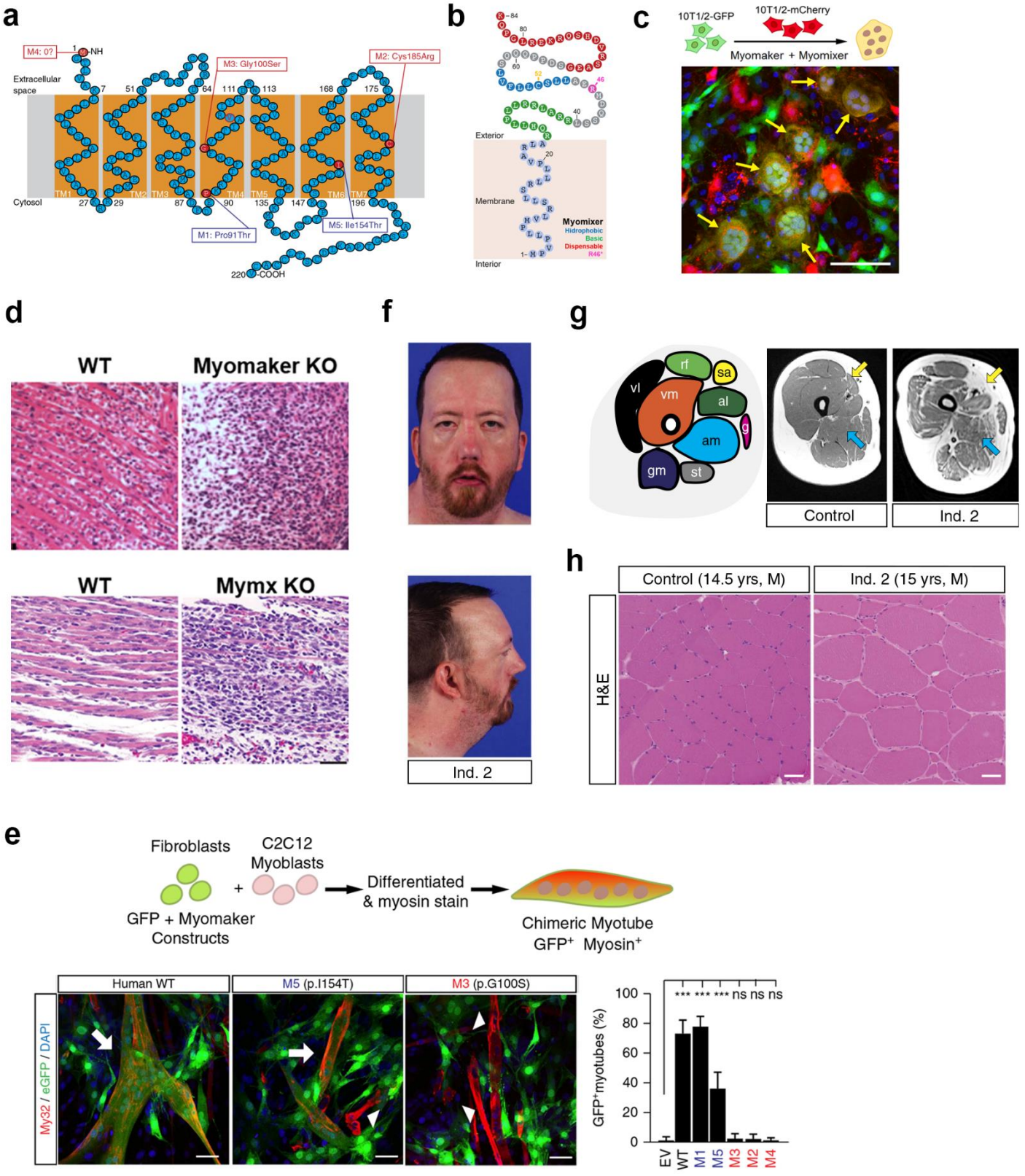
a
M4: 0?
NH
Extracellular space
M3: Gly100Ser
M2: Cys185Arg
M1: Pro91Thr
M5: Ile154Thr
Cytosol
COOH
TM1
TM2
TM3
TM4
TM5
TM6
TM7
b
Exterior
Membrane
Interior
Myomixer
Hidrophobic
Basic
Dispensable
c
10T1/2-GFP
10T1/2-mCherry
Myomaker + Myomixer
d
WT
Myomaker KO
WT
Mymx KO
f
Ind. 2
g
rf
sa
vl
vm
al
am
gm
st
Control
Ind. 2
h
Control (14.5 yrs, M)
Ind. 2 (15 yrs, M)
H&E
e
Fibroblasts
C2C12 Myoblasts
GFP + Myomaker Constructs
Differentiated & myosin stain
Chimeric Myotube GFP+ Myosin+
Human WT
M5 (p.I154T)
M3 (p.G100S)
My32 / eGFP / DAPI
GFP+myotubes (%)
*** *** *** ns ns ns
EV
WT
M1
M5
M3
M2
M4

Fig. 21. Myomaker and Mymx regulate myoblast fusion.

a. Predicted topology of human MYOMAKER protein. The red amino acids indicate residues mutated in CFZS patients. Mutations (M) 1 and M5, in blue, are less severe than M2, M3 and M4, in red. **b.** Predicted topology of MYMX protein. The colored residues denote hydrophobic (blue), basic-hydrophobic (green) and disordered hydrophilic (red) regions. R46 (pink) is a residue mutated in CFZS-like patients. **c.** In vitro fusion assays show that Myomaker and Mymx are sufficient to induce fusion in vitro. 10T1/2 fibroblasts labeled with GFP or mCherry and expressing Myomaker and Mymx were co-cultured and imaged (up). Immunofluorescence images showing fibroblast-fibroblast fusion upon ectopic overexpression of Myomaker and Mymx (down). **d.** Deletion of Myomaker or Mymx abolishes myoblast fusion. Longitudinal sections of perinatal muscles from WT and Myomaker KO (upper panels) and WT and Mymx KO (lower panels) reveal loss of multinucleated fibers. **e.** Photograph of a CFZS patient with facial dysmorphism. **f.** Representation of human thigh muscles: vastus lateralis (vl), black; vastus medialis (vm), orange; rectus femoris (rf), light green; sartorius (sa), yellow; adductor longus (al), dark green; adductor magnus (am), light blue; gracilis (g), pink; semitendinosus (st), grey; gluteus maximus (gm), purple. (Left). Left thigh MRI of control and CFZS patients. Arrows denote muscle atrophy and fatty infiltration. **g.** Hematoxylin and eosin staining of transverse sections of vastus lateralis biopsies from a healthy control and a CFZS patient. Variable fiber size can be observed in the CFZS patient. Scale bar: 50µm. **h.** Scheme for heterologous fusion assays. Fibroblasts expressing GFP and different Myomaker constructs were mixed with C2C12 immortalized myoblasts. The presence of chimeric myotubes was assessed after My32 staining (upper panel). Fusion assays and quantification for selected Myomaker constructs (lower panel). scale bar: 50µm. Panels were reproduced from the indicated references[118,119,133].

4.2. A novel mutation in Mymx causes CFZS

Identification of a *MYMX* mutation in myopathic patients

Two patients presenting a phenotype highly reminiscent of CFZS[133] were identified (Dr. Van Jaarsveld, personal communication). The patients were two siblings (15 and 13 years old) with overlapping myopathic features, including slowly progressive muscle weakness, scoliosis, and dysmorphic facial features. The parents were asymptomatic. Whole-exome sequencing of the family did not identify any known pathogenic mutation in myopathy-related genes, including *MYOMAKER,* but revealed that the parents were distantly related. Additional analysis of novel gene variants identified a single nucleotide polymorphism (SNP) in *MYMX* (c.136C>T, p.R46Stop) (**Fig. 22a**). Both siblings were homozygous for the SNP, whereas the parents were heterozygous carriers (**Fig. 22b**). The SNP (referred hereafter as Mymx^{R46*}) causes the appearance of a premature stop codon resulting in loss of most of the extracellular region of Mymx (ectodomain) (**Fig. 22c**). From prior studies, this mutation is predicted to be highly pathogenic. These preliminary findings suggest that compromised Mymx activity, similar to Myomaker, could potentially cause CFZS, and additional analyses are currently being performed to characterize myopathic features in these patients.

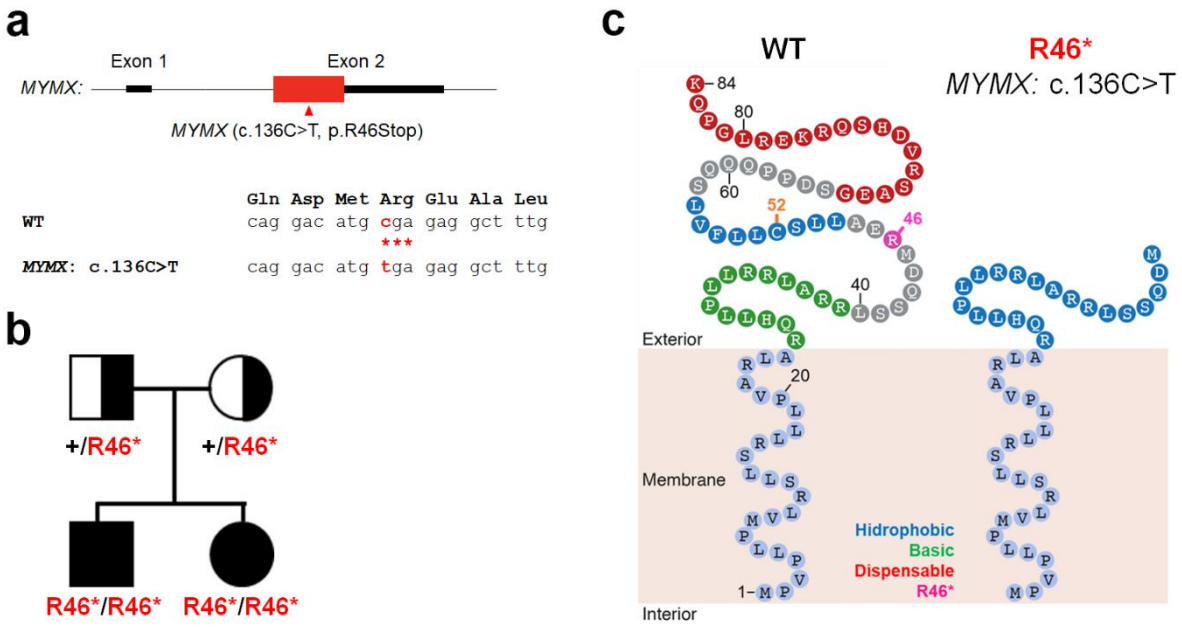

Fig. 22. Identification of a *MYMX* mutation in myopathic patients.

a. Gene structure of human *MYMX*. Boxes represent exons. Black boxes denote untranslated regions and red boxes indicate open reading frame. Arrowhead indicates the location of the SNP (R46*) observed in myopathic patients (upper panel). Genomic sequence surrounding *MYMX* SNP (lower panel). **b.** Pedigree of the family with *MYMX*^{R46*} allele. Square indicates male, circle indicates female. Half black filling indicates heterozygosity, and full black filling indicates homozygosity for Mymx^{R46*}. **c.** Predicted protein products from WT and Mymx^{R46*} alleles.

Generation of in vitro and in vivo CFZS disease models

To assess the contribution of the Mymx ectodomain to muscle fusion, induced pluripotent stem cells (iPSCs) were generated from gingival fibroblasts from one CFZS patient by delivery of the Yamanaka factors with Sendai virus (**Fig. 23a**). Mymx^{R46*} (c.136C>T) is amenable to correction by CRISPR-Cas-mediated Adenine Base Editors (ABE). Therefore, to allow for isogenic comparisons, patient-derived iPSCs will have their *MYMX* locus restored back to

wild-type by base-editing, and several sgRNAs have been designed for that purpose. As an additional control, patient-derived iPSCs will be infected with adeno-associated virus (AAV) encoding wild-type *MYMX* under control of a chimeric murine Mef2c-Myogenin promoter[55] (expressed during myoblast differentiation) and a ubiquitously expressed NLS-GFP fluorescent reporter (CMV-NLS-GFP-Myo-Mymx) (**Fig. 23b**). Importantly, AAV-CMV-NLS-GFP-Myo-Mymx may also be used in future studies in mouse models where myoblast fusion is impaired. Once WT and Mymx^{R46*} isogenic iPSCs cell lines are generated, they will be differentiated into skeletal muscle, and fusion efficiency will be measured.

To understand the function of the Mymx ectodomain in vivo, a humanized mouse model harboring the Mymx^{R46*} allele was generated by CRISPR/Cas9-mediated genome editing. Cas9 and a single-stranded oligo donor (ssODN) were initially used to introduce the SNP in mice, but homologous recombination was not observed after multiple injections (data not shown). To reduce unspecific non-homologous DNA end joining, Cas9 nickase D10A was used for injection (**Fig. 23c**), and 3 out of 63 mice were positive for the Mymx^{R46*}. These mice were bred to WT for germline transmission and heterozygous *Mymx*$^{+/R46*}$ mice were obtained and genotyped by Sanger sequencing (**Fig. 23d**). Overall, we generated the required reagents to analyze Mymx^{R46*} both in vitro and in vivo, and studies are underway to assess the contribution of the Mymx ectodomain to myoblast fusion in mice.

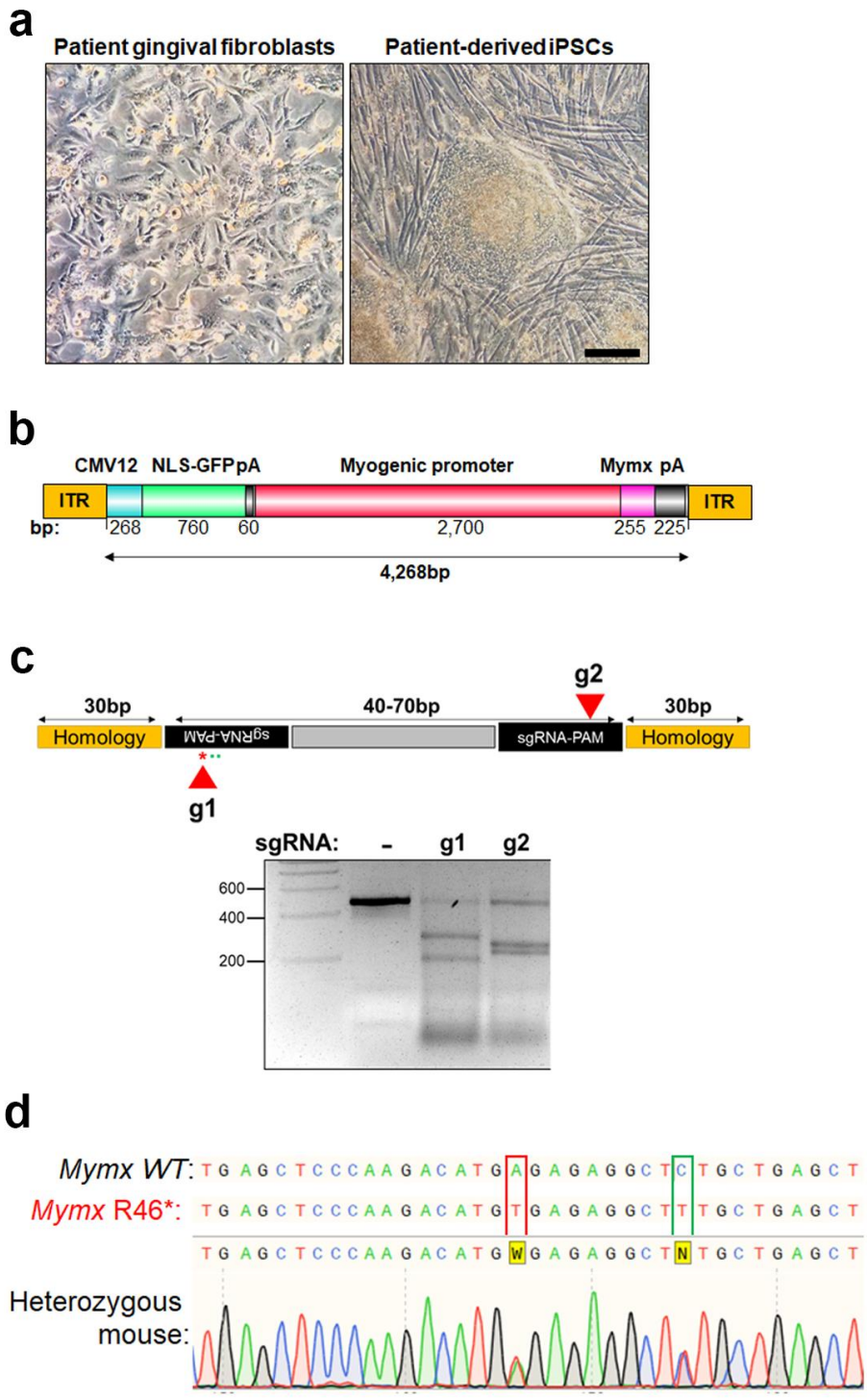

Fig. 23. Generation of in vitro and in vivo CFZS disease models.

a. Generation of induced pluripotent stem cells from patient fibroblasts. Microscopy images of fibroblasts before and after reprogramming into iPSCs by delivery of Sendai virus. Scale bar: 100 µm. **b.** Design of the AAV vector to deliver Mymx into patient-derived iPSCs. CMV12 is a minimal ubiquitous promoter

derived from cytomegalovirus. NLS: Nuclear localization signal. The myogenic promoter (Myo) is a fusion of a Mef2c enhancer (1.1Kb) and the Myogenin promoter (1.6Kb). The first polyA is synthetic, whereas the second polyA is derived from bovine growth hormone polyA. ITR: Inverted terminal repeat. The total packaging capacity of AAV is 4.4Kb. **c.** Cas9 nickase strategy to generate Mymx^{R46*} humanized mice. Cas9 nickase-mediated knock-in requires the use of two sgRNAs with PAMs opposing each other and separated by 40 to 70bp. The single stranded DNA donor for homology-mediated repair must contain 30 nucleotides of homology on each end, as well as the desired mutation (red) and an additional silent mutation (green) that humanizes the locus at the nucleotide level and prevents recutting after recombination (upper panel). In vitro cleavage assay with recombinant Cas9 (WT) showing that Cas9 and the selected sgRNAs can engage and cut the desired genomic sequence for Mymx knock-in (lower panel). **d.** Sanger sequencing of the *Mymx* locus from *Mymx*$^{+/R46*}$ heterozygous mice. The mutations introduced can be observed as a dual peak in the chromatogram.

Deletion of the Mymx ectodomain impairs fusogenic activity in vitro

For further studies on Mymx^{R46*}, in vitro quantitative heterologous fusion assays were used[129]. In these assays, C2C12-mCherry-RLuc1 myoblasts are mixed with 10T1/2-GFP-RLuc2 fibroblasts, and myoblast differentiation was induced. Then, myoblast-fibroblast fusion was assessed by quantification of GFP^{+}; mCherry^{+} chimeric myofibers, and measurement of reconstituted luciferase activity (**Fig. 24a**). The only commercially available antibody against MYMX (Novus Biologicals, AF4580) recognizes the C-terminus of the protein, which is lost in Mymx^{R46*}. To overcome that limitation, we generated C-terminally tagged Mymx constructs that preserve fusogenic activity, as quantified by fusion assays (**Fig. 24a**). To better understand the contribution of the Mymx ectodomain to myoblast fusion in vitro, tagged constructs encoding Mymx^{R46*} and the Mymx

ectodomain (Mymx^{Ecto}) were tested in fusion assays (**Fig. 24a, b**). In the presence of Myomaker, full length Mymx strongly enhanced heterologous fusion, whereas Mymx^{R46*} and Mymx^{Ecto} failed to increase fusion, indicating that they are not functional. Immunofluorescence of tagged Mymx proteins revealed all constructs were expressed at similar levels and displayed similar vesicular localization (**Fig. 24c**). Thus, the ectodomain region lost in Mymx^{R46*} is essential for Mymx activity.

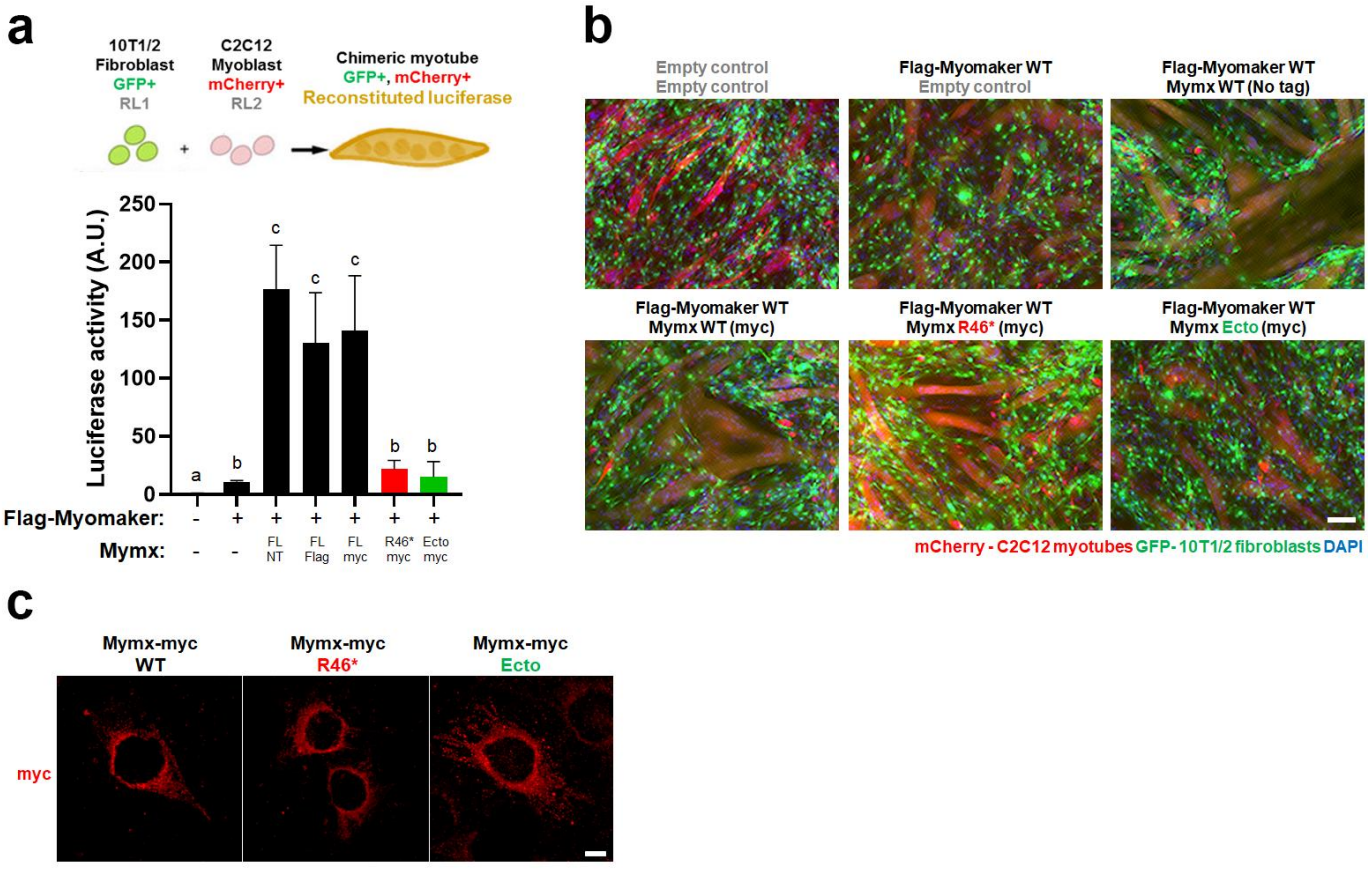

Fig. 24. Deletion of Mymx ectodomain impairs fusogenic activity in vitro.

a. Scheme for quantitative heterologous fusion assays. Fibroblasts expressing GFP and the first half of split luciferase were mixed with C2C12 myoblasts expressing mCherry and the second half of a split luciferase. Fusion could be observed by the presence of double positive mCherry^{+}; GFP^{+} myotubes, and measured using cell permeable luciferase substrates (upper panel). Luciferase measurements for heterologous fusion assays. Fibroblasts expressed the indicated constructs. FL: Full length. NT: No tag. Ecto: Ectodomain only. $p < 0.05$.

Error is expressed as standard deviation (lower panel). **b.** Microscopy images of the heterologous fusion assays shown in a. Scale bar: 50µm. **c.** Confocal immunofluorescence images of fibroblasts expressing the indicated myc tagged Mymx constructs. All constructs used were stable and localized correctly. Scale bar: 5µm.

Mymx ectodomain engages in hydrophobic interactions

Mymx^{Ecto} has been shown to be sufficient to induce cell-cell fusion by regulating membrane curvature when added in the media of Mymx KO myocytes[123]. Because Mymx^{Ecto} is an amphipathic protein, with abundant highly positively charged and hydrophobic residues, we hypothesized that such detergent-like properties may contribute to Mymx function as a physical membrane disruptor. To understand how Mymx^{Ecto} drives fusion, structural analysis by nuclear magnetic resonance (NMR) was performed with recombinant human Mymx ectodomain protein (rEcto). Codon optimized GST-rEcto was expressed in *E.coli* with a human rhinovirus (HRV) 3C cleavage site between GST and rEcto to allow for easy purification and separation of the tag. In contrast to prior studies[123], we observed that even after on-bead cleavage of GST, rEcto was retained on glutathione beads, and could only be released by using detergents (**Fig. 25a**). The same results were obtained when other tags were used for purification (MBP, His6). Therefore, two-dimensional heteronuclear single quantum coherence (HSQC) spectroscopy experiments with ^{15}N labeled rEcto were performed in the presence of 4mM CHAPS. In HSQC, proteins are magnetized to align the spin of all hydrogen protons in the sample. Then, magnetization is specifically transferred to the isotopically labeled ^{15}N nucleus of the amide group in the peptide bond. By measuring the energy released after the

process, it is possible to obtain information about the physicochemical environment of each peptide bond, and therefore, each residue of the protein. Initially, rEcto residues showed low dispersion in 2D-HSQC (**Fig. 25b**), indicating the lack of an organized structure or aggregation. However, when CHAPS concentration was increased to 25mM (CHAPS critical micellar concentration is 6mM[134]), and micelles were formed, a spectral shift was observed (**Fig. 25b**). Therefore, these data suggest that the properties of $Mymx^{Ecto}$ potentially change in a more hydrophobic environment, where the protein may be more structured.

The spectroscopic changes of rEcto in the presence of micelles suggest that, in cells, the ectodomain is unlikely to be continuously exposed to the hydrophilic extracellular space. Instead, the ectodomain may be embedded within the plasma membrane and in close proximity to its hydrophobic N-terminal transmembrane region. Co-immunoprecipitation assays in 293T cells showed that the N-terminal transmembrane helix of Mymx interacts with itself and with $Mymx^{Ecto}$, thus supporting an association between the two hydrophobic regions of the protein. No interaction was observed between $Mymx^{Ecto}$ proteins (**Fig. 25c**). To test the functional significance of these interactions, a split GFP system was used to control Mymx conformation[135] (**Fig. 25d**). The 11th β-strand complementary fragment of GFP was add to the C-terminus of Mymx (Mymx-M3). M3 engages in irreversible interactions with an asymmetrically split sGFP2 to reconstitute GFP. As sGFP2 is cytosolic, interaction between Mymx-M3 and sGFP2 would trap Mymx-M3 in an irreversible “closed” conformation only if the C-terminus of Mymx-M3 is facing the cytosol. Indeed, co-expression of Mymx-M3 and sGFP2 impaired Mymx activity in heterologous fusion assays (**Fig. 25e**). These results suggest that, in cells, Mymx may undergo an inside-out

conformational change to expose its fusogenic ectodomain. That process may be regulated by its association with the N-terminal transmembrane region, interactions with the hydrophobic environment, or potentially, other proteins.

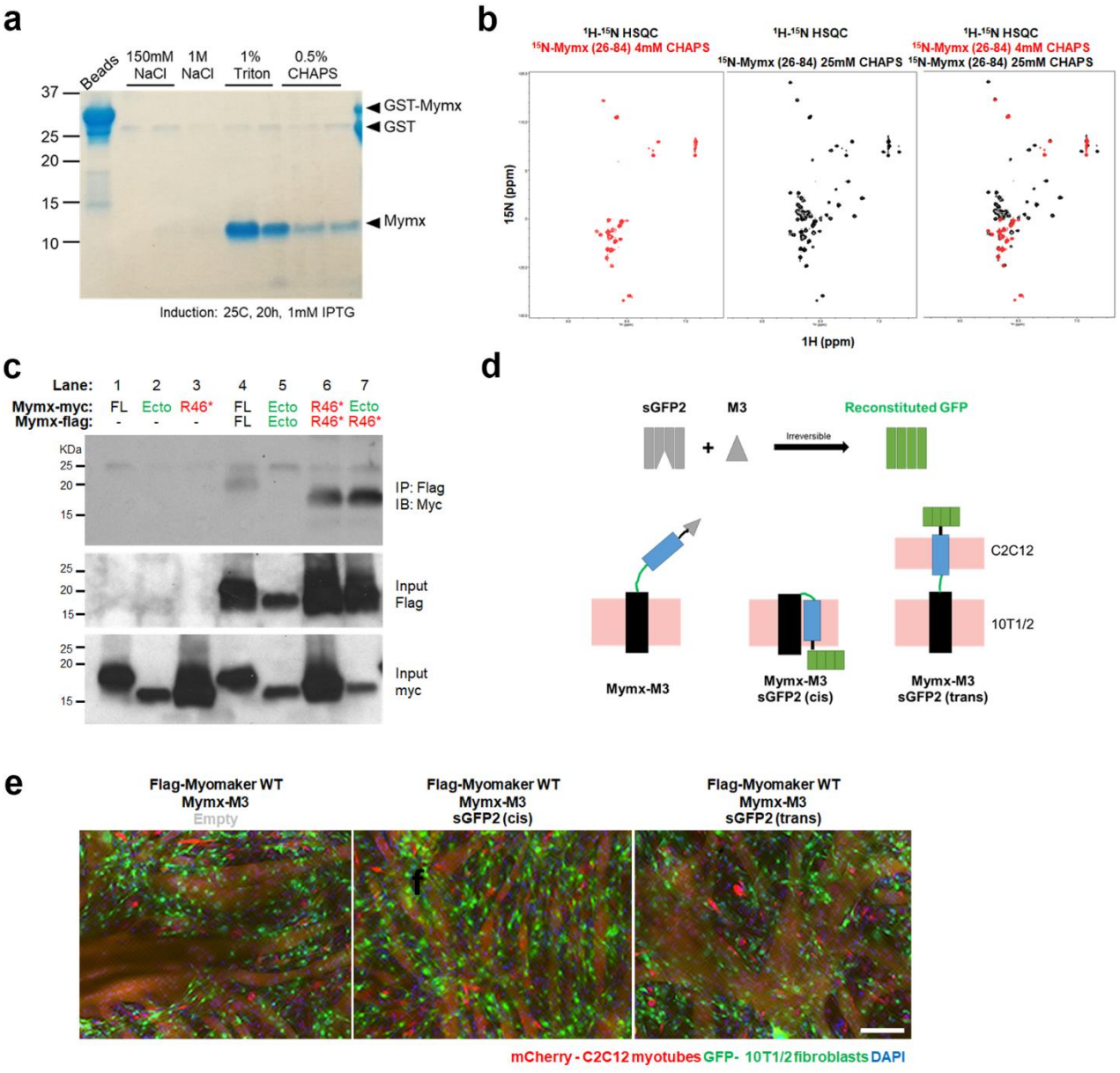

Fig. 25. Mymx ectodomain engages in hydrophobic interactions.

a. Comassie blue staining showing the efficiency of different solutions to elute Mymx. Arrowheads denote different proteins. Mymx was released from the GST tag by on-bed HRV-3C protease digest, but incubation with detergents (Triton

X100 or CHAPS) was required to release Mymx from the beads. **b.** 2D-(^{1}H-^{15}N)-HSQC spectra for Mymx ectodomain in 4mM CHAPS (red) and 25mM CHAPS (black). The axis shows arbitrary units (ppm: parts per million) that correlate the chemical shift of nitrogen to the hydrogen in the amide group of the peptide bond. In proteins with defined structures, each amino acid is in a specific location with a defined environment, resulting in a plot with as many “dots” as residues in the protein. In the case of Mymx, increasing CHAPS to 25mM caused the generation of micelles and increased dispersion of the protein spectra (ie. defined positions for specific amino acids, and therefore, a more defined structure). **c.** Co-immunoprecipitation assays with different myc or flag tagged Mymx constructs in 293T cells. FL: Full length. Mymx interacts with itself (4th lane) and pulldowns with Mymx truncations show that the interaction occurs between two Mymx^{R46*} regions of different proteins (6th lane) and between Mymx^{R46*}-Mymx^{Ecto} of different proteins (7th lane) or potentially, within the same protein. **d.** Scheme to regulate Mymx into closed or open conformation. A split GFP system was used in which a small helix of GFP (M3) can irreversibly associate with the rest of the protein (sGFP2) to reconstitute GFP. M3 was fused to the C-terminus of Mymx and sGFP2 was expressed in the same cell (cis) or different cell (trans) to force open or closed Mymx, respectively. **e.** Heterologous fusion assays with fibroblasts expressing Mymx-M3 and sGFP in cis or trans. Co-expression of Mymx-M3 and sGFP2 in the same cell (promoting closed Mymx) impaired fusion. Scale bar: 50µm.

4.3. Discussion and future directions

Developmental and postnatal myonuclear accretion is essential for muscle function. Nuclei within muscle fibers exert specialized functions and contribute to the transcriptional capacity of the cell[54,65-67], and impairment of myoblast fusion beyond a certain threshold cannot be compensated by the remaining nuclei[136]. Complete loss of fusion in mice causes neonatal death due to lack of diaphragmic contraction[120], and juvenile or adult deletion of Mymx or Myomaker precludes posterior adaptations to growth, increased mechanical load, and response to injury[120,132,137]. In humans, CFZS is the only known disease directly caused by defects in myoblast fusion. Fewer than 15 CFZS cases have been reported so far, and whole-exome sequencing of these patients revealed uncommon biallelic *MYOMAKER* combinations that resulted in uniquely compromised myoblast fusion levels, compatible with life but causing extensive abnormalities[133].

Our preliminary data implicate Mymx in the etiology of CFZS. By whole exome sequencing, we identified two patients with CFZS features harboring a potentially pathogenic *MYMX* allele ($Mymx^{R46*}$) in homozygosity. We are currently generating a humanized mouse model to better understand the contribution of $Mymx^{R46*}$ to the disease, and significant work is still required to characterize these mice. We hypothesize that $Mymx^{R46*}$ mice may present a severe myopathic phenotype, or even phenocopy Mymx KO mice. In both cases, detailed histological analysis will be required to quantify the extent of fusion in myofibers. The contribution of fusion and specific nuclei to muscle function and disease is an active area of research[67], and $Mymx^{R46*}$ is likely to represent the first mouse model for CFZS, a disorder caused by impairment in fusion. Therefore, it will be

of interest to analyze the transcriptional changes occurring in muscle when fusion is compromised, particularly at single-nucleus resolution.

In vitro studies with Myomaker mutants involved in CFZS revealed that, in most cases, the mutations caused instability, decreased protein levels, and therefore, decreased Myomaker activity[133]. In contrast, Mymx^{R46*} is stable in vitro, and shows no obvious differences in localization. The small length of Mymx (84 residues in humans) makes it amenable for mutagenesis analysis, and prior studies showed that disruption of the Mymx ectodomain by combined point mutations is sufficient to abolish its activity[119]. Similarly, evolutionary analysis of Mymx orthologs revealed that the only region strictly conserved across species is the extracellular AxLyCxL motif[127], which is lost in Mymx^{R46*}. Consistently, our data show that Mymx^{R46*} is not fusogenic by in vitro heterologous fusion assays, further indicating the likely pathogenicity of the human allele. In heterologous fusion assays, Myomaker is required for fusion in both fibroblasts and myoblasts, whereas Mymx is only required in one of the two cell types[120]. Furthermore, recent studies have shown that Myomaker is sufficient to induce some fusion by itself in the absence of Mymx when human cells were used in culture[138]. Thus, while our vitro data suggest that Mymx^{R46*} results in complete loss of function, it is likely that residual fusion or compensatory mechanisms may be in place in mice and humans to partially tolerate the mutation.

Cell and membrane fusion have been mechanistically studied in other biological processes. During neurotransmitter release, the proteins at the synaptic vesicle and the receiving plasma membrane interact with each other to form a trans-SNARE complex[125]. Additional protein-protein and protein-lipid interactions result in tightening of the complex and mixing of the membranes

(hemifusion) without cytosolic mixing. The formation of a stalk intermediate causes the SNARE complex to quickly reassemble on the same membrane (cis-SNARE), generating mechanical forces and lipid rearrangements that culminate with the opening of a fusion pore. In contrast, in viral and placental fusion (mediated by syncytins, proteins of viral origin), single proteins with long ectodomains can interact with membrane receptors and insert fusogenic peptides in the opposing membrane to destabilize it and open a fusion pore[124]. More recently, small reoviral proteins have been shown to facilitate cell-cell fusion by hijacking the host actin cytoskeleton[139]. In the case of myoblast fusion, Myomaker has been shown to be sufficient to promote membrane mixing between cells (hemifusion)[128]. Similarly, Mymx could be replaced and cytosolic mixing achieved by osmotic stress after promoting membrane curvature with lysophosphatidylcholine[123]. Typically, hemifusion intermediates are unstable and quickly lead to fusion[116,117]. Intriguingly, the reported results on Myomaker and Mymx suggest that, in myoblast fusion, membrane and cytosol fusion may be decoupled. However, the unique biochemistry of Myomaker and Mymx makes mechanistic studies technically challenging and all data must be taken cautiously. We originally reported that Myomaker and Mymx interacted with each other[119], and other groups were only able to observe an interaction between the two proteins after our original findings and protocols were available. Similarly, we and others (Dr. Bi and Dr. Ravaux, personal communication) have not been able reproduce the results of others concerning protein purification, membrane mixing, osmotic stress, or even lysophosphatidylcholine treatment. However, all studies agree on the potential function of Mymx as a membrane destabilizer through its hydrophobic ectodomain. Our structural data indicate that Mymx^{Ecto} likely

undergoes conformational rearrangements as opposing membranes approach each other, and the biochemical interactions we observed between the different regions of Mymx are reminiscent of the interactions in cis and trans observed in neurotransmitter membrane fusion. Considering the short length of $Mymx^{Ecto}$, it is unlikely that Mymx may be critically involved in multiple steps of the fusion process beyond opening of the fusion pore. Therefore, elucidating the structure of such a short yet functional protein will be of great interest to further understand the unique mechanisms behind myoblast fusion.

5. Concluding remarks

The research included in this thesis comprises a multidisciplinary approach to identify and characterize new players in muscle biology. The disciplines involved are diverse: human genetics, disease modeling in vivo and in vitro, multi-omics, and molecular and structural biology. This combination of techniques enabled us to understand new genes from their role in human disease, all the way to their mechanisms of action. Similarly, the topics of each project (proteostasis, fusion, and nuclear organization) and their associated challenges were very different. In the case of Klhl41, because of prior studies on related genes, it was necessary to focus on mechanistic studies in vitro. In contrast, myoblast fusion is a rapidly evolving area (oftentimes by contributions from current or former lab members) and finding the right relevant biological question to work on has been essential, especially as the CFZS project started during the worldwide COVID pandemic. Kelch proteins and myoblast fusion were ongoing research areas when I joined the Olson lab, but the initial work on Net39 is what sparked our interest in nuclear envelope biology and EDMD. I think we succeeded in exploiting the strengths of our laboratory to fill in a significant gap of knowledge in that field. As a result, the project has expanded to become an important part of other people's research in the lab as well.

Overall, this work is a testimony of the increasing need for integrative approaches and team effort to solve biological questions. All paths have strengths and weaknesses. Certainly, focusing on a single topic or techniques can be much more efficient and productive in the short term. However, I firmly believe that, as a graduate student, taking the time and risks to explore new questions and methods is the way to become a complete and versatile scientist for the future.

6. Methods

Generation of mouse models

All animal procedures were approved by the Institutional Animal Care and Use Committee at the University of Texas Southwestern Medical Center.

To generate knock-out and conditional Net39 alleles, CRISPR Cas9 guides flanking exon 1 of the *Net39* (also refered to as *Plpp7*) gene were selected from CRISPR 10K Genome Browser Track, cloned into pX458 (Addgene # 251928), transfected into N2a cells, FACS sorted, and cutting efficiency was assessed by T7E1 assay as per provider's instructions (New England BioLabs #E3321).

Net39-sgRNA-5' 5'-TCCCTGAACCAGCCCCCCAA-3'

Net39-sgRNA-3' 5'-GGGTTGGGCCGGCTCCCAGA-3'

Cas9 mRNA and Net39 sgRNAs were injected into the pronucleus and cytoplasm of zygotes. For zygote production, B6C3F1 female mice were treated for superovulation and mated to B6C3F1 stud males. Zygotes were isolated, transferred to M16 and M2 medium, injected with Cas9 mRNA and sgRNA, and cultured in M16 medium for 1h at 37ºC. Injected zygotes were transferred into the oviducts of pseudo-pregnant ICR female mice. Tail genomic DNA was extracted from F0 mice and used for genomic analysis with PCR primers that amplify the targeted region. For Net39 KO, primers 1 and 2 amplify fragments of different size in WT and KO mice. Primers 2 and 3 only amplify the WT allele.

#1 Net39-WT/KO-F 5'-GCAGCTGGAGGTAAATAGCC-3'

#2 Net39-WT/KO-R 5'-CTCCCCACACTAGAGGCTTG-3'

#3 Net39-WT.only-F 5'-GCAGATGTCAATAGCCAGCA-3'

For Net39^{fl}, the conditional allele presents a 36bp increase in size due to the insertion of loxP sites. The following primers were used for genotyping.

Net39-fl-F acttagccctagagacccaaca

Net39-fl-R cagggcagatccttcatagc

For Mymx^{R46*}, the sgRNAs used for injection were:

Mymx-sgRNA-5’ 5’-CAGAGCCTCTCTCATGTCTT-3’

Mymx-sgRNA-3’ 5’-CCTCAGCCAGCAACAGCCAC-3’

The Mymx^{R46*} allele was genotype by Sanger sequencing. The following primers were used for PCR:

Mymx-F 5’-GCGTGCCTGAGGTACAGTCT-3’

Mymx-R 5’-GTCAGAGCCCTCTTGCACTC-3’

Mosaic mice were mated to C57BL6N mice and a mouses lines were stablished. For Net39 KO, a 559bp deletion was selected for further characterization. Experiments requiring KO mice were sex balanced (2 males, 1 female per genotype). Experiments required cKO mice were performed with male mice.

For the Klhl41 KO line, mice were generated using a targeted Klhl41 embryonic stem cell clone (Klhl41$^{tm1a(KOMP)Wtsi}$) obtained from the KOMP Repository (http://www.KOMP.org) as previously described[118]. Klhl41+/– mice were intercrossed to generate KO mice. KO mice were maintained in a pure C57BL/6 background. Klhl41 genotypes was determined based on the presence or absence of WT and KO alleles using two genotyping reactions. The primers for Klhl41 span intron 1 (WT) or the targeted allele plus intron 1 (KO). The following primers were used:

KLHL41-WT-F AGAAAGTAAGTGCCAAAATGAATCC

KLHL41-WT-R AGGCTGACTGTGCTCCTAGGTGCTGTTC

KLHL41-KO-F GAGATGGCGCAACGCAATTAAT

KLHL41-KO-R CAGTTTCTCGTTCAGTTCTTCTCTG

Radioisotopic in situ hybridization

Radioisotopic in situ hybridization (ISH) was performed on E10.5, E12.5 and E15.5 embryo sections and modified from prior protocols[140]. For pre-

hybridization, embryo section slides were heated to 58°C for 30 minutes, deparaffinized in xylene and hydrated by sequential ethanol/DEPC-saline washes (95%, 85%, 60%, 30%) to DEPC-saline. Microwave RNA retrieval was performed in plastic containers (Miles Tissue-Tek, Elkhart, IN) filled with DEPC-1X Antigen Retrieval Citra pH 6.0 (Biogenex, San Ramon, CA), and samples were heated in a 750-watt microwave at 90% power for 5 minutes. Evaporated solution was replaced with DEPC-H_2O, and an additional heating was performed at 60% power for 5 minutes. Samples were cooled down for 20 minutes and washed twice in DEPC-PBS for 5 minutes. Samples were then permeabilized for 7.5 minutes with 20 µg/ml pronase-E in 50mM Tris-HCl, pH 8.0, 5mM EDTA, pH 8.0 in DEPC-H_2O. Samples were then washed in DEPC-PBS twice and re-fixed in 4% paraformaldehyde/DEPC-PBS, pH 7.4, for 5 minutes, washed in DEPC-PBS and acetylated in 0.25% acetic anhydride/0.1M triethanolamine–HCl, pH 7.5, twice for 5 minutes. Slides were then equilibrated in 1x SSC, pH 7.0, for 5 minutes, incubated in 50mM n-ethylmaleimide/1x SSC, pH 7.0, for 20 minutes and washed in DEPC-PBS, pH 7.4, and DEPC-saline. Finally, slides were dehydrated through graded ethanol/DEPC-saline rinses (30%, 60%, 85%, 95%) to absolute ethanol, and dried under vacuum for 2 hours.

mRNA probe sequences were synthesized by Integrated DNA Technologies (IDT) and cloned into pCRII-Topo vector (ThermoFisher, K460001) as per provider's instructions. MAXIscript SP6/T7 (Life Technologies, AM1320) was used for in vitro transcription of the probe. The following sequences were used as probes:

Net39:

CCTGCTGGCTATTGACATCTGCATGTCCAAGCGACTGGGGGTGTGTGCCG
GCCGGGCTGCATCCTGGGCCAGCGCCCGCTCCATGGTCAAGCTCATTGG
CATCACAGGCCACGGCATTCCTTGGATCGGGGGCACCATCCTCTGCCTGG
TGAGAAGCAGCACCCTGGCTGGCCAAGAGGTGCTCATGAACCTGCTGCTA
GCCCTGCTCTTGGACATCATGACAGTGGCTGGAGTCCAGAAGCTCATCAA
GCGCCGCGGCCCATATGAGACCAGCCCTGGGCTCCTGGACTACCTCACC
ATGGACATCTATGCCTTCCCTGCCGGCCACGCCAGCCGTGCCGCCATGGT
GT

Klhl41:

AGCTGGAATCTAAAGAGTTTGCACCCACTGAAGTCAATGACATATGGAAGT
ATGAAGATGATAAAAAAGAATGGGCTGGGATGCTGAAGGAAATCCGTTAC
GCTTCGGGAGCTAGTTGCCTAGCAACGCGCTTAAATCTGTTTAAACTGTCT
AAACTATAAAGGAGGTGACAAAGACACAGTTTGAGAGGTGGCTTGTTGGG
ACAAGAGGCTTTAATTTATTGTCATTCTTTAAGCCTATACAATGATTCACATA
GGGTTACAGGGATTCACGCAGTTTCTCTGGGGTAAAACAGTGTAACCGAA
TCCCAGAGATTTTCAGTGTGCCAAGTATAAAACCATTTGCTAGGAAGTTTA
GTATTCAGTTGAACAATATATTTTTTTTTTTTTTTTTTTGGTTTTTTGAGACA
GGGTTTCTCTGTATAGC

The probe was diluted in hybridization mixture (50% formamide, 0.75M NaCl, 20mM Tris-HCl, pH 8.0, 5mM EDTA, pH 8.0, 10mM $NaPO_4$, pH 8.0, 10% dextran sulfate, 1x Denhardt's, and 0.5 mg/ml tRNA) to achieve $7.5x10^3$cpm/µl and heated to 95°C for 5 minutes. Diluted probe was cooled to 37°C and DTT was added to a final concentration of 10mM. The probe was applied over the sections in a Nalgene Nalgene utility box lined with 5x SSC/50% formamide-saturated gel blot paper. Hybridization was performed for 14 hours at 70°C. After hybridization, slides were washed as follows: 5x SSC/10 mM DTT at 55°C for 40 minutes, HS (2x SSC/50% formamide/100mM DTT) at 65°C for 40 minutes, three 10 minute washes in NTE (0.5 M NaCl/10 mM Tris-HCl, pH 8.0/5 mM EDTA, pH 8.0) at 37°C, NTE with RNase-A (2 µg/ml) at 37°C for 30 minutes, NTE at 37°C for 15 minutes, HS at 65° for 30 minutes, 2 washes in 2xSSC and 0.1xSSC each at 37°C for 15 minutes. Slides were then dehydrated in graded ethanol rinses (30%, 60%, 85%, 95%) to absolute ethanol, and dried under vacuum. For autoradiographic exposure, dried slides were added pre-warmed (42°C) diluted Ilford K.5 nuclear emulsion (Polysciences, Warrington, PA) and dried at room temperature at 75% humidity for 3 hours. Slides were then sealed with desiccant and stored at 4°C for 28 days. After that, samples were developed in D19 (Eastman Kodak, Rochester, NY) at 14°C and the latent image was fixed with Kodak Fixer. After rinsing, hematoxylin counter-staining was performed (Richard-Allen, Kalamazoo, MI), and samples were dehydrated and mounted. Net39 expression was observed with a Leitz Laborlux-S microscope stand

equipped with Plan-EF optics, a standard bright-field condenser, and a Mears low-magnification dark-field condenser.

Northern blot analysis

Tissues were harvested from 8 week old C57BL/6 mice and flash-frozen in liquid nitrogen. Total RNA was extracted from tissue with TRIZOL reagent (Invitrogen) according to manufacturer instructions. The in-situ hybridization probe sequence was used to generate the Northern blot probe by labeling with [α-^{32}P]dCTP using the RadPrime DNA Labelling System (Invitrogen), as per manufacturer's instructions. As a loading control, 28S and 18S rRNAs from gel run were visualized.

Ex vivo electrophysiology

Extensor digitorum longus (EDL) and soleus muscles were isolated from postnatal day 17 (P17) mice and mounted on Grass FT03.C force transducers connected to a Powerlab 8/SP data acquisition unit (AD Instruments), under physiological salt solution at 37°C, and continuous flux of 95% O_2–5% CO_2. Muscles were adjusted to initial length at which the passive force was 0.5g and then stimulated with two platinum wire electrodes to establish optimal length for obtaining maximal isometric tetanic tension. Measurements were normalized to specific force (mN/mm2) to account for tissue cross-sectional area. For fatigue assays, after reaching optimal muscle length, muscles were stimulated for 20s (fatigability measurements) or 10 minutes (for electron microscopy) at 0.8 Hz, 50ms. Fatigue curves were calculated by comparing the relative change in force to the initial peak (considered 100%).

Histology, immunochemistry, and electron microscopy

Skeletal muscle tissues were flash-frozen in a cryoprotective 3:1 mixture of tissue-freezing medium (Triangle BioSciences International) and gum tragacanth (Sigma, G1128) and sectioned on a cryostat and routine hematoxylin

and eosin staining was performed. For SDH staining, unfixed frozen sections were incubated in 0.2 M phosphate buffer (pH 7.6) containing sodium succinate and nitroblue tetrazolium chloride (NBT) for 60 min at 37 °C (21). For NADH staining, unfixed frozen sections were incubated in 0.05 M Tris buffer (pH 7.6) containing NADH and NBT for 30 min at 37 °C[45]. Sections were cleared with acetone and mounted in aqueous medium. Cytochrome oxidase (COX) activity was detected in unfixed frozen sections by incubation for one-hour at room temperature in 1mg/ml cytochrome C (Sigma, C2506) / 6mg/ml catalase (Sigma, C40) / 0.5mg/ml 3,3-diamonobenzidine tetrachloride (Sigma, D5637) in phosphate buffered saline, pH 7.4. Upon conclusion of incubation, sections were washed in distilled water, dehydrated, cleared, and coverslips mounted with synthetic mounting medium (ThermoFisher, SP15-100). Gomori's trichrome staining was performed as previously described[141].

For immunofluorescence, cryosections were fixed in 4% paraformaldehyde for 15 minutes and permeabilized in 0.3% Triton X-100 for 15min. Sections were blocked with mouse on mouse (MOM) blocking solution (Vector Labs, BMK-2202) and 5% goat serum. Primary and conjugated Alexa Fluor secondary antibodies (ThermoFisher) were used at 1:200 dilution. The following antibodies and conjugated fluorophores were used: Sun2 (Sigma, MABT880), Lamin A (Abcam, ab26300), Lemd2 (Sigma, HPA017340), Mef2c (Cell Signaling, #5030), cleaved caspase-3 (Cell Signaling, #9661) Myh7 (BA-D5, DSHB), Myh2 (DSHB, SC-71), Myh4 (DSHB, BF-F3), Myh3 (DSHB, F1.652), Pax7 (DSHB, PAX7-c), Sv2 (DSHB, SV2-c), Neurofilament (DSHB, 2H3-c), Desmin (Dako, M0760, clone D33), Laminin (Sigma, L9393), α-actinin (Sigma, A7811) α-Bungarotoxin-555 (ThermoFisher, B35451), Phalloidin-488 (ThermoFisher, A12379), Wheat germ agglutinin-488 (ThermoFisher, W11261). Confocal images were obtained in Zeiss LSM 800. Myofiber diameter was measured with CellProfiler.

For electron microscopy of whole muscle, mice were perfused with 4% paraformaldehyde and 1% glutaraldehyde in 0.1M sodium cacodylate buffer (pH 7.4) and stained with 1% osmium tetroxide. For electron microscopy after ex vivo stretching, muscles were immediately fixed after 10 minutes of stimulation and contraction. Samples were processed by the University of Texas Southwestern

Medical Center Electron Microscopy Core facility. Images were acquired using a FEI Tecnai G2 Spirit transmission electron microscope.

Plasmids and cloning

The open reading frame for Net39 was obtained in pCMV6-Entry backbone (Origene, MR203615). Net39 ORF was subcloned into the following custom-made pMXs-puro (Cell Biolabs, RTV-012) backbones: pMXs-puro-3xFLAG-HA (C-terminal) and pMXs-puro-miniTurbo (C-terminal). pMXs-puro-miniTurbo was generated by conventional cloning using pcDNA-V5-miniTurbo-NES (Addgene, #107170) as the PCR template.

Tagged KLHL40, LMOD3 and NEB_{frag} plasmids were cloned as previously described[19]. A fragment of FLNC (amino acids 2133–2725) cloned into pcDNA3.1-FLAG was used from previous studies[142]. A fragment of NRAP (NCBI reference sequence NM_008733.4, nucleotides 162–1106) was cloned into pcDNA3.1-myc by conventional PCR using a synthetic gBlock (Integrated DNA Technologies) as template. KLHL41 was cloned from mouse quadriceps cDNA using Phusion High-Fidelity DNA Polymerase (NEB) and the following primers:

KLHL41-F: gatgaattcGATTCCCAGCGGGAGCTTGCAGA

KLHL41-R: gctcgagTTATAGTTTAGACAGTTTAAACAGATTTAAGCGCG

KLHL41 was then subcloned into pcDNA3.1-FLAG, pcDNA3.1-myc and pCS2-3xFLAG-HA. For tandem affinity purification, N-terminal tagged pCS2-3xFLAG-HA-KLHL41 was subcloned into pBx vector. Domain deletions of KLHL41 were generated by conventional PCR and cloned into pcDNA3.1-FLAG. The deleted regions were (numbers correspond to nucleotides in NCBI reference sequence NM_028202.3): ΔBTB (78-467), ΔBACK (518-788) and ΔKR (789-1898). For generation of ΔBACK, 2 PCR products were used for triple ligation. Domain deletion mutants were subcloned into pCS2-3xFLAG-HA. NEB_{frag} deletions were generated by conventional PCR and triple ligation into pcDNA3.1(+). pRK5-HA-Ub-WT and pRK5-HA-Ub-K0 were a gift from Ted Watson (Addgene plasmids #17608 and #17603 respectively)[143]. The remaining HA-Ubiquitin mutants were cloned by conventional mutagenesis (QuikChange

Lightning Site-Directed Mutagenesis Kit, Agilent) using HA-Ub-WT as template. CUL3 was cloned from mouse quadriceps cDNA into C-terminal myc pcDNA3.1 (Invitrogen) using Phusion High-Fidelity DNA Polymerase (NEB) and the following primers:

CUL3-F: TAAGCAGGTACCCGCCACCATGTCGAATCTGAGCAAAGGC

CUL3-R: TGCTTACTCGAGTGCTACATATGTGTATACTTTGCGATC

The plasmids for Myomaker and Mymx overexpression and heterologous assays were generated and described in prior publications[119,129] or modified by regular PCR. Tagged Mymx was cloned into custom-made pMXs-puro-3xFLAG-HA (C-terminal) and pMXs-puro-myc (C-terminal). Mymx-M3 was generated by conventional PCR using a synthetic gBlock (Integrated DNA Technologies) as template.

Cell culture, overexpression and immunofluorescence

C2C12 mouse myoblasts, N2a neuroblastoma cells, HEK 293T cells, and Platinum E cells (Cell Biolabs, NC0066908) were cultured in 10% FBS with 1% penicillin/streptomycin in DMEM. Cells were transfected with FuGENE6 (Promega, #E2692) as per provider's instructions. 10µg of plasmid was used for 10cm plate transfection and 20µg of DNA was used for 15cm plate transfection. Platinum E cells were used for retroviral virus production. 48 hours after transfection, supernatants were collected and filtered through a 0.45 µm syringe filter. Virus was concentrated with Retro-X concentrator (Takara, 631456). After 16 hours of viral concentration, viral soup was centrifuged at 1,500g for 45 minutes and the pellet was resuspended in fresh growth media supplemented with polybrene (Sigma, H9268) at a final concentration of 8µg/mL. 24 hours after infection, cells had their media replaced with fresh growth media.

For immunofluorescence, C2C12 cells overexpressing pMXs-puro-Net39-3xFLAG-HA or empty pMXs-puro-3XFLAG-HA were differentiated into myotubes for 5 days, fixed in 4% paraformaldehyde for 15 minutes and permeabilized in 0.3% Triton X-100 for 15 minutes. Cells were blocked with 5% BSA in PBS for 1 hour and incubated in primary and secondary antibodies in blocking solution for

1 hour. The following antibodies were used at 1:200 dilution: mTOR (Cell Signaling, 2983), My32 (Sigma, M4276), M2-FLAG (Sigma, F1804).

COS-7 cells (American Type Culture Collection) in 60 mm dishes were transfected at 75% confluency using Fugene 6 (Promega) as per manufacturer's directions. A total of 5 ug of DNA was used for each transfection. 48 hr after transfection, cells were washed with PBS and lysed in IP-A for 15 min. Lysates were rotated for 1 hr at 4°C and centrifuged at 20,817 x *g* for 15 min. The pellet was discarded. Standard SDS-PAGE was performed. FLAG M2 (Sigma, F1804), mouse c-myc (ThermoFisher, R950-25), rabbit c-myc (Santa Cruz, sc-789), HA (ThermoFisher, 32–6700), GAPDH (EMD Millipore, MAB374), LC3 (Novus Biologicals, NB100-2220), and fibrillarin (Abcam, ab5821) antibodies were used for blotting. For solubility assays, the remaining pellet was solubilized in high detergent lysis buffer (50 mM Tris, 150 mM NaCl, 1% NP-40, 0.1% SDS), boiled and incubated for 24 hr at 4°C under constant mixing. For ubiquitination assays, cells were lysed in IP-A buffer supplemented with 10 mM N-ethylmaleimide (Sigma, E387), a deubiquitinase inhibitor. For HA-Ub co-immunoprecipitation, cells were lysed in high detergent lysis buffer with 10 mM N-ethylmaleimide and the final volume was diluted 1:2 with IP-A buffer.

For chemical treatments, MG132 (Sigma, C2211) or chloroquine (Sigma, C6628) was dissolved in DMSO and added to COS-7 at a final concentration of 10 µM for 24 hr and 12 hr, respectively. For cycloheximide pulse experiments, cycloheximide (Sigma, C7698) was resuspended in ethanol and added to COS-7 cells at a final concentration of 100 µg/ml.

Heterologous fusion assays

We developed a dual split luciferase/GFP assay to accurately quantify the fusion efficiency. The reporter system consists of a pair of chimeras (RL-DSP1 and RL-DSP2) encoding the N- or C-terminal portions of a fusion protein of Renilla luciferase and GFP protein (24). The original pRluc8155-156-DSP1–7 (RL-DSP1) and pRluc8155-156-DSP8–11 (RL-DSP2) sequences were kindly provided by Zene Matsuda[144] (Institute of Medical Science, University of Tokyo, Tokyo, Japan) and subcloned into pMXs-puro using conventional PCR. Initially,

two different cell populations expressing either RL-DSP1 or RL-DSP2, which are catalytically inactive, were generated. When both populations are mixed and fusion occurs, each fragment of the reporter protein spontaneously interacts. Thus, in chimeric myotubes, the reporter becomes active, and luciferase activity is used as a surrogate for fusion efficiency. Luciferase readings were performed after 5 days of culture in differentiation medium using a CLARIOstar microplate reader (BMG Labtech) and the cell-permeable ViviRen substrate (Promega, E6491). Medium was replaced with 50 µl of 60 µm ViviRen, and the cells were incubated for 12 min at room temperature before measuring the luciferase activity.

We first validated whether luciferase readings were able to quantitatively measure fusion. We initially generated a calibration curve using C2C12 myoblasts and expected luciferase activity to increase linearly with the amount of cells expressing the reporters. For this experiment, we generated three stable C2C12 cell lines expressing one component of the split system (C2C12-RL-DSP1 and C2C12-RL-DSP2) or only the puromycin resistance cassette (C2C12-Empty). Those populations were then mixed as follows: the amount of C2C12-RL-DSP2 was kept constant at 9,000 cells/well, whereas the amount of C2C12-RL-DSP1 was gradually increased up to 9,000 cells. Myotube formation was then induced for 5 days in differentiation medium (DM), and luminescence was measured. The luciferase signal was linearly proportional to the amount of C2C12-DSP1 cells throughout the range of cells used. Then we generated an equivalent calibration curve for heterologous myoblast–fibroblast fusion by mixing C2C12-RL-DSP2 cells with increasing amounts of 10T1/2-RL-DSP1 fibroblasts infected with either the empty vector (no fusion) or mouse myomaker plasmid. As expected, we also observed a high linearity within the range of cells used.

Western blot analysis and co-immunoprecipitation

Protein was isolated from flash-frozen muscle samples by addition of RIPA buffer (Sigma, R0278) and mechanical homogenization in Precellys Evolution (3x20s at 6800rpm). Protein concentration was determined by BCA assay (ThermoFisher, 23225) and equal amounts of protein among samples were used

for regular western blot and transfer in PDVF membrane (Millipore, IPVH00010).

For co-immunoprecipitation, stable cell lines of C2C12 myoblasts were generated by infection with retroviral pMXs-puro-Net39-3xFLAG-HA, empty pMXs-puro-3XFLAG-HA, pBx-3xFLAG-HA-Klhl41 or pBx-3xFLAG-HA-GFP. For each condition five 15cm plates were differentiated into myotubes for 5 days and processed for co-immunoprecipitation. Briefly, cells were washed with PBS and scraped on PBS. Cells were centrifuged at 500g for 5min and pellets resuspended in 1.5mL of 50mM Tris, 150mM NaCl, 0.2% Triton, supplemented with protease inhibitor cocktail (Sigma, 11697498001) and PhosSTOP phosphatase inhibitor cocktail (Sigma, 4906845001). FLAG pulldown and elution were performed using Anti-FLAG M2 Magnetic Beads (Sigma, M8823) and 3xFLAG peptide (Sigma, F4799) as per provider's instructions. Beads were washed with 50mM Tris, 350mM NaCl, 0.2% Triton before elution. 2% of the lysate was loaded for input and the rest was used for co-IP.

Blocking and antibody incubation were performed in 5% milk in TBS-Tween 0.1%. The following antibodies were used at a 1:200 concentration (primary) or 1:5000 (HRP-conjugated): NET39 (Sigma, HPA070252), LEMD2 (Sigma, HPA017340), SUN2 (Sigma, MABT880), Lamin A (Abcam, ab26300), LMNB1 (Abcam, ab16048), EMD (Santa Cruz, sc-25284), VCL (Sigma, V9131), GAPDH (Sigma, MAB374), TUBB (Abcam, ab6046), Histone H3 (Cell Signaling, 9715S), KlHL41 (Abcam, ab66605), LMOD3 (Proteintech, 14948-1-AP), NEB (Proteintech, 19706-1-AP), HRP-conjugated streptavidin (Thermofisher, N100), goat anti-Mouse IgG (H+L)-HRP Conjugate (Bio-Rad , 170-6516) and goat anti-Rabbit IgG (H+L)-HRP Conjugate (Bio-Rad, 170-6515). For mTOR signaling, western blot analysis was performed using 5% BSA for blocking and antibody incubation. The following antibodies were used at 1:200 concentration: AKT (Cell Signaling, 9272), RAPTOR (Cell Signaling, 2280), S6K (Cell Signaling, 9202), p-S6K (Thr389) (Cell Signaling, 9234), 4EBP1 (Cell Signaling, 9452) and p-4EBP1 (Ser65) (Cell Signaling, 9451). Immunodetection was performed using Western Blotting Luminol Reagent (Santa Cruz Biotechnology, sc2048).

Gene expression analysis

Flash-frozen mouse muscle samples were homogenized in 1mL of Trizol in Precellys Evolution (3x20s at 6800rpm). RNA was isolated using RNeasy Micro kit (Qiagen, 74004) as per provider's instructions. cDNA was synthesized using iScript Reverse Transcriptase (Bio-Rad). RNA-seq (n = 3 mice per genotype) was performed by the UT Southwestern Genomic and Microarray Core Facility.

For qRT-PCR, the following primers were used:

Gene	Name	Sequence (5' to 3')
Klhl41	RT1_Klhl41-E1.2-F	CTGTATGTGGACGAAGAAAATAAGG
Klhl41	RT1_Klhl41-E1.2-R	CCACCACATAGATTTTGTCATCTACT
Klhl41	RT1_Klhl41-E3.4-F	TTTTTCCAGCTTGATAACGTAACAT
Klhl41	RT1_Klhl41-E3.4-R	AGATTTTTCACTTCACTCCACTTTG
Klhl41	RT2_Klhl41-E3.4-F	CCAGCTTGATAACGTAACATCTGA
Klhl41	RT2_Klhl41-E3.4-R	AGATTTTTCACTTCACTCCACTTTG
Klhl41	RT1_Klhl41-E5.6-F	GAAGATGGTCTTTCAGCTTCAGTT
Klhl41	RT1_Klhl41-E5.6-R	AGTGGGTGCAAACTCTTTAGATTC
Klhl40	RT_Klhl40-F	CCCAAGAACCATGTCAGTCTGGTGAC
Klhl40	RT_Klhl40-R	TCAGAGTCCAAGTGGTCAAACTGCAG
Lmod3	RT_Lmod3-F	CCGCTGGTGGAAATCACTCCC
Lmod3	RT_Lmod3-R	ACTCCAGCTCCTTTGGCAGTTGC
Neb	RT_Neb-F	TGACTTGAGAAGTGATGCCATTC
Neb	RT_Neb-R	CTCTAGCGCCAATGTGGTGAC

For bulk RNA-seq, single-end raw reads with more than 30% nucleotide with phred quality scores less than 20 were filtered from further analysis. Quality-filtered reads were then aligned to the mouse reference genome (version GRCm38.mm10) using the HISAT2 aligner (v2.1.0). Aligned reads were then counted using featurecount (v 1.6.2) to assign read counts to each annotation gene id. DESeq2 R Bioconductor package[145] was used to normalize read counts and identify differentially expressed (DE) genes. KEGG[146] pathway data was downloaded using KEGG API (https://www.kegg.jp/kegg/rest/keggapi.html) and gene ontology (GO) data was downloaded from NCBI FTP (ftp://ftp.ncbi.nlm.nih.gov/gene/DATA/gene2go.gz). The enrichment of DE genes to pathways and GOs was calculated by Fisher's exact test in R statistical package. Differentially expressed genes were determined using cut-offs of fold

changes > 2 and an adjusted p-value of < 0.05.

snRNA-seq was performed as previously described[67]. Briefly, nuclei were isolation after gentle mincing and centrifugation (15 minutes at 1,500g). Library preparation was performed using Chromium Next GEM Single Cell 3′ Gene Expression v3.1 kit (10× Genomics) as per provider's instructions.

Chromatin accessibility analysis

The Assay for Transposase-Accessible Chromatin using sequencing (ATAC-seq) protocol was modified from prior published protocols[147]. Flash-frozen quadriceps muscle samples from P17 mice (n = 3 mice per genotype) were resuspended in 1 mL of homogenization buffer (5mM $CaCl_2$, 3mM Mg Acetate, 10mM Tris pH 7.8, 320mM Sucrose, 200µM EDTA, 0.1% NP-40, 0.05% BME, with cOmplete protease inhibitor cocktail (Sigma, 11697498001)) and disrupted with beads in Precellys Evolution (3x20s at 6800rpm). Lysate was sequentially filtered through 70 µm and 40 µm cell strainers, laid on top of sucrose buffer (1M sucrose, 3mM Mg acetate, 10mM Tris pH 7.8) and centrifuged at 1000g for 10 minutes. Nuclei in the pellet were permeabilized in 0.5mL of 0.3% Triton in PBS for 30 minutes and washed twice with resuspension buffer (10mM NaCl, 3mM Mg Acetate, 10mM Tris pH 7.8). Transposition and library preparation were performed using TDE1 Tagment DNA Enzyme (Illumina, 15027865) and Nextera DNA Library Prep Kit (Illumina, 15027866) as per manufacturer's instructions. Sequencing (n = 3 mice per genotype) was performed by the UT Southwestern Genomic and Microarray Core Facility.

Paired-end raw reads were mapped to the mouse reference genome (GRCh38/mm10) using bowtie2 (version 2.3.4.3) with parameter '–very-sensitive' enabled. Read duplication and reads that mapped to chrM were removed from downstream analysis. Peaks were called using findpeaks command from HOMER software package version 4.9, with parameter '–style dnase', and the FDR threshold (for Poisson p-value cutoff) was set to 0.001. Called peaks were merged from all samples and annotatePeaks.pl command was used to produce a raw count matrix. Differential peaks were identified using R package DEseq version 3.8. Differentially regulated peaks were determined using cut-offs of fold

changes > 2 and an adjusted p-value of < 0.05. To analyze the functional significance of peaks, Genomic Regions Enrichment of Annotations Tool (GREAT) was used with mm10 as the background genome and other parameters set as default.

ChIP-Seq

For Lamn A/C ChIP-seq, frozen hindlimb muscles (n = 3 mice per genotype) were crushed to powder and crosslinked in 10mL of PBS with 2% formaldehyde (Sigma, F8775) for 15 minutes at room temperature under rotation. Crosslinking was stopped with 1.5mL of 2.5M glycine. Samples were washed with PBS and incubated on ice for 10 minutes in Farham lysis buffer (5mM PIPES, 85mM KCl, 0.5% N-40, pH 8.0) before bead lysis in Precellys Evolution (3x20s at 6800rpm). Lysates were then incubated on ice for 20 minutes, and the supernatant was removed after centrifugation (1000g, 5 minutes). The remaining pellet was resuspended in TE and 0.2%SDS (10mM Tris-HCl pH 8.0, 1mM EDTA) and nuclei were sonicated on Bioruptor pico (Diagenode) for 10 cycles (30s on, 30s off). 1% of sheared DNA was saved for input and the rest was diluted 1:1 with in 1xTE 0.1% sodium deoxycholate, 1% Triton X-100 and added 8µg of Lamin A/C antibody (Santa Cruz, sc-7292 X) conjugated to 60µl of Protein G Dynabeads (ThermoFisher, 10003D). Lamin A/C immunoprecipitation was performed for 48 hours at 4ºC and beads were subsequently washed twice with RIPA buffer, 360mM NaCl RIPA buffer, LiCl buffer (250mM LiCl, 0.5% NP40, 0.5% deoxycholate, 1mM EDTA, 10mM Tris-HCl, pH 8.0) and TE buffer. DNA was released from the beads by addition of decrosslinking buffer (TE 0.3% SDS, 2mg/mL proteinase K) and incubation at 65ºC for 16 hours under constant mixing. RNA was then removed by incubation with 0.1µg/µl of RNase A and incubation at 37ºC for 1 hour under constant mixing. DNA was purified from the supernatant with Qiagen PCR purification kit (Qiagen, 28104).

For Net39 ChIP-seq, C2C12 cells infected with Ty1-Net39 were plated on 15cm dishes. 4 dishes were used per replicate. 5 days after differentiation, myotubes were crosslinked for 30 minutes with 4% PFA. ChIP-IT High Sensitivity Kit (Active Motif, 53040) was user as per provider’s instructions.

Sequencing (n = 3 mice per genotype and n = 2 for C2C12 myotubes) was performed by the UT Southwestern Next Generation Sequencing Core. Raw reads were mapped to the mouse reference genome (GRCh38/mm10) using bowtie2 (version 2.3.4.3) with default parameters. Duplicate reads were removed with 'mark duplicates' from Picard tools (v.2.10.3). To detect lamin-associated domains (LADs), Enriched Domain Detector (v.1.0) was used with a 10Kb bin size, gap penalty of 10 and a FDR-adjusted significance threshold of 0.05. Gain, loss and overlapping LADs between WT and KO samples were tallied using bedtools (v.2.29.0).

Metabolomics

Quadriceps from P17 WT and Net39 KO mice were harvested and flash-frozen in liquid nitrogen. Samples were homogenized in bead tubes with Precellys Evolution (3x20s at 6800rpm) in 1mL of methanol/water (80:20 vol/vol). 200µl of sample were transferred to a new tube with 800µl of ice-cold methanol/water (80:20 vol/vol). Samples were vortexed for 1 minute and centrifuged at 20,000g for 15 minutes at 4ºC. Supernatant was transferred to a new tube and dried with SpeedVac system. Samples were further processed and analyzed as described here and in prior protocols[148]: samples were reconstituted in 0.03% formic acid, vortexed and debris was removed by centrifugation. The supernatant was used for the metabolomic studies. Liquid chromatography with tandem mass spectrometry (LC-MS/MS) was performed with AB QTRAP 5500 liquid chromatography–triple quadrupole mass spectrometer (Applied Biosystems SCIEX). Two mobile phases were used for separation: 0.03% formic acid in water and 0.03% formic acid in acetonitrile. MultiQuant software v.2.1 (Applied Biosystems SCIEX) was used to review the chromatogram and integrate peak area. The peak area for each metabolite was normalized to the total ion count of that sample. Metabolite identification targeted for 458 metabolites and 445 metabolites were detected above the baseline set by cell-free samples. Statistical differences were determined via Partial Least Squares-Discriminant Analysis (PLS-DA).

Limma R Bioconductor package[149] was used to identify differentially

regulated pathways. KEGG[146] compound and pathway data was downloaded using KEGG API (https://www.kegg.jp/kegg/rest/keggapi.html). Differentially enriched pathways were determined by Fisher's exact test in R statistical package. Differentially regulated metabolites were determined using cut-offs of fold changes > 2 and an adjusted p-value of < 0.05. Raw data can be found in Supplementary Data 2.

Serum was collected from heart puncture and glucose, insulin, triglycerides, cholesterol, and ketones were analyzed using VITROS clinical diagnostics.

Mitochondrial DNA quantification

Flash-frozen quadriceps muscle samples P17 mice were homogenized in Trizol and phase-separated with chloroform. The interphase and organic phase containing DNA were added 4 M guanidine thiocyanate, 50 mM sodium citrate and 1M Tris, mixed, incubated at room temperature and centrifuged at 3.000g at 4C. The upper phase was transferred to a new tube and DNA was precipitated with isopropanol. DNA pellets were washed four times with 75% ethanol, resuspended in 8mM NaOH and added HEPES and EDTA to a final concentration of 10mM and 1mM, respectively. The following primers were used for mtDNA qPCR (MT-MD1) and normalization (LPL):

NADH dehydrogenase subunit 1 (MT-ND1) Forward:

5'-CCCATTCGCGTTATTCTT-3'

NADH dehydrogenase subunit 1 Reverse: 5'-AAGTTGATCGTAACGGAAGC -3'

LPL Forward:

5’-GGATGGACGGTAAGAGTGATTC-3’

LPL Reverse:

5’-ATCCAAGGGTAGCAGACAGGT-3’

Proximity biotinylation in C2C12 cells

Proximity biotinylation (BioID) was adapted from prior publications[150]. C2C12 myoblasts expressing pMXs-puro-Net39-miniTurbo were plated on ten 15cm dishes at 100% confluence and differentiated in DM (DMEM with 2% horse serum and 1% antibiotic-antimycotic) (ThermoFisher, 26050088) for 7 days. Five 5cm dishes were supplemented with 500µM biotin (Sigma, B4501) for 4 hours. The remaining five 15cm dishes were used as negative control. Cell lysates were extracted in 1ml of lysis buffer (6M urea, 10% SDS, supplemented with cOmplete protease inhibitor cocktail and PhosSTOP phosphatase inhibitor cocktail) and lysed mechanically with Precellys Evolution (3x20s at 6800rpm). Lysates were added to 9ml of dilution buffer (50mM Tris, 150mM NaCl) and 100µl of equilibrated streptavidin magnetic beads (ThermoFisher, 88816). Lysates were incubated for 24 hours at 4ºC on a wheel. Beads were washed 5 times with lysis buffer and boiled for 10min in 2xLaemmli sample buffer (Bio-Rad, 1610737). Pulldown was assessed by silver staining (ThermoFisher, LC6070).

For protein identification by mass spectrometry, samples were run for 1cm in an Any-KD Mini-PROTEAN 10-well gel (Bio-Rad, # 4569034). Gels were then fixed and stained with EZBlue (Sigma, G1041) as per provider's instructions. The area of the gel containing proteins was cut into small 1mm cubes and submitted for analysis to the Proteomics Core Facility at University of Texas Southwestern Medical Center. Gel band samples were digested overnight with trypsin (Pierce) following reduction and alkylation with DTT and iodoacetamide (Sigma). The samples then underwent solid-phase extraction cleanup with an Oasis HLB plate (Waters) and the resulting samples were injected onto an Orbitrap Fusion Lumos mass spectrometer coupled to an Ultimate 3000 RSLC-Nano liquid chromatography system. Samples were injected onto a 75 µm i.d., 75-cm long EasySpray column (Thermofisher) and eluted with a gradient from 0-28% buffer B over 90 minutes. Buffer A contained 2% (v/v) ACN and 0.1% formic acid in water, and buffer B contained 80% (v/v) ACN, 10% (v/v) trifluoroethanol, and 0.1% formic acid in water. The mass spectrometer operated in positive ion mode with a source voltage of 1.8 kV and an ion transfer tube temperature of 275°C. MS scans were acquired at 120,000 resolution in the Orbitrap and up to 10 MS/MS spectra were obtained in the ion trap for each full spectrum acquired

using higher-energy collisional dissociation (HCD) for ions with charges 2-7. Dynamic exclusion was set for 25 s after an ion was selected for fragmentation.

Raw MS data files were analyzed using Proteome Discoverer v2.2 (Thermofisher), with peptide identification performed using Sequest HT searching against the mouse protein database from UniProt along with the sequence for Net39-miniTurbo. Fragment and precursor tolerances of 10 ppm and 0.6 Da were specified, and three missed cleavages were allowed. Carbamidomethylation of Cys was set as a fixed modification, with oxidation of Met set as a variable modification. The false-discovery rate (FDR) cutoff was 1% for all peptides. Two independent experiments for BioID were performed.

For analysis of enriched hits, results were filtered by enrichment (>20-fold enrichment in “Biotin” samples over “Control” samples) and ordered by abundance. The top 50 highest hits were selected for analysis on STRING and the 5 most enriched gene ontology terms were represented.

Luciferase assays

A region 442bp upstream of the open reading frame of Net39 was used for promoter analysis based on MyoD ChIP-seq data on C2C12 differentiation. Net39 promoter WT or with mutated E-boxes (Mut) were synthesized by Integrated DNA Technologies (IDT) and cloned into the promoterless luciferase reporter pGL4.10[luc2] (Promega, E6651) by conventional cloning. HEK 293T cells were transfected with combinations of reporter and either pCS2-GFP or pcDNA-MyoD-VP16. pcDNA-MyoD-VP16 encodes the bHLH domain of MyoD fused to the activation domain of VP16 and has been previously characterized[151]. The DesMef reporter has been previously described[9,56]. All samples were transfected pCMV-LacZ for normalization of cell numbers. 48 hours after transfection, luciferase assays were performed using Luciferase assay system (Promega, E1500) and beta-galactosidase assays were performed with Mammalian beta-Galactosidase Assay Kit (Thermofisher, 75707) as per provider’s instructions. Luminescence and absorbance (405nm) were read in a CLARIOstar plate reader (BMG Labtech).

Quantitative proteomic analysis of skeletal muscle

Hindlimb muscle from P0 mice (n = 3 mice per genotype) was collected for quantitative proteomic analysis by 10-fraction LC/LC-MS/MS by Proteomics and Metabolomics Shared Resource at Duke University. For sample preparation, each sample was added 8 M urea in 50 mM ammonium bicarbonate, pH 8.0 at a constant 10 µL per mg of tissue. Samples were then subjected to mechanical disruption using a Tissue Tearer followed by 2 rounds of probe sonication on ice at 30% power. Samples were spun to remove insoluble material and 4 µL was removed and subjected to Bradford assay to determine protein quantity. From each sample, 100 µg of total protein was removed and concentrations were normalized. Samples were then diluted in 1.6M urea with 50 mM ammonium bicarbonate. All samples were reduced for 20 min at 80°C with 10 mM dithiothreitol and alkylated for 40 min at room temperature with 25 mM iodoacetamide. Trypsin was added to a 1:50 ratio (enzyme to total protein) and allowed to proceed for 18 hr at 37°C. Samples were then acidified with 0.2% TFA (pH 2.5) and subjected to C18 SPE cleanup (Sep-Pak 50 mg bed). Following elution, all samples were frozen and lyophilized to dryness. For TMT labeling, each sample was resuspended in 100 µL 200 mM triethylamonium bicarbonate, pH 8.0. Fresh TMT reagents (0.8 mg for each 6-plex reagent) were resuspended in 100 µL acetonitrile. 50 µL of each TMT tag was added to a specific sample and incubated for 4 hr at room temperature. Afterwards, 8 µL 5% hydroxylamine was added to quench the reaction. 20% of each sample were combined at 1:1:1:1:1:1 ratio and was then lyophilized to dryness prior to LC/LC-MS/MS analysis. Quantitative two-dimensional liquid chromatography-tandem mass spectrometry (LC/LC-MS/MS) was performed on approximately 5 µg of protein digest per sample. The method uses two-dimensional liquid chromatography in a high-low pH reverse phase/reverse phase configuration on a nanoAcquity UPLC system (Waters Corp.) coupled to a Thermo QExactive Plus high resolution accurate mass tandem mass spectrometer with nanoelectrospray ionization. Peptides were first trapped at 2 ul/min at 97/3 v/v water/MeCN in 20 mM ammonium formate (pH 10) on a 5 µm XBridge BEH130 C18 300 µm x 50 mm column (Waters Corp.). A series of step-elutions of MeCN at 2 µl/min was used to elute peptides from the 1st dimension column. Ten steps of 14.0%, 16.0%, 17.3%,

18.5%, 20.3%, 22.0%, 23.5%, 25.0%, 30.0% and 50.0% MeCN were utilized for the analyses; these percentages were optimized for delivery of an approximately equal load to the 2nd dimension column for each fraction. For 2nd dimension separation, the elution of the 1st dimension was first diluted 10-fold online with 99.8/0.1/0.1 v/v/v water/MeCN/formic acid and trapped on a 5µ Symmetry C18 180 µm x 20 mm trapping column (Waters Corp.). The 2nd dimension separations were performed using a 1.7 µm Acquity BEH130 C18 75mmx250mm column (Waters Corp.) using a 90 min gradient of 3% to 25% acetonitrile with 0.1% formic acid at a flow rate of 400 nL/min with a column temperature of 55°C. Data collection on the QExactive Plus mass spectrometer was performed in a data-dependent acquisition mode of acquisition with a r = 70,000 (at m/z 200) full MS scan from m/z 375–1600 with a target AGC value of 1e6 ions followed by 20 MS/MS scans at r = 17,500 (at m/s 200) at a target AGC value of 5e4 ions. A 30 s dynamic exclusion was employed to increase depth of coverage. The total analysis cycle time for each sample injection was approximately 2 hr.

Following the 10 LC-MS/MS analyses, raw data were processed by Protein Discoverer to create MGF files. These MS/MS data were searched against a SwissProt_Mouse database within Mascot Server (Matrix Science) that also contained a reversed-sequence ‘decoy’ entry for each protein for false positive rate determination. Because mouse nebulin (NEB) is not a reviewed entry in SwisProt_Mouse, the unreviewed entry E9Q1W3_MOUSE was manually included in the analysis. Search tolerances were 5ppm precursor and 0.02 Da product ions with full trypsin protease rules and up to two missed cleavages. Search results were imported to Scaffold Q + S v4.4.6 (Proteome Software) and data was annotated at a Protein False Discovery Rate of 1.0%. The overall dataset yielded identifications for 23,910 TMT labeled peptides corresponding to 4,418 TMT labeled proteins. Only peptides uniquely identified to a protein were considered. To normalize the six different channels to account for differences in labeling efficiencies and mixing percentages, the summed intensity for each channel was calculated and then normalized to the 126 channel. Then, protein level intensities were generated by summing all of the unique peptide intensities to that protein.

For representation, proteins more than 30% up- or down- regulated were

selected as input for Morpheus (https://software.broadinstitute.org/morpheus/). Z-score was used for heat map scale. For pathway analysis, a list of significantly up- or down-regulated proteins was used as input for DAVID analysis of enriched GO Terms related to biological pathways[88].

Transthoracic echocardiography (ECHO)

Cardiac function was determined by two-dimensional echocardiography using the Visual Sonics Vevo 2100 Ultrasound (Visual Sonics, Toronto, Ontario, Canada) on conscious WT and Net39 KO mice at P9 and P17. Fractional shortening (FS) was calculated according to the following formula: $FS(\%) = [(LVID;d - LVID;s)/LVID;d]\times 100$. Left ventricular internal diameter (LVID) was measured as the largest anteroposterior diameter in either diastole (LVID;d) or systole (LVID;s). Ejection fraction (EF%) was calculated by: $EF(\%)=([EDV - ESV]/EDV)\times 100$. EDV, end diastolic volume; ESV, end systolic volume[152].

Case selection and tissue processing

The use of medical record and human tissues for research purposes was compliant with the ethical principles in the Belmont Report, the Department of Health and Human Service (DHHS) human subject regulations, Title 21 CFR, as well as good clinical practice (GCP) as adopted by the FDA, and approved by the UTSW Human Research Protection Program (IRB# STU012016-082). A waiver of patient informed consent was requested and approved by the human research protection program for retrospective study on archived human muscle tissue.

The pathology database at UTSW Medical Center was retrospectively reviewed. Among 10,070 muscle biopsies received between 1980 and 2016, three patients genetically confirmed to harbor Lamin A/C mutations and with available frozen muscle tissues were identified. Three normal muscle specimens from age-matched individuals served as controls. Muscle biopsies were collected from alive individuals and stored at -80ºC. Slides and electron microscopy images from all cases were reviewed by an experienced neuropathologist. Human muscle biopsy tissues were collected, processed and analyzed according to all ethical

regulations. 20μm-thick cryosections from each muscle specimen were collected for western blot, immunofluorescence, and qRT-PCR analyses. The analysis of human muscle samples was performed by independent researchers. RNA was isolated using RNeasy Micro kit (Qiagen, 74004) as per provider's instructions. cDNA was synthesized using iScript Reverse Transcriptase (Bio-Rad). A Taqman probe (Hs00262043_m1, Thermofisher), was used for qRT-PCR analysis. Protein samples were extracted as described in prior sections.

Structural studies on the Mymx ectodomain

The ORF for human Mymx ectodomain (residues 26-84) was codon-optimized for *Escherichia coli*, synthesized by Integrated DNA Technologies (IDT) and cloned into pGEX-6P1 (Addgene# 61838) by conventional PCR. The construct was transformed into NEBExpress bacterial cells (New England Biolabs, C2523H).

For protein purification, bacteria were grown in M9 media with isotopically labeled $^{15}NH_4Cl$ as the sole source of nitrogen (Sigma, 299251). 10 liters of bacteria were induced for 18 hours at 25C with 0.25mM IPTG (Biomatik, A2903). Bacteria were spun (1,000g for 15 minutes) and the pellet was solubilized in 20mM HEPES, 500mM NaCl, 10% v/v glycerol, 1mM EDTA, 1mM DTT, 1% Triton X-100, 0.2mg/mL lysozyme, pH 7.4. Samples were sonicated (10 minutes, 3 seconds ON, 3 seconds OFF, 40% power), spun (30 minutes, 8,000g) and added glutathione beads (Thermo Fisher, 16100) overnight at 4C (2mL per liter of culture). Beads were washed with 20mM HEPES, 1M NaCl, 10% v/v glycerol, 1mM EDTA, 1mm DTT, 1% Triton X-100, pH 7.4. The GST tag was then cleaved by on-bead incubation with HRV-3C protease (kindly provided by Dr. Yun-Zu Pan) overnight at 4C in 20mM HEPES, 150mM NaCl, 1mM DTT, pH 7.4. Samples were eluted in HRV-3C protease buffer with 4mM CHAPS (Sigma, 10810118001). Spectroscopic studies were performed in 4mM CHAPS and 25mM CHAPS[153] in an Agilent DD2 spectrometer operating at 600 MHz and equipped with cold probe and analyzed as previously described[154-156].

Statistics

Data are presented as mean ± SEM. For histological and cellular experiments, statistical analysis was performed using one or two-tailed unpaired t-tests, as indicated in each figure legend. For genome-wide and metabolomics analysis, a fold change > 2 and FDR <0.05 was used. Benjamini and Hochberg procedure was used for multiple hypothesis testing. Sample sizes and p-values are indicated in each figure.

7. References

1 Frontera, W. R. & Ochala, J. Skeletal muscle: a brief review of structure and function. *Calcif Tissue Int* **96**, 183-195, doi:10.1007/s00223-014-9915-y (2015).

2 Hill, J. & Olson, E. N. *Muscle: Fundamental Biology and Mechanisms of Disease* 1st edn, (Academic Press, 2012).

3 Chal, J. & Pourquie, O. Making muscle: skeletal myogenesis in vivo and in vitro. *Development* **144**, 2104-2122, doi:10.1242/dev.151035 (2017).

4 Gibb, S., Maroto, M. & Dale, J. K. The segmentation clock mechanism moves up a notch. *Trends Cell Biol* **20**, 593-600, doi:10.1016/j.tcb.2010.07.001 (2010).

5 Tajbakhsh, S. & Buckingham, M. The birth of muscle progenitor cells in the mouse: spatiotemporal considerations. *Curr Top Dev Biol* **48**, 225-268, doi:10.1016/s0070-2153(08)60758-9 (2000).

6 Buckingham, M. Myogenic progenitor cells and skeletal myogenesis in vertebrates. *Curr Opin Genet Dev* **16**, 525-532, doi:10.1016/j.gde.2006.08.008 (2006).

7 Buckingham, M. & Vincent, S. D. Distinct and dynamic myogenic populations in the vertebrate embryo. *Curr Opin Genet Dev* **19**, 444-453, doi:10.1016/j.gde.2009.08.001 (2009).

8 Liu, N. *et al.* Requirement of MEF2A, C, and D for skeletal muscle regeneration. *Proc Natl Acad Sci U S A* **111**, 4109-4114, doi:10.1073/pnas.1401732111 (2014).

9 Haberland, M. *et al.* Regulation of HDAC9 gene expression by MEF2 establishes a negative-feedback loop in the transcriptional circuitry of muscle differentiation. *Mol Cell Biol* **27**, 518-525, doi:10.1128/MCB.01415-06 (2007).

10 Deries, M., Schweitzer, R. & Duxson, M. J. Developmental fate of the mammalian myotome. *Dev Dyn* **239**, 2898-2910, doi:10.1002/dvdy.22425 (2010).

11 Yamakawa, H., Kusumoto, D., Hashimoto, H. & Yuasa, S. Stem Cell Aging in Skeletal Muscle Regeneration and Disease. *Int J Mol Sci* **21**, doi:10.3390/ijms21051830 (2020).

12 Liu, N. *et al.* A Twist2-dependent progenitor cell contributes to adult skeletal muscle. *Nat Cell Biol* **19**, 202-213, doi:10.1038/ncb3477 (2017).

13 Lovering, R. M., Porter, N. C. & Bloch, R. J. The muscular dystrophies: from genes to therapies. *Phys Ther* **85**, 1372-1388 (2005).

14 Barr, F. G. Gene fusions involving PAX and FOX family members in alveolar rhabdomyosarcoma. *Oncogene* **20**, 5736-5746, doi:10.1038/sj.onc.1204599 (2001).

15 Watson, C. M. *et al.* Deficiency of the myogenic factor MyoD causes a perinatally lethal fetal akinesia. *J Med Genet* **53**, 264-269, doi:10.1136/jmedgenet-2015-103620 (2016).

16 Zweier, M. *et al.* Mutations in MEF2C from the 5q14.3q15 microdeletion syndrome region are a frequent cause of severe mental retardation and diminish MECP2 and CDKL5 expression. *Hum Mutat* **31**, 722-733, doi:10.1002/humu.21253 (2010).

17 Robson, M. I. *et al.* Tissue-Specific Gene Repositioning by Muscle Nuclear Membrane Proteins Enhances Repression of Critical Developmental Genes during Myogenesis. *Mol Cell* **62**, 834-847, doi:10.1016/j.molcel.2016.04.035 (2016).

18 Liu, G. H. *et al.* Regulation of myoblast differentiation by the nuclear envelope protein NET39. *Mol Cell Biol* **29**, 5800-5812, doi:10.1128/MCB.00684-09 (2009).

19 Garg, A. *et al.* KLHL40 deficiency destabilizes thin filament proteins and promotes nemaline myopathy. *J Clin Invest* **124**, 3529-3539, doi:10.1172/JCI74994 (2014).

20 Gupta, V. A. *et al.* Identification of KLHL41 Mutations Implicates BTB-Kelch-Mediated Ubiquitination as an Alternate Pathway to Myofibrillar Disruption in Nemaline Myopathy. *Am J Hum Genet* **93**, 1108-1117, doi:10.1016/j.ajhg.2013.10.020 (2013).

21 Ravenscroft, G. *et al.* Mutations in KLHL40 are a frequent cause of severe autosomal-recessive nemaline myopathy. *Am J Hum Genet* **93**, 6-18, doi:10.1016/j.ajhg.2013.05.004 (2013).

22 Biga, L. M. *et al. Anatomy & Physiology*. (OpenStax/Oregon State University, 2018).

23 Paulsen, J. *et al.* Chrom3D: three-dimensional genome modeling from Hi-C and nuclear lamin-genome contacts. *Genome Biol* **18**, 21, doi:10.1186/s13059-016-1146-2 (2017).

24 Guelen, L. *et al.* Domain organization of human chromosomes revealed by mapping of nuclear lamina interactions. *Nature* **453**, 948-951, doi:10.1038/nature06947 (2008).

25 Crisp, M. *et al.* Coupling of the nucleus and cytoplasm: role of the LINC complex. *J Cell Biol* **172**, 41-53, doi:10.1083/jcb.200509124 (2006).

26 Stroud, M. J., Banerjee, I., Veevers, J. & Chen, J. Linker of nucleoskeleton and cytoskeleton complex proteins in cardiac structure, function, and disease. *Circ Res* **114**, 538-548, doi:10.1161/CIRCRESAHA.114.301236 (2014).

27 Strambio-De-Castillia, C., Niepel, M. & Rout, M. P. The nuclear pore complex: bridging nuclear transport and gene regulation. *Nat Rev Mol Cell Biol* **11**, 490-501, doi:10.1038/nrm2928 (2010).

28 Brull, A., Morales Rodriguez, B., Bonne, G., Muchir, A. & Bertrand, A. T. The Pathogenesis and Therapies of Striated Muscle Laminopathies. *Front Physiol* **9**, 1533, doi:10.3389/fphys.2018.01533 (2018).

29 Ungricht, R. & Kutay, U. Mechanisms and functions of nuclear envelope remodelling. *Nat Rev Mol Cell Biol* **18**, 229-245, doi:10.1038/nrm.2016.153 (2017).

30 Mekhail, K. & Moazed, D. The nuclear envelope in genome organization, expression and stability. *Nat Rev Mol Cell Biol* **11**, 317-328, doi:10.1038/nrm2894 (2010).

31 Kalverda, B. & Fornerod, M. Characterization of genome-nucleoporin interactions in Drosophila links chromatin insulators to the nuclear pore complex. *Cell Cycle* **9**, 4812-4817, doi:10.4161/cc.9.24.14328 (2010).

32 Brachner, A. & Foisner, R. Evolvement of LEM proteins as chromatin tethers at the nuclear periphery. *Biochem Soc Trans* **39**, 1735-1741, doi:10.1042/BST20110724 (2011).

33 Poleshko, A. *et al.* Genome-Nuclear Lamina Interactions Regulate Cardiac Stem Cell Lineage Restriction. *Cell* **171**, 573-587 e514, doi:10.1016/j.cell.2017.09.018 (2017).

34 Briand, N. & Collas, P. Laminopathy-causing lamin A mutations reconfigure lamina-associated domains and local spatial chromatin conformation. *Nucleus* **9**, 216-226, doi:10.1080/19491034.2018.1449498 (2018).

35 Scharner, J. *et al.* Novel LMNA mutations in patients with Emery-Dreifuss muscular dystrophy and functional characterization of four LMNA mutations. *Hum Mutat* **32**, 152-167, doi:10.1002/humu.21361 (2011).

36 Muchir, A. & Worman, H. J. Emery-Dreifuss muscular dystrophy: focal point nuclear envelope. *Curr Opin Neurol* **32**, 728-734, doi:10.1097/WCO.0000000000000741 (2019).

37 Bione, S. *et al.* Identification of a novel X-linked gene responsible for Emery-Dreifuss muscular dystrophy. *Nat Genet* **8**, 323-327, doi:10.1038/ng1294-323 (1994).

38 Le Thanh, P. *et al.* Immunohistochemistry on a panel of Emery-Dreifuss muscular dystrophy samples reveals nuclear envelope proteins as inconsistent markers for pathology. *Neuromuscul Disord* **27**, 338-351, doi:10.1016/j.nmd.2016.12.003 (2017).

39 Ziat, E. *et al.* FHL1B Interacts with Lamin A/C and Emerin at the Nuclear Lamina and is Misregulated in Emery-Dreifuss Muscular Dystrophy. *J Neuromuscul Dis* **3**, 497-510, doi:10.3233/JND-160169 (2016).

40 Liang, W. C. *et al.* TMEM43 mutations in Emery-Dreifuss muscular dystrophy-related myopathy. *Ann Neurol* **69**, 1005-1013, doi:10.1002/ana.22338 (2011).

41 Zhang, Q. *et al.* Nesprin-1 and -2 are involved in the pathogenesis of Emery Dreifuss muscular dystrophy and are critical for nuclear envelope integrity. *Hum Mol Genet* **16**, 2816-2833, doi:10.1093/hmg/ddm238 (2007).

42 Schirmer, E. C., Florens, L., Guan, T., Yates, J. R., 3rd & Gerace, L. Nuclear membrane proteins with potential disease links found by subtractive proteomics. *Science* **301**, 1380-1382, doi:10.1126/science.1088176 (2003).

43 Meinke, P. *et al.* A multistage sequencing strategy pinpoints novel candidate alleles for Emery-Dreifuss muscular dystrophy and supports gene misregulation as its pathomechanism. *EBioMedicine* **51**, 102587, doi:10.1016/j.ebiom.2019.11.048 (2020).

44 de Las Heras, J. I. *et al.* Tissue-specific NETs alter genome organization and regulation even in a heterologous system. *Nucleus* **8**, 81-97, doi:10.1080/19491034.2016.1261230 (2017).

45 Kim, J. K. *et al.* Nuclear lamin A/C harnesses the perinuclear apical actin cables to protect nuclear morphology. *Nat Commun* **8**, 2123, doi:10.1038/s41467-017-02217-5 (2017).

46 Abdelfatah, N. *et al.* Characterization of a Unique Form of Arrhythmic Cardiomyopathy Caused by Recessive Mutation in LEMD2. *JACC Basic Transl Sci* **4**, 204-221, doi:10.1016/j.jacbts.2018.12.001 (2019).

47 Vafiadaki, E. *et al.* Muscle lim protein isoform negatively regulates striated muscle actin dynamics and differentiation. *FEBS J* **281**, 3261-3279, doi:10.1111/febs.12859 (2014).

48 Liu, S. & Pellman, D. The coordination of nuclear envelope assembly and chromosome segregation in metazoans. *Nucleus* **11**, 35-52, doi:10.1080/19491034.2020.1742064 (2020).

49 Wilson, M. H. & Holzbaur, E. L. Nesprins anchor kinesin-1 motors to the nucleus to drive nuclear distribution in muscle cells. *Development* **142**, 218-228, doi:10.1242/dev.114769 (2015).

50 Hamrick, M. W., McGee-Lawrence, M. E. & Frechette, D. M. Fatty Infiltration of Skeletal Muscle: Mechanisms and Comparisons with Bone Marrow Adiposity. *Front Endocrinol (Lausanne)* **7**, 69, doi:10.3389/fendo.2016.00069 (2016).

51 Bertrand, A. T. *et al.* DelK32-lamin A/C has abnormal location and induces incomplete tissue maturation and severe metabolic defects leading to premature death. *Hum Mol Genet* **21**, 1037-1048, doi:10.1093/hmg/ddr534 (2012).

52 Kubben, N. *et al.* Post-natal myogenic and adipogenic developmental: defects and metabolic impairment upon loss of A-type lamins. *Nucleus* **2**, 195-207, doi:10.4161/nucl.2.3.15731 (2011).

53 Ramirez-Martinez, A. *et al.* The nuclear envelope protein Net39 is essential for muscle nuclear integrity and chromatin organization. *Nat Commun* **12**, 690, doi:10.1038/s41467-021-20987-x (2021).

54 Petrany, M. J. *et al.* Single-nucleus RNA-seq identifies transcriptional heterogeneity in multinucleated skeletal myofibers. *Nat Commun* **11**, 6374, doi:10.1038/s41467-020-20063-w (2020).

55 Potthoff, M. J. *et al.* Histone deacetylase degradation and MEF2 activation promote the formation of slow-twitch myofibers. *J Clin Invest* **117**, 2459-2467, doi:10.1172/JCI31960 (2007).

56 Wu, H. *et al.* Activation of MEF2 by muscle activity is mediated through a calcineurin-dependent pathway. *EMBO J* **20**, 6414-6423, doi:10.1093/emboj/20.22.6414 (2001).

57 Lu, J., Webb, R., Richardson, J. A. & Olson, E. N. MyoR: a muscle-restricted basic helix-loop-helix transcription factor that antagonizes the actions of MyoD. *Proc Natl Acad Sci U S A* **96**, 552-557, doi:10.1073/pnas.96.2.552 (1999).

58 Bank, E. M. *et al.* A laminopathic mutation disrupting lamin filament assembly causes disease-like phenotypes in Caenorhabditis elegans. *Mol Biol Cell* **22**, 2716-2728, doi:10.1091/mbc.E11-01-0064 (2011).

59 Quijano-Roy, S. *et al.* De novo LMNA mutations cause a new form of congenital muscular dystrophy. *Ann Neurol* **64**, 177-186, doi:10.1002/ana.21417 (2008).

60 Bertrand, A. T. *et al.* Lamin A/C Assembly Defects in LMNA-Congenital Muscular Dystrophy Is Responsible for the Increased Severity of the Disease Compared with Emery-Dreifuss Muscular Dystrophy. *Cells* **9**, doi:10.3390/cells9040844 (2020).

61 Zhang, Y. *et al.* Enhanced CRISPR-Cas9 correction of Duchenne muscular dystrophy in mice by a self-complementary AAV delivery system. *Sci Adv* **6**, eaay6812, doi:10.1126/sciadv.aay6812 (2020).

62 Pacak, C. A. *et al.* Recombinant adeno-associated virus serotype 9 leads to preferential cardiac transduction in vivo. *Circ Res* **99**, e3-9, doi:10.1161/01.RES.0000237661.18885.f6 (2006).

63 Kim, Y. & Zheng, Y. Generation and characterization of a conditional deletion allele for Lmna in mice. *Biochem Biophys Res Commun* **440**, 8-13, doi:10.1016/j.bbrc.2013.08.082 (2013).

64 Brussee, V., Tardif, F. & Tremblay, J. P. Muscle fibers of mdx mice are more vulnerable to exercise than those of normal mice. *Neuromuscul Disord* **7**, 487-492, doi:10.1016/s0960-8966(97)00115-6 (1997).

65 Dos Santos, M. *et al.* Single-nucleus RNA-seq and FISH identify coordinated transcriptional activity in mammalian myofibers. *Nat Commun* **11**, 5102, doi:10.1038/s41467-020-18789-8 (2020).

66 Kim, M. *et al.* Single-nucleus transcriptomics reveals functional compartmentalization in syncytial skeletal muscle cells. *Nat Commun* **11**, 6375, doi:10.1038/s41467-020-20064-9 (2020).

67 Chemello, F. *et al.* Degenerative and regenerative pathways underlying Duchenne muscular dystrophy revealed by single-nucleus RNA sequencing. *Proc Natl Acad Sci U S A* **117**, 29691-29701, doi:10.1073/pnas.2018391117 (2020).

68 Brachner, A., Reipert, S., Foisner, R. & Gotzmann, J. LEM2 is a novel MAN1-related inner nuclear membrane protein associated with A-type lamins. *J Cell Sci* **118**, 5797-5810, doi:10.1242/jcs.02701 (2005).

69 van Steensel, B. & Belmont, A. S. Lamina-Associated Domains: Links with Chromosome Architecture, Heterochromatin, and Gene Repression. *Cell* **169**, 780-791, doi:10.1016/j.cell.2017.04.022 (2017).

70 Raices, M. *et al.* Nuclear Pores Regulate Muscle Development and Maintenance by Assembling a Localized Mef2C Complex. *Dev Cell* **41**, 540-554 e547, doi:10.1016/j.devcel.2017.05.007 (2017).

71 Bakay, M. *et al.* Nuclear envelope dystrophies show a transcriptional fingerprint suggesting disruption of Rb-MyoD pathways in muscle regeneration. *Brain* **129**, 996-1013, doi:10.1093/brain/awl023 (2006).

72 Ozawa, R. *et al.* Emerin-lacking mice show minimal motor and cardiac dysfunctions with nuclear-associated vacuoles. *Am J Pathol* **168**, 907-917, doi:10.2353/ajpath.2006.050564 (2006).

73 Romero, N. B., Sandaradura, S. A. & Clarke, N. F. Recent advances in nemaline myopathy. *Curr Opin Neurol* **26**, 519-526, doi:10.1097/WCO.0b013e328364d681 (2013).

74 Wallgren-Pettersson, C., Sewry, C. A., Nowak, K. J. & Laing, N. G. Nemaline myopathies. *Semin Pediatr Neurol* **18**, 230-238, doi:10.1016/j.spen.2011.10.004 (2011).

75 Agrawal, P. B. *et al.* Heterogeneity of nemaline myopathy cases with skeletal muscle alpha-actin gene mutations. *Ann Neurol* **56**, 86-96, doi:10.1002/ana.20157 (2004).

76 Cenik, B. K. *et al.* Severe myopathy in mice lacking the MEF2/SRF-dependent gene leiomodin-3. *J Clin Invest* **125**, 1569-1578, doi:10.1172/JCI80115 (2015).

77 Donner, K. *et al.* Mutations in the beta-tropomyosin (TPM2) gene--a rare cause of nemaline myopathy. *Neuromuscul Disord* **12**, 151-158, doi:10.1016/s0960-8966(01)00252-8 (2002).

78 Johnston, J. J. *et al.* A novel nemaline myopathy in the Amish caused by a mutation in troponin T1. *Am J Hum Genet* **67**, 814-821, doi:10.1086/303089 (2000).

79 Lehtokari, V. L. *et al.* Identification of 45 novel mutations in the nebulin gene associated with autosomal recessive nemaline myopathy. *Hum Mutat* **27**, 946-956, doi:10.1002/humu.20370 (2006).

80 Wattanasirichaigoon, D. *et al.* Mutations of the slow muscle alpha-tropomyosin gene, TPM3, are a rare cause of nemaline myopathy. *Neurology* **59**, 613-617, doi:10.1212/wnl.59.4.613 (2002).

81 Yuen, M. *et al.* Leiomodin-3 dysfunction results in thin filament disorganization and nemaline myopathy. *J Clin Invest* **125**, 456-457, doi:10.1172/JCI80057 (2015).

82 Geyer, R., Wee, S., Anderson, S., Yates, J. & Wolf, D. A. BTB/POZ domain proteins are putative substrate adaptors for cullin 3 ubiquitin ligases. *Mol Cell* **12**, 783-790, doi:10.1016/s1097-2765(03)00341-1 (2003).

83 Gupta, V. A. & Beggs, A. H. Kelch proteins: emerging roles in skeletal muscle development and diseases. *Skelet Muscle* **4**, 11, doi:10.1186/2044-5040-4-11 (2014).

84 Dhanoa, B. S., Cogliati, T., Satish, A. G., Bruford, E. A. & Friedman, J. S. Update on the Kelch-like (KLHL) gene family. *Hum Genomics* **7**, 13, doi:10.1186/1479-7364-7-13 (2013).

85 Genschik, P., Sumara, I. & Lechner, E. The emerging family of CULLIN3-RING ubiquitin ligases (CRL3s): cellular functions and disease implications. *EMBO J* **32**, 2307-2320, doi:10.1038/emboj.2013.173 (2013).

86 Werner, A. *et al.* Cell-fate determination by ubiquitin-dependent regulation of translation. *Nature* **525**, 523-527, doi:10.1038/nature14978 (2015).

87 Taylor, A. *et al.* DNA sequence and muscle-specific expression of human sarcosin transcripts. *Mol Cell Biochem* **183**, 105-112, doi:10.1023/a:1006824331819 (1998).

88 Jiao, X. *et al.* DAVID-WS: a stateful web service to facilitate gene/protein list analysis. *Bioinformatics* **28**, 1805-1806, doi:10.1093/bioinformatics/bts251 (2012).

89 Pappas, C. T., Bliss, K. T., Zieseniss, A. & Gregorio, C. C. The Nebulin family: an actin support group. *Trends Cell Biol* **21**, 29-37, doi:10.1016/j.tcb.2010.09.005 (2011).

90 Pappas, C. T. *et al.* Knockout of Lmod2 results in shorter thin filaments followed by dilated cardiomyopathy and juvenile lethality. *Proc Natl Acad Sci U S A* **112**, 13573-13578, doi:10.1073/pnas.1508273112 (2015).

91 Bodine, S. C. *et al.* Identification of ubiquitin ligases required for skeletal muscle atrophy. *Science* **294**, 1704-1708, doi:10.1126/science.1065874 (2001).

92 D'Avila, F. *et al.* Exome sequencing identifies variants in two genes encoding the LIM-proteins NRAP and FHL1 in an Italian patient with BAG3 myofibrillar myopathy. *J Muscle Res Cell Motil* **37**, 101-115, doi:10.1007/s10974-016-9451-7 (2016).

93 Duff, R. M. *et al.* Mutations in the N-terminal actin-binding domain of filamin C cause a distal myopathy. *Am J Hum Genet* **88**, 729-740, doi:10.1016/j.ajhg.2011.04.021 (2011).

94 Komander, D. & Rape, M. The ubiquitin code. *Annu Rev Biochem* **81**, 203-229, doi:10.1146/annurev-biochem-060310-170328 (2012).

95 Kulathu, Y. & Komander, D. Atypical ubiquitylation - the unexplored world of polyubiquitin beyond Lys48 and Lys63 linkages. *Nat Rev Mol Cell Biol* **13**, 508-523, doi:10.1038/nrm3394 (2012).

96 Fang, S., Jensen, J. P., Ludwig, R. L., Vousden, K. H. & Weissman, A. M. Mdm2 is a RING finger-dependent ubiquitin protein ligase for itself and p53. *J Biol Chem* **275**, 8945-8951, doi:10.1074/jbc.275.12.8945 (2000).

97 Nuber, U., Schwarz, S. E. & Scheffner, M. The ubiquitin-protein ligase E6-associated protein (E6-AP) serves as its own substrate. *Eur J Biochem* **254**, 643-649, doi:10.1046/j.1432-1327.1998.2540643.x (1998).

98 Yau, R. & Rape, M. The increasing complexity of the ubiquitin code. *Nat Cell Biol* **18**, 579-586, doi:10.1038/ncb3358 (2016).

99 Furukawa, M. & Xiong, Y. BTB protein Keap1 targets antioxidant transcription factor Nrf2 for ubiquitination by the Cullin 3-Roc1 ligase. *Mol Cell Biol* **25**, 162-171, doi:10.1128/MCB.25.1.162-171.2005 (2005).

100 Liu, C. C. *et al.* Cul3-KLHL20 Ubiquitin Ligase Governs the Turnover of ULK1 and VPS34 Complexes to Control Autophagy Termination. *Mol Cell* **61**, 84-97, doi:10.1016/j.molcel.2015.11.001 (2016).

101 Shibata, S., Zhang, J., Puthumana, J., Stone, K. L. & Lifton, R. P. Kelch-like 3 and Cullin 3 regulate electrolyte homeostasis via ubiquitination and degradation of WNK4. *Proc Natl Acad Sci U S A* **110**, 7838-7843, doi:10.1073/pnas.1304592110 (2013).

102 Xu, L. *et al.* BTB proteins are substrate-specific adaptors in an SCF-like modular ubiquitin ligase containing CUL-3. *Nature* **425**, 316-321, doi:10.1038/nature01985 (2003).

103 Yuan, W. C. *et al.* K33-Linked Polyubiquitination of Coronin 7 by Cul3-KLHL20 Ubiquitin E3 Ligase Regulates Protein Trafficking. *Mol Cell* **54**, 586-600, doi:10.1016/j.molcel.2014.03.035 (2014).

104 Flick, K., Raasi, S., Zhang, H., Yen, J. L. & Kaiser, P. A ubiquitin-interacting motif protects polyubiquitinated Met4 from degradation by the 26S proteasome. *Nat Cell Biol* **8**, 509-515, doi:10.1038/ncb1402 (2006).

105 Ramadan, K. *et al.* Cdc48/p97 promotes reformation of the nucleus by extracting the kinase Aurora B from chromatin. *Nature* **450**, 1258-1262, doi:10.1038/nature06388 (2007).

106 Rape, M. *et al.* Mobilization of processed, membrane-tethered SPT23 transcription factor by CDC48(UFD1/NPL4), a ubiquitin-selective chaperone. *Cell* **107**, 667-677, doi:10.1016/s0092-8674(01)00595-5 (2001).

107 Jentsch, S. & Rumpf, S. Cdc48 (p97): a "molecular gearbox" in the ubiquitin pathway? *Trends Biochem Sci* **32**, 6-11, doi:10.1016/j.tibs.2006.11.005 (2007).

108 Goebel, H. H. & Blaschek, A. Protein aggregation in congenital myopathies. *Semin Pediatr Neurol* **18**, 272-276, doi:10.1016/j.spen.2011.10.009 (2011).

109 Olive, M. *et al.* New cardiac and skeletal protein aggregate myopathy associated with combined MuRF1 and MuRF3 mutations. *Hum Mol Genet* **24**, 3638-3650, doi:10.1093/hmg/ddv108 (2015).

110 Ryan, M. M. *et al.* Clinical course correlates poorly with muscle pathology in nemaline myopathy. *Neurology* **60**, 665-673, doi:10.1212/01.wnl.0000046585.81304.bc (2003).

111 Smith, D. A., Carland, C. R., Guo, Y. & Bernstein, S. I. Getting folded: chaperone proteins in muscle development, maintenance and disease. *Anat Rec (Hoboken)* **297**, 1637-1649, doi:10.1002/ar.22980 (2014).

112 Winter, L. *et al.* Chemical chaperone ameliorates pathological protein aggregation in plectin-deficient muscle. *J Clin Invest* **124**, 1144-1157, doi:10.1172/JCI71919 (2014).

113 Sarparanta, J. *et al.* Mutations affecting the cytoplasmic functions of the co-chaperone DNAJB6 cause limb-girdle muscular dystrophy. *Nat Genet* **44**, 450-455, S451-452, doi:10.1038/ng.1103 (2012).

114 Selcen, D. *et al.* Mutation in BAG3 causes severe dominant childhood muscular dystrophy. *Ann Neurol* **65**, 83-89, doi:10.1002/ana.21553 (2009).

115 Hernandez, J. M. & Podbilewicz, B. The hallmarks of cell-cell fusion. *Development* **144**, 4481-4495, doi:10.1242/dev.155523 (2017).

116 Brukman, N. G., Uygur, B., Podbilewicz, B. & Chernomordik, L. V. How cells fuse. *J Cell Biol* **218**, 1436-1451, doi:10.1083/jcb.201901017 (2019).

117 Kim, J. H. & Chen, E. H. The fusogenic synapse at a glance. *J Cell Sci* **132**, doi:10.1242/jcs.213124 (2019).

118 Millay, D. P. *et al.* Myomaker is a membrane activator of myoblast fusion and muscle formation. *Nature* **499**, 301-305, doi:10.1038/nature12343 (2013).

119 Bi, P. *et al.* Control of muscle formation by the fusogenic micropeptide myomixer. *Science* **356**, 323-327, doi:10.1126/science.aam9361 (2017).

120 Quinn, M. E. *et al.* Myomerger induces fusion of non-fusogenic cells and is required for skeletal muscle development. *Nat Commun* **8**, 15665, doi:10.1038/ncomms15665 (2017).

121 Zhang, Q. *et al.* The microprotein Minion controls cell fusion and muscle formation. *Nat Commun* **8**, 15664, doi:10.1038/ncomms15664 (2017).

122 Golani, G. *et al.* Myomerger promotes fusion pore by elastic coupling between proximal membrane leaflets and hemifusion diaphragm. *Nat Commun* **12**, 495, doi:10.1038/s41467-020-20804-x (2021).

123 Leikina, E. *et al.* Myomaker and Myomerger Work Independently to Control Distinct Steps of Membrane Remodeling during Myoblast Fusion. *Dev Cell* **46**, 767-780 e767, doi:10.1016/j.devcel.2018.08.006 (2018).

124 Leroy, H. *et al.* Virus-Mediated Cell-Cell Fusion. *Int J Mol Sci* **21**, doi:10.3390/ijms21249644 (2020).

125 Sudhof, T. C. & Rothman, J. E. Membrane fusion: grappling with SNARE and SM proteins. *Science* **323**, 474-477, doi:10.1126/science.1161748 (2009).

126 Millay, D. P. *et al.* Structure-function analysis of myomaker domains required for myoblast fusion. *Proc Natl Acad Sci U S A* **113**, 2116-2121, doi:10.1073/pnas.1600101113 (2016).

127 Shi, J. *et al.* Requirement of the fusogenic micropeptide myomixer for muscle formation in zebrafish. *Proc Natl Acad Sci U S A* **114**, 11950-11955, doi:10.1073/pnas.1715229114 (2017).

128 Gamage, D. G. *et al.* Insights into the localization and function of myomaker during myoblast fusion. *J Biol Chem* **292**, 17272-17289, doi:10.1074/jbc.M117.811372 (2017).

129 Landemaine, A. *et al.* Trout myomaker contains 14 minisatellites and two sequence extensions but retains fusogenic function. *J Biol Chem* **294**, 6364-6374, doi:10.1074/jbc.RA118.006047 (2019).

130 Pei, J., Millay, D. P., Olson, E. N. & Grishin, N. V. CREST--a large and diverse superfamily of putative transmembrane hydrolases. *Biol Direct* **6**, 37, doi:10.1186/1745-6150-6-37 (2011).

131 Millay, D. P., Sutherland, L. B., Bassel-Duby, R. & Olson, E. N. Myomaker is essential for muscle regeneration. *Genes Dev* **28**, 1641-1646, doi:10.1101/gad.247205.114 (2014).

132 Bi, P. *et al.* Fusogenic micropeptide Myomixer is essential for satellite cell fusion and muscle regeneration. *Proc Natl Acad Sci U S A* **115**, 3864-3869, doi:10.1073/pnas.1800052115 (2018).

133 Di Gioia, S. A. *et al.* A defect in myoblast fusion underlies Carey-Fineman-Ziter syndrome. *Nat Commun* **8**, 16077, doi:10.1038/ncomms16077 (2017).

134 Chattopadhyay, A. & Harikumar, K. G. Dependence of critical micelle concentration of a zwitterionic detergent on ionic strength: implications in receptor solubilization. *FEBS Lett* **391**, 199-202, doi:10.1016/0014-5793(96)00733-8 (1996).

135 Koker, T., Fernandez, A. & Pinaud, F. Characterization of Split Fluorescent Protein Variants and Quantitative Analyses of Their Self-Assembly Process. *Sci Rep* **8**, 5344, doi:10.1038/s41598-018-23625-7 (2018).

136 Cramer, A. A. W. *et al.* Nuclear numbers in syncytial muscle fibers promote size but limit the development of larger myonuclear domains. *Nat Commun* **11**, 6287, doi:10.1038/s41467-020-20058-7 (2020).

137 Petrany, M. J., Song, T., Sadayappan, S. & Millay, D. P. Myocyte-derived Myomaker expression is required for regenerative fusion but exacerbates membrane instability in dystrophic myofibers. *JCI Insight* **5**, doi:10.1172/jci.insight.136095 (2020).

138 Zhang, H. *et al.* Human myotube formation is determined by MyoD-Myomixer/Myomaker axis. *Sci Adv* **6**, doi:10.1126/sciadv.abc4062 (2020).

139 Duncan, R. Fusogenic Reoviruses and Their Fusion-Associated Small Transmembrane (FAST) Proteins. *Annu Rev Virol* **6**, 341-363, doi:10.1146/annurev-virology-092818-015523 (2019).

140 Shelton, J. M., Lee, M. H., Richardson, J. A. & Patel, S. B. Microsomal triglyceride transfer protein expression during mouse development. *J Lipid Res* **41**, 532-537 (2000).

141 Frey, N. *et al.* Mice lacking calsarcin-1 are sensitized to calcineurin signaling and show accelerated cardiomyopathy in response to pathological biomechanical stress. *Nat Med* **10**, 1336-1343, doi:10.1038/nm1132 (2004).

142 Frey, N., Richardson, J. A. & Olson, E. N. Calsarcins, a novel family of sarcomeric calcineurin-binding proteins. *Proc Natl Acad Sci U S A* **97**, 14632-14637, doi:10.1073/pnas.260501097 (2000).

143 Lim, K. L. *et al.* Parkin mediates nonclassical, proteasomal-independent ubiquitination of synphilin-1: implications for Lewy body formation. *J Neurosci* **25**, 2002-2009, doi:10.1523/JNEUROSCI.4474-04.2005 (2005).

144 Ishikawa, H., Meng, F., Kondo, N., Iwamoto, A. & Matsuda, Z. Generation of a dual-functional split-reporter protein for monitoring membrane fusion using self-associating split GFP. *Protein Eng Des Sel* **25**, 813-820, doi:10.1093/protein/gzs051 (2012).

145 Anders, S. & Huber, W. Differential expression analysis for sequence count data. *Genome Biol* **11**, R106, doi:10.1186/gb-2010-11-10-r106 (2010).

146 Kanehisa, M., Furumichi, M., Tanabe, M., Sato, Y. & Morishima, K. KEGG: new perspectives on genomes, pathways, diseases and drugs. *Nucleic Acids Res* **45**, D353-D361, doi:10.1093/nar/gkw1092 (2017).

147 Corces, M. R. *et al.* An improved ATAC-seq protocol reduces background and enables interrogation of frozen tissues. *Nat Methods* **14**, 959-962, doi:10.1038/nmeth.4396 (2017).

148 Mullen, A. R. *et al.* Oxidation of alpha-ketoglutarate is required for reductive carboxylation in cancer cells with mitochondrial defects. *Cell Rep* **7**, 1679-1690, doi:10.1016/j.celrep.2014.04.037 (2014).

149 Ritchie, M. E. *et al.* limma powers differential expression analyses for RNA-sequencing and microarray studies. *Nucleic Acids Res* **43**, e47, doi:10.1093/nar/gkv007 (2015).

150 Branon, T. C. *et al.* Efficient proximity labeling in living cells and organisms with TurboID. *Nat Biotechnol* **36**, 880-887, doi:10.1038/nbt.4201 (2018).

151 Black, B. L., Molkentin, J. D. & Olson, E. N. Multiple roles for the MyoD basic region in transmission of transcriptional activation signals and interaction with MEF2. *Mol Cell Biol* **18**, 69-77, doi:10.1128/MCB.18.1.69 (1998).

152 Makarewich, C. A. *et al.* The DWORF micropeptide enhances contractility and prevents heart failure in a mouse model of dilated cardiomyopathy. *Elife* **7**, doi:10.7554/eLife.38319 (2018).

153 Anglister, J., Grzesiek, S., Ren, H., Klee, C. B. & Bax, A. Isotope-edited multidimensional NMR of calcineurin B in the presence of the non-deuterated detergent CHAPS. *J Biomol NMR* **3**, 121-126, doi:10.1007/BF00242480 (1993).

154 Zhang, O., Kay, L. E., Olivier, J. P. & Forman-Kay, J. D. Backbone 1H and 15N resonance assignments of the N-terminal SH3 domain of drk in folded and unfolded states using enhanced-sensitivity pulsed field gradient NMR techniques. *J Biomol NMR* **4**, 845-858, doi:10.1007/BF00398413 (1994).

155 Johnson, B. A. & Blevins, R. A. NMR View: A computer program for the visualization and analysis of NMR data. *J Biomol NMR* **4**, 603-614, doi:10.1007/BF00404272 (1994).

156 Delaglio, F. *et al.* NMRPipe: a multidimensional spectral processing system based on UNIX pipes. *J Biomol NMR* **6**, 277-293, doi:10.1007/BF00197809 (1995).